Along-ridge diversity of melt migration processes in the mantle: implications from the northern Oman ophiolite

Norikatsu Akizawa

April/2014

博士論文

Along-ridge diversity of melt migration processes in the mantle: implications from the northern Oman ophiolite

金沢大学大学院自然科学研究科
環境科学専攻　自然計測講座

学籍番号: 1123142401
氏名: 秋澤 紀克
主任指導教員名: 荒井 章司

CONTENTS

1. INTRODUCTION

Polybaric fractional melting of peridotitic mantle from the garnet stability field (> 2.5 GPa) through the spinel stability field at the suboceanic upper mantle has been widely accepted for genesis of mid-ocean ridge basalt (MORB) (e.g. Klein & Langmuir, 1987; Johnson et al., 1990; Hellebrand et al., 2002). Melt within adiabatically upwelling asthenosphere migrates upward to the surface with aggregation, mixing, melt/wall rock interaction and crystallization processes (Grove et al., 1992; Collier & Kelemen, 2010). However, processes of MORB genesis in present-day suboceanic mantle remain enigmatic due to the absence of deep-seated in-situ samples. Meanwhile, ophiolites, that are fragments of ancient oceanic lithosphere exposed on land, sheds light on visualizing a melt migration process within the suboceanic mantle.

From field observations of ophiolites, the uppermost mantle section is dominantly composed of dunites and wehrlites, which are called Moho transition zone (MTZ) (Boudier & Nicolas, 1995). These rocks are in equilibrium with MORB, but harzburgite is not, in terms of clinopyroxene chemistry (e.g. Kelemen et al., 1995). Moreover, the MORB seems not to be saturated with orthopyroxene, although it is one of the major minerals of the harzburgite (e.g. Stolper, 1980). This contrast implies that melts are focused into a melt channel, which is composed of dunite and chemically isolated from surrounding residual peridotites (e.g. Iwamori, 1993; Kelemen et al., 1995). From lines of field evidence, geochemical data and numerical modeling, the melt channels below a ridge axis seem to be connected and getting thicker upward like a fractal tree (e.g. Hart, 1993; Spiegelman et al., 2001; Braun & Kelemen, 2002).

The melt channel formation mechanisms are separated into two end-members. One is mechanical fracturing that is initiated by exceeding fluid pressure within the host rock (e.g. Shaw, 1970; Nicolas & Jackson, 1982; Sleep, 1988; Arai & Matsukage, 1996; Suhr, 1999). The open fracture localizes melts with a proper pressure gradient and drains the melt upward. The fracture-related melt channel at shallower mantle section leaves dunites as a result of selective fractional crystallization of olivine from intruding melts and/or melt-wall rock interaction with pyroxenes dissolution of wall peridotites (Quick, 1981; Suhr, 1999). The other is called reactive infiltration instability (e.g. Chadam et al., 1986). Dissolution of solid mineral phases (pyroxenes) of the peridotite makes the melt channel highly porous, which induces melt flow with high permeability.

This mechanism works as positive feedback and channel size grows with time proceeding. The numerical modeling suggests that the melt localization process with the reactive infiltration instability spaces melt channels in 1~200 m during ~100,000 years, which are transformed into the so-called “replacive dunite channel” (Spiegelman et al., 2001).

As stated above, the melt channel-formation mechanism is clearly associated with dunite formation in the mantle section, where high-pressure MORB melts (parental MORB melts) migrate upward to assemble as low-pressure MORB melts, which erupts at a ridge axis. The high-pressure MORB melts are in equilibrium with olivine and pyroxenes at higher pressure, but are in equilibrium with only olivine at lower pressure (e.g. Kushiro, 1975). The high-pressure MORB melts interact with peridotites at low pressures, and selective dissolution of pyroxenes and precipitation of olivine leave dunite; i.e., high-pressure MORB melts + peridotite = low-pressure MORB melts + dunite (Arai, 2005). Efficient melt separation at the final trapped melt crystallization stage is inevitable for the dunite channel formation, if not, melt component-bearing rocks like troctolite, gabbro or plagioclase-bearing dunite are expected.

The parental MORB melts interact with mantle peridotites to evolve to MORB melt during their migration upward through the dunite channel. However, it is generally difficult to evaluate the parameters that constrain this interaction in natural systems (open magmatic systems), such as parental melt composition, melt influx rate, melt separation rate, and others. A mass conservation equation (Ozawa, 2001), which can treat the simultaneous operation of any reactions and multistage operation of various magmatic processes, is used to quantitatively constrain appropriate parameters of multiple open magmatic processes along the concordant dunite bands, which are ancient melt channels, of the northern part of the Oman ophiolite. The main purpose of this study is to clarify the diversity of melt-migration processes within the suboceanic upper mantle beneath a fast spreading mid-ocean ridge by conducting numerical modeling properly constrained with field and microscopic observations. I took the ridge segment structure into consideration in this study because of differences in geotherm along the ridge segment (e.g. Lin & Phipps Morgan, 1992), which possibly induces changes in melt migration processes.

2. GEOLOGICAL BACKGROUND

The Oman ophiolite, which is a fragment of Tethyan oceanic lithosphere formed at a fast spreading center, had been obducted onto the Oman margin until about 75Ma (e.g. Nicolas, 1989). It is the most extensively exposed ophiolite in the world, 500 km in the NW-SE directions, and 50~100 across (Lippard et al., 1986; Nicolas, 1989). It allows us to observe paleo-oceanic lithosphere on land and in three dimensions, and provides us with information on the whole picture from its generation at the mid-ocean ridge to the end of magmatism when obducted on land. However, several events such as hydrothermal activity, off-ridge magmatism and weathering have made its lithology complicated, and we should be careful for which event we are looking at.

2.1. Segment structures of the Oman ophiolite & present-day fast-spreading ridges

The extensively exposed Oman ophiolite comprehensively shows segment structures, which correspond to those observed at the present-day fast spreading ridge. The segment structures are divided into four orders on the present-day ocean floor; first order (300~500 km), second order (50~300 km), third order (30~100 km) and forth order (10~50 km) (Macdonald et al., 1988). Transform faults define the first-order ridge segmentation, in which finer segmentations (second to fourth orders) occur. Overlapping spreading centers (OSCs) divide the ridge axis into the second- to third-order segments, and deviations from axial linearity (DEVAL) divide into the fourth-order segment (Macdonald et al., 1991). Ridge segmentation is possibly related to various patterns of mantle upwelling or distribution of magma supply (e.g. Macdonald et al., 1991). Two-dimensional sheet-like mantle flow and three-dimensional diapiric mantle flow have been proposed as the models of mantle upwelling beneath fast-spreading centers (e.g. Lin & Phipps Morgan, 1992; Barth and Mutter, 1996; Toomey et al., 2007); the actual mantle flow pattern below fast-spreading ridges remain debated because of the relatively low resolution of geophysical imaging at these depths.

The scale of the Oman ophiolite is equivalent to the spacing between transform faults (first order) containing fine-scale segmentations, OSCs (second and third orders) and DEVAL (fourth orders) (Ceuleneer, 1986). The segment structures have been

described from the structural point of view at the Oman ophiolite. The attitude of lineation and foliation preserved in the mantle peridotites of Oman points to diapiric flow beneath the paleo-ridge (e.g. Ceuleneer et al., 1988; Nicolas et al., 2000). Therefore, the diapiric mantle upwelling was inferred in the case of the Oman ophiolite, but no structural evidence indicating such diapiric mantle upwelling has been observed at the northern Oman ophiolite, except for Aswad massif (Nicolas et al., 2000). On the other hand, the trend of the sheeted dikes, which is subparallel to the paleo-ridge axis, is expected to have changed at fossil segment boundaries of the second- to fourth-order segmentations. Such discontinuities have been reported from the Oman ophiolite, but no transform faults corresponding to the first-order segmentation (e.g. MacLeod & Rothery, 1992). Higher magma supply to the segment center possibly caused a thick MTZ, whose domed-up summit lifted up the gabbroic section to make it thinner. Thus, the thick MTZ and thin gabbroic section characterize the paleo-ridge segment center of the Oman ophiolite (e.g. Nicolas et al., 1996; Nicolas & Boudier, 2000).

Detailed segment structures, corresponding to second- and third-order segmentations, have been particularly well recognized at Fizh massif (MacLeod & Rothery, 1992; Adachi & Miyashita, 2003; Miyashita et al., 2003; Umino et al., 2003) in the northern Oman ophiolite. A fossil segment boundary corresponding to second-order segmentation (paleo-OSCs) was proposed between Wadi Zabin and Wadi Fizh (Adachi & Miyashita, 2003). The boundary is characterized by an intense dike penetration zone, where layered gabbros are intruded by NNW-striking dikes subparallel to the overlying sheeted dike complex (Adachi & Miyashita, 2003). A segment center of the second-order segmentation is inferred by lines of thick MTZ, thin gabbroic section, strong lineation of the layered gabbro and well ordered sheeted dikes along Wadi Thuqbah, whereas no traces for southern segment margin has been observed on account of faults at southern Hilti massif (Miyashita et al., 2003). The 60~70 km-long second-order segmentation contains a paleo-DEVAL (third-order segmentation), which is confirmed by the changing trend of the sheeted dike complex from NS strike to NNE~NS strike toward the south around Wadi Bani Umar al Gharbi (Umino et al., 2003). Nevertheless, segment structures in deeper parts of the mantle section of the Oman ophiolite are unclear because of continual deformations until the end of its emplacement onto the Arabian margin.

Another segment boundary is also inferred between Wadi Rajmi and Wadi Zabin, where WNW-trending dikes crosscut NS-trending sheeted dike complex (MacLeod & Rothery, 1992). However, the WNW-trending, corss-cutting dikes are boninitic in terms of phenocryst assemblage, mineral chemistry and bulk composition (Adachi & Miyashita, 2003). A finger-like distribution of highly depleted peridotites [Cr/(Cr + Al) atomic ratio of chromian spinel > 0.7] is proposed in the northern Fizh massif (Suetake & Takazawa, 2012), where subduction-related fluid flux affected the residual peridotites with remelting, and boninitic melts generated and migrated upward to penetrate into the preexisting NS-trending sheeted dike complex (Adachi & Miyashita, 2003). Hence, a part of northern Fizh massif was overprinted by subduction-related magmatism through mantle to crust.

2.2 Dunite distribution in the Oman ophiolite & melt channel distribution beneath a present-day fast-spreading ridge

The surface area of dunites and wehrlites is estimated as about 5 % of the Oman ophiolite (Nicolas et al., 2000). Most of them are exposed as a member of MTZs, which are diverse in thickness from few meters to several hundred meters (< 1,000 m) along the paleoridge segment of the Oman ophiolite (e.g. Nicolas et al., 1996). At the northern Oman ophiolite, thickness of the MTZ highly varies from about 10 m at Wadi Fizh (segment end) (Akizawa & Arai, 2009) to about 1,000 m at Wadi Thuqbah (segment center) (Negishi et al., 2013). This variation can be explained by difference in amounts of magma supply or in degree of modification by late intrusive rocks. The MTZ of Wadi Fizh has preserved primary rocks formed beneath the mid-ocean ridge (Akizawa et al., 2012), while disturbed to varying extents by off-ridge magmatism associated with the initiation of subduction at Wadi Thuqbah (Negishi et al., 2013). However, the initial thickness of MTZ was possibly far thicker along Wadi Thuqbah than along Wadi Fizh, and thus, a larger amount of melt had been involved in thick MTZ formation of Wadi Thuqbah. MTZ-forming rocks such as dunite and wehrlite are in equilibrium with MORB, and the MTZ is considered as a main reservoir of MORB magma at the uppermost mantle beneath mid ocean-ridges (e.g. Kelemen et al., 1995; Akizawa et al., 2012).

The extensive Oman ophiolite provides us with information on fossil melt channels within the mantle section, which are classified into two in appearance, concordant dunite bands and discordant dunite dikes (e.g. Arai et al., 2006). Melt channels beneath a mid-ocean ridge are transported outward from the ridge axis via horizontal mantle flow and transformed into concordant dunite bands (e.g. Cassard et al., 1981). In contrast, discordant dunite dikes are related to off-ridge magmatism. Thus, the Oman ophiolite had recorded multiple melt migration processes, which played different roles in magma genesis; the older concordant dunite bands for MORB magma genesis, and the younger discordant dunite dikes for arc-related magma genesis. A melt channel distribution beneath a fast spreading center is interpreted as coalescing network upward like fractal tree by field observations of dunite channel, its shape, size, abundance and distribution, at the Oman ophiolite (Kelemen et al., 2000; Brawn & Kelemen, 2002). A lot of small-size melt channels fed melts upward via a large-size melt channel, and thus, melt flow was ultimately focused to a narrow region just beneath a fats-spreading ridge axis (Kelemen et al., 2000).

Modeling and seismic data from the present-day fast-spreading ridge suggest that the partially molten region is ~70 km in depth and the order of 100 km wide at its base (Forsyth et al., 1998; Katz, 2010). On the other hand, the seismic data collected in a fourth-order segment around 9°30'N at East Pacific Rise suggested that the narrow region at the uppermost mantle (less than 20 km wide across the spreading center, up to several kilometers deep from the lower end of the crust) contains a large amount of melt fraction (up to approximately 10 %) (Dunn et al., 2000). The partially molten region, which corresponds to the scale of melt channel distribution, is focused from the order of 100 km wide at its base to few tens of kilometers beneath the fast-spreading ridge axis in the model. The summit of the partially molten region in the uppermost mantle at present-day fast-spreading ridges possibly corresponds to the MTZ and the upper mantle section below in the Oman ophiolite.

3. FIELD RELATIONS AND FABRICS OF DUNITE BANDS

I focused on the mantle section of the northern to central Oman ophiolite in this study, from which I selected 28 outcrops (Fig. 1). They are numbered as T-1~T-10 (Wadi

Thuqbah), R-1~R-3 (Wadi Rajmi), Z-1 (Wadi Zabin), F-1~F-6 (Wadi Fizh), H-1 (Wadi Hilti), S-1~S-4 (Wadi Sarami), Ry-1 (Wadi Rayy), U-1 (Wadi Umm al Hasa) and K-1 (Wadi Khudayrah). The mantle section is classified into five subsets for simplicity; the "uppermost mantle section" expands few tens of meters below the base of the MTZ, the "upper mantle section" refers to the upper mantle below the uppermost mantle section, that extend up to 5 km in map to the west of the base of the layered gabbro section (possible Moho; Akizawa and Arai, 2009), the "middle mantle section" expands in the area from 5 km to 10 km in map to the west of the base of the layered gabbro section, the "lower mantle section" expands in map over 10 km to the west of the base of the layered gabbro section, and the "basal section" is located at the base of the mantle section in the Oman ophiolite, above the metamorphic sole.

The outcrops are classified as below; uppermost mantle section (11 outcrops): T-1~T-4, F-1~F-5 and S-1~S-2, upper mantle section (5 outcrops): T-5~T-6, R-1~R-2 and F-6, middle mantle section (6 outcrops): T-7, R-3, Z-1, H-1 and S-3~S-4, lower mantle section (3 outcrops): T-8~T-10, and basal section (3 outcrops): Ry-1, U-1 and K-1 (Fig. 1). Outcrops S-1~S-3 are located in the Sarami massif, whereas outcrop S-4 is in the Wuqbah massif, where the crustal section is placed at the center of the massif (Girardeau et al., 2002), and thus, outcrop S-4 is classified in the middle mantle section (approximately 5~6 km to the base of the layered gabbro section). I assume the outcrops along Wadi Thuqbah (T-1~T-10) are located in the center of a second-order paleo-ridge segment, whereas other outcrops (R-1~R-3, Z-1, F-1~F-6, H-1 and S-1~S-4) are uncertain as from which part of the paleo-ridge segment they are located in. However, they are obviously located in a distal part of the paleo-ridge segment center, and possibly a segment end. In the other outcrops (Ry-1, U-1 and K-1), the MORB-related peridotites had been overprinted by off-ridge magmatism (e.g. Takazawa, 2012).

Outcrops T-1, F-1 and S-1 are from the MTZ; T-1 is from the thick MTZ (< 1,000 m) of the segment center along Wadi Thuqbah (Negishi et al. 2013), F-1 is from the thin MTZ (about 10 m) of a segment end along Wadi Fizh (cf. Akizawa et al., 2012), and S-1 is from the thin MTZ (< few tens of meters) of a segment end along Wadi Sarami. To eliminate modifications by off-ridge magmatism, I conducted careful field observations to select samples from the MTZs that were formed beneath the ridge axis. The MTZs contain gabbroic bands parallel with the base of the layered gabbro section (Akizawa and Arai, 2009). The bands vary in thickness from a few centimeters to less

than several tens of centimeters. The band/harzburgite boundaries are different in appearance along the paleoridge segment; diffused at the segment center (Fig. 2a), and rather sharp at segment ends (Akizawa et al., 2012). The other outcrops (T-2~T-10, R-1~R-3, Z-1, F-2~F-6, H-1 and S-2~S-4) consist of mantle peridotite with concordant dunite bands or discordant dunite dikes. I took samples from the dunite part, its aureole peridotite and ambient peridotite away from the dunite at each outcrop. The "aureole peridotites" were taken within a few centimeters away from the dunite/peridotite boundary, whereas the "ambient peridotites" were taken away from metasomatic agents like bands, dikes and veins, to eliminate any magmatic features that may have been generated after the melting process.

Most of the concordant dunite bands are deformed with the ambient peridotites, but some of them appear to branch off from discordant dunite dikes, and their concordance is not due to deformation. To distinguish those two types of concordant dunite bands, I carefully checked markers of deformation in the dunite. Elongated spinel seams and lens-shaped orthopyroxene grain in parallel with a flat dunite/peridotite boundary well indicate that the dunite band was deformed with the ambient peridotite (Fig. 2b). I also judged that several parallel concordant dunite bands with clearly flat dunite/peridotite boundaries were deformed with the ambient peridotite (Figs. 2c and d). In contrast, it is impossible to deduce the amount of deformation only from field observations for solitary concordant dunite bands without any visible, macroscopic markers of deformation.

I prepared highly polished thin sections of such solitary concordant dunite bands and associated peridotites, and examined their olivine crystal preferred orientations (CPO) by using a HITACHI S-3400N SEM system equipped with electron back-scattered diffraction (EBSD) at Shizuoka University. Results of samples from five outcrops (T-3, T-4, T-5, F-3 and F-6) suitable for EBSD analysis are shown in Figure 3. The comparative olivine CPO patterns between dunite and peridotite are as below; (1) similar in outcrop T-4 (Figs. 3c and d) and outcrop T-5 (Figs. 3e and f), (2) slightly similar in outcrop F-6 (Figs. 3i and j), and (3) completely different in outcrop T-3 (Figs. 3a and b) and outcrop F-3 (Figs. 3g and h). This indicates that solitary concordant dunite bands were deformed with surrounding peridotites at outcrops T-4, T-5 and F-6, whereas not the case at outcrops T-3 and F-3. I refer to the concordant dunite band of outcrops T-3 and F-3 as "dunite band", and to the other concordant dunite bands as

“concordant dunite bands”. Thus, the term “concordant” hereafter includes the petrofabric concordance with the surrounding peridotite.

Stratigraphic distributions of the concordant dunite bands are different in the studied mantle sections along the paleoridge segment. First, I will focus on the segment center. Concordant dunite bands decrease in frequency and increase in thickness upward to the base of the MTZ. Their maximum thickness is 250 cm (outcrop T-4) in the uppermost mantle section, but less than 100 cm in the lower mantle section (Fig. 2e). Note that thin dunite bands (a few centimeters to a few tens of centimeters) were observed at all stratigraphic levels, although they are less frequent upward. Some concordant dunite bands are accompanied by lens-shaped dunites, which are up to few centimeters thick and parallel to the bands. Moving on to the segment end, all concordant dunite bands are thinner (< 50 cm) in comparison with those observed at the segment center, but slightly increase in thickness and decrease in frequency upward. I found some outcrops that show some solitary concordant dunite bands (outcrops R-1, R-2, F-5, H-1 and S-3) (Figs. 2c and d), although the concordant dunite bands are not frequent at the segment end.

Some concordant dunite bands are associated with orthopyroxene-rich rocks; orthopyroxenite lens along the center and boundary of the dunite band at outcrop T-2 (Fig. 2f), and orthopyroxene-rich harzburgite along the boundary with the dunite band at outcrop T-5. This type of dunite band is thin (up to few tens of centimeters), and frequent in the middle to uppermost mantle section at the segment center, but some are still observed at segment ends.

For comparison, we examined a discordant dunite dike at the lower mantle section along Wadi Thuqbah (outcrop T-10), and concordant dunite bands at the basal section along Wadis Rayy, Umm al Hasa and Khudayrah (outcrops Ry-1, U-1 and K-1). The discordant dunite dike contains orthopyroxene lenses (up to few centimeters) and spinel seams. The dike/peridotite boundary is sharp, but weakly waving. At the basal section along Wadi Rayy (outcrop Ry-1), concordant dunite bands are frequent and thick (Fig. 2g); they are extremely thick up to 400 cm, and contain elongated chromitites (Fig. 2h) and pockets of orthopyroxenite (Fig. 2i). In contrast, concordant dunite bands are rather thin (a few centimeters) and sparse along Wadi Umm al Hasa and Wadi Khudayrah (outcrops U-1 and K-1).

4. PETROGRAPHY

Sufficiently fresh samples are required for detailed observations across the dunite/peridotite boundary, i.e., for checking modal, structural and mineral chemical changes across the boundary. However, samples are serpentinized to varying extents, and some dunites are completely altered, except for cores of chromian spinel, which I could analyze for major-element compositions. Ambient peridotites are fresh in comparison with dunites, and their primary textures and minerals have been sufficiently preserved for my use.

Dunites are almost free from clinopyroxenes, which, if any, are tiny and interstitial to olivines and spinels (Fig. 4a). Aureole peridotites of the dunites are also depleted in clinopyroxene, except for outcrop F-5, where clinopyroxenes partially or completely replace orthopyroxene porphyroclasts (Fig. 4b). Additionally, the harzburgite about 20 cm above the concordant dunite band at outcrop F-5 contains composite grains of orthopyroxene, clinopyroxene, saussurite and chromian spinel with olivine inclusions (Fig. 4c). Only the thickest concordant dunite band at outcrop T-4 contains large (up to 3 mm in diameter) clinopyroxene grains with orthopyroxene blebs (Fig. 4d). Some concordant dunite bands contain vermicular-shaped orthopyroxenes with association of trace amount of clinopyroxenes at outcrops T-7, R-2, F-3, F-6, Ry-1 and K-1 (Fig. 4e), whereas the discordant dunite dike contains lens-shaped coarse (up to 3 cm in the long axis) composite grains of orthopyroxene with small amount of interstitial clinopyroxene and euhedral to subhedral chromian spinel. The aureole peridotites usually contain highly irregular-shaped orthopyroxenes, of which size is smaller than that of the ambient peridotites. All dunites are composed of coarse olivines in comparison with the ambient peridotites, except in outcrop Ry-1, where the dunites and surrounding peridotites are exceptionally fine grained and mylonitic owing to post-emplacement high T-deformation (e.g. Nicolas et al., 2000; Takazawa et al., 2003). No plagioclase has been found from dunites.

Lherzolitic peridotites have been reported from the northern Oman ophiolite (Takazawa et al., 2003), but none of the ambient peridotites studied have exceeded 5 vol.% in modal amount of clinopyroxene, and they are all “harzburgites”. Clinopyroxenes of the ambient harzburgites are various in both modal amount and appearance at various stratigraphic levels along the paleoridge segment (Table 1). At the

uppermost mantle section, all ambient harzburgites are almost free from clinopyroxenes, and, if any, small in size and associated with orthopyroxenes (Fig. 4f). At the lower to upper mantle section, the ambient harzburgites are depleted in clinopyroxene at the segment center, where some clinopyroxenes are still interstitial to olivine (Fig. 4g), whereas coarse-grained clinopyroxene-rich harzburgites are occasionally found at the segment end (Fig. 4h). All of the ambient peridotites examined are also free of plagioclase.

5. MINERAL CHEMISTRY

5.1. Analytical methods

Major-element analysis of olivine, pyroxenes, plagioclase and chromian spinel was conducted with a JEOL JXA-8800R microprobe at Kanazawa University. I analyzed only cores of mineral grains as no significant intra-grain chemical heterogeneity was detected. I used an accelerating voltage of 20 kV, a probe current of 20 nA and a probe diameter of 3 μm. Natural and synthetic minerals were used as standards. Raw data were corrected using the ZAF online correction program. All Fe was assumed to be ferrous iron (Fe^{2+}) in silicates, and Fe^{2+} and ferric iron (Fe^{3+}) in spinel were calculated assuming spinel stoichiometry. Mg# is Mg/(Mg + Fe^{2+}) atomic ratio and Cr# is Cr/(Cr + Al) atomic ratio, respectively. Fo is 100×Mg# in olivine. An is 100×Ca/(Ca + Na + K) atomic ratio in plagioclase. Representative major-element compositions of minerals are listed in Tables 2 to 6.

Trace-element concentrations of clinopyroxene and orthopyroxene in samples were determined with a laser ablation (193 nm ArF excimer: MicroLas GeoLas Q-plus)-inductively coupled plasma mass spectrometer (Agilent 7500S) (LA-ICP-MS) at Kanazawa University (Ishida et al. 2004; Morishita et al. 2005a, b). Each analysis was performed by ablating 40-60 μm in diameter for clinopyroxene at 6 Hz with energy density of 8 J/cm^2 per pulse, and 100-110 μm in diameter for orthopyroxene, olivine and plagioclase at 10 Hz with energy density of 8 J/cm^2 per pulse. Signal integration times were 50s for a gas background interval, and 50s for clinopyroxene and 30s for orthopyroxene, olivine and plagioclase for an ablation interval. The element

concentrations of the NIST SRM 612 were selected from the preferred values of Pearce et al. (1997). Data reduction was facilitated using ^{29}Si as the internal standard for pyroxenes, based on SiO_2 contents determined by microprobe, following a protocol essentially identical to that outlined in Longerich et al. (1996). The accuracy of measurements estimated from analyses of reference material (NIST SRM 614) is better than 4 % in relative standard deviation for all elements. Representative trace-element compositions of minerals are listed in Tables 7 and 8.

5.2. Major-element chemistry

Major-element compositions of olivine, chromian spinel, clinopyroxene and orthopyroxene in dunites, aureole harzburgites and ambient harzburgites are shown in Figure 6. Dunites from MTZs exhibit deviations from melting trends defined by the ambient peridotites (Figs. 5a and b), and slight enrichment in incompatible elements like TiO_2 of chromian spinel (Fig. 5c) and Al_2O_3 of clinopyroxene (Fig. 5g). Most of the dunites below the MTZ overlap in major-element mineral compositions with the ambient harzburgites, except the discordant dunite dike at outcrop T-10 and concordant dunite bands from the basal section (outcrops Ry-1, U-1 and K-1). Such exceptional dunites are highly depleted, showing higher Fo (91~94) and NiO content (0.35~0.5 wt%) of olivine (Figs. 5a and b), lower TiO_2 content (< 1.5 wt%) and higher Cr# (0.6~0.8) of chromian spinel (Figs. 5c and e), and lower Al_2O_3 content (< 1.5 wt%) and Cr_2O_3 content (< 0.8 wt%) of clinopyroxene (Figs. 5g and i). The concordant dunite bands at outcrops Z-1 and F-6 deviate in chemical compositions from trends defined by dunite bands in the lower to uppermost mantle section, but overlap with those from the basal section (Fig. 5). The dunite band from outcrop T-3 and the concordant dunite bands associated with orthopyroxene-rich rocks from outcrops T-2 and T-5 show the same chemical characteristics as other concordant dunite bands at the same stratigraphic levels (Figs. 5c, e, g and i). Al_2O_3 and Cr_2O_3 of clinopyroxene in dunites clearly increase upward with a decrease of Mg# (Figs. 5g and i), whereas other minerals seem to be scattered in chemical space without any systematic changes upward. The Cr# of chromian spinel in dunite is, however, slightly lower on average at the uppermost mantle section (Figs. 5c and e).

Most of the ambient harzburgites exhibit a character of ordinary mantle restite, tracing both olivine mantle array (OMA, Takahashi et al., 1986) (Fig. 5a) and olivine-spinel mantle array (OSMA, Arai, 1994) (Fig. 5b). We expect an increase in melting degree upward on a polybaric fractional melting trend of mantle peridotites (e.g. Plank & Langmuir, 1992). However, no clear evidence in major elements for increasing melting degree upward was found, but an increase in incompatible elements and Cr in clinopyroxene from the basal section to the uppermost mantle section through the lower mantle section, middle mantle section and upper mantle section was clearly observed instead (Figs. 5h and j). We compiled major-element compositions of chromian spinel in the aureole harzburgites and the ambient harzburgites around the dunites in Figures 5d and f. However, no or little systematic increase in incompatible elements in chromian spinel was shown from the ambient harzburgite to the aureole harzburgite around the dunite bands. In contrast, the aureole harzburgite around the discordant dunite dike is highly depleted; it shows high Cr# (approximately 0.8) and low TiO_2 content (almost nil wt%) of chromian spinel (Figs. 5d and f). The ambient harzburgites are highly depleted in the basal section, except for outcrop K-1, where the ambient harzburgite shows about 91 Fo of olivine (Fig. 5a), about 0.50 Cr# of chromian spinel (Figs. 5d and f), and about 2.0~2.5 wt% Al_2O_3 and about 0.90 wt% Cr_2O_3 of clinopyroxene (Figs. 5h and j).

5.3. Trace-element chemistry

Chondrite-normalized trace-element (rare earth elements = REE, Sr, Zr and Ti) patterns of clinopyroxene from dunites and ambient harzburgites are shown in Figures 6-9. In the case of dunites that are free of clinopyroxenes, data are acquired from the aureole harzburgite in contact with the dunite body, which are expected to be the same as those from the dunites.

The MTZ rocks such as wehrlites, dunites, and olivine gabbros show the same trace-element pattern of clinopyroxene, i.e., gently declining from heavy REE (HREE) to light REE (LREE) through middle REE (MREE), although their levels are different, higher in Wadi Fizh, and lower in Wadi Thuqbah and Wadi Sarami (Figs. 6a and b). The clinopyroxene trace-element pattern in the harzburgite just below the MTZ in Wadi Thuqbah is similar to that from the MTZ dunite, although the concentration is lower in

the former (Fig. 6a). According to a few meters-scale geochemical profile of the MTZ, REE concentrations of clinopyroxene systematically increase upward in Wadi Fizh (cf. Akizawa et al., 2012), and possibly also in Wadi Thuqbah and Wadi Sarami. Plagioclases of the MTZ olivine gabbros in Wadi Thuqbah and Wadi Fizh show almost the same trace-element characteristics, although the concentrations are different (higher in Wadi Fizh, and lower in Wadi Thuqbah; Fig. 6c).

The shape of the trace-element patterns of clinopyroxene in dunite bands varies along the paleo-ridge segment. At the segment center, the trace-element pattern changes from spoon shape in the lower to middle mantle section (Figs. 7e and f) to moderately declining from HREE to LREE in the upper to uppermost mantle section (Figs. 7b and d). At the segment end, the moderately declining pattern of clinopyroxene is predominant (Figs. 8a-b, f, g-i and k). However, the concordant dunite bands that contain high Cr# spinel in outcrops Z-1 and F-6 show a positive anomaly of Sr, and negative anomalies of Zr and Ti in the moderately declining trace-element pattern of clinopyroxene, which is possibly in equilibrium with boninitic magma (Figs. 8g and h).

The clinopyroxene from dunite bands that are associated to orthopyroxene-rich rocks are extremely depleted in trace elements in outcrops T-2 and T-5 (Figs. 7a and c). Furthermore, some dunite bands from the middle to uppermost mantle section also contain such depleted clinopyroxene (Fig. 7b, 8d-e, 8j and 8l). The concordant dunite bands from outcrops F-3 and F-5 exceptionally show spoon-shaped trace-element patterns of clinopyroxene in the uppermost mantle section at the segment end, which are variable in LREE to MREE contents even within a single thin section (about 4 cm long by 2 cm) (Figs. 8b and c). The clinopyroxene of the composite grains (Fig. 4c) exceptionally shows convex upward trace-element pattern in the harzburgite about 20 cm above the concordant dunite band in outcrop F-5 (Fig. 8c).

For comparison, trace-element patterns of clinopyroxene from the discordant dunite dike and the concordant dunite bands in the basal section are shown in Figure 9. The clinopyroxene in the discordant dunite dike is almost in equilibrium with boninitic melt in terms of the trace-element composition (Fig. 9a). In the basal section, the trace-element patterns of clinopyroxene in the concordant dunite bands are highly declining from HREE to LREE in outcrops Ry-1 and K-1 (Figs. 9b and d), and moderately declining in outcrop U-1 (Fig. 9c).

Most of the residual clinopyroxenes in the ambient harzburgites are depleted in trace elements, but they show slight enrichment in LREE to MREE at the segment center (Figs. 7), and slight (Figs. 8a-d, f, i and l) or moderate (Figs. 8e, g-h and j-k) enrichment in LREE to MREE at the segment end. The enrichment in LREE is unachievable by simple fractional melting process of a peridotite, because LREEs are more incompatible with the clinopyroxene than HREEs and more efficiently removed away from them (Hellebrand et al., 2002).

6. DISCUSSION

6.1. Evolution of MTZs along the ridge segment

Main components of the MTZ, dunites and wehrlites, are considered as a product of reaction between MORB-like melt and harzburgite, where incongruent melting of orthopyroxene played an important role (Nicolas & Prinzhofer, 1983). Thus, the MTZ was an intense reaction zone and main reservoir of MORB-like melts at the mantle section, which erupted as a MORB at the ridge axis (Kelemen et al., 1995). I discuss here an evolutionary process of the MTZ.

The MTZ is thick (< 1,000m) at Wadi Thuqbah (segment center), whereas rather thin at Wadis Fizh and Sarami (segment end) as mentioned above. Detailed mineral chemical profile of harzburgite-dunite-wehrlite sequence just beneath the MTZ of Wadi Fizh revealed that incompatible elements increase in abundance upward as a function of the degree of MORB-like melt/harzburgite interaction associated with incongruent melting of orthopyroxenes (cf. Akizawa et al., 2012). Less chemical data of minerals have been accumulated for MTZs of Wadis Thuqbah and Sarami to compare with the one of Wadi Fizh, but mineral chemical characteristics apparently overlap with each other for all MTZs (Figs. 5 and 6). This possibly indicates that essentially the same mechanism worked for the formation of MTZ irrespective of its thickness.

A large amount of melt was supplied to thicken the MTZ of Wadi Thuqbah, which is consistent with depletion of modal clinopyroxene in the underling harzburgite (Fig. 4g). The MORB-like melts involved in forming the thick MTZ of Wadi Thuqbah were clearly rich in Cr (Fig. 5i), indicating a higher melting degree of underling mantle

peridotite at the segment center. The mantle temperature is estimated to be higher at the segment center than at the segment end at a given depth (e.g. Lin & Phipps Morgan, 1992), and therefore, the melting degree of mantle peridotite is higher on average at the segment center in the same level.

The olivine gabbro bands within or beneath the MTZ of Wadi Thuqbah and Wadi Fizh are chemically equilibrated with MORB (Akizawa et al., 2012). Their olivines and clinopyroxenes have been re-equilibrated in terms of Fe-Mg distribution at subsolidus condition (possibly 800~900 °C) (Obata et al., 1974) (Fig. 10), although a high temperature (1,160~1,200 °C) is inferred using the thermometer of Loucks (1996). The olivine gabbro band-forming melt (MORB-like melt) intruded at such high-temperature conditions of the uppermost mantle section (> 800 °C) at the outskirts of the paleo-ridge axis. Differences in appearance of MTZs［i.e., a diffused transition from the olivine gabbro band to its aureole harzburgite in Wadi Thuqbah (Fig. 2a), and a sharp transition in Wadi Fizh (cf. Akizawa et al., 2012)］are possibly derived from the difference in temperature of wall harzburgites, higher at the segment center and lower at the segment end. Therefore, the difference in temperature of the mantle along a ridge segment basically controls the difference in structure and mineral chemical characteristics of MTZs.

6.2. Role of discordant dunite dikes and concordant dunite bands at the base of the mantle section

The Oman ophiolite has undergone several off-ridge magmatic processes at the outskirts of the ridge axis until the end of obduction (e.g. Nicolas, 1989). A part of the mantle section has been overprinted by off-ridge magmatism. Based on their specific chemical signature, discordant dunite dikes and concordant dunite bands at the basal section are expected to represent melt channels for off-ridge magmatism. For a comparison with the melt migration process beneath the ridge axis, we discuss here the roles of such dunites as melt channels off the ridge.

Minerals in the discordant dunite dike and its aureole harzburgite in outcrop T-10 are highly depleted in major elements, and overlap with those in boninites in chemical space (Fig. 5). Additionally, clinopyroxenes have trace-element compositions indicating equilibrium with boninitic melts: depletion in high-field-strength elements (Zr and Ti)

and enrichment in Sr (Fig. 9a). Such boninitic melt occasionally precipitated lens-shaped coarse orthopyroxenes in the dunite channel, and diffused into the wall peridotite to some extent to form high-Cr# spinels (up to 0.8 Cr#) and clinopyroxenes in equilibrium with the boninites (Fig. 9a). On the other hand, the aureole harzburgite has been scarcely metasomatized by boninitic melt infiltration in outcrop T-10 (Figd. 5d and f), indicating that infiltration was restricted within a few meters away from the boninitic melt channel.

The concordant dunite bands in outcrops Z-1 and F-6 are similar in mineral chemical characteristics to the discordant dunite dike (Figs 5 and 8g-h) despite the temporal difference (i.e., concordant dunite band formation predated discordant dunite dike formation). Additionally, the ambient harzburgites are also similar in mineral chemical characteristics to the discordant dunite dike ((Figs. 8g and h). Outcrops Z-1 and F-6 are located close to the "highly depleted area" (Fig. 1), where the peridotites are highly depleted (Cr# > 0.7) due to boninitic melt migration (Suetake & Takazawa, 2012; Takazawa, 2012). The pervasive activity of arc-related boninitic melt possibly modified both older concordant dunite bands and surrounding peridotites. Large dunite bodies (more than a few tens of meters in dimension) and discordant dunite dikes are dominant in the northern Fizh massif (Takazawa, 2012), and are possibly remnants of the migration of arc-related melt, which chemically modified large amounts of peridotites, including outcrops Z-1 and F-6.

In the basal section along Wadi Rayy (outcrop Ry-1), both concordant dunite bands and ambient harzburgite are highly depleted in major and trace elements (Figs. 5 and 9b). Thick concordant dunite bands (< 400 cm) are particularly abundant (Fig. 2g), and small chromitites and orthopyroxenite pockets are occasionally observed in the dunite bands in outcrop Ry-1 (Figs. 2h and i). These features are ascribed to subduction-related remelting of residual mantle peridotites, with the generation of depleted melt by hydrous remelting of the residual peridotites, and subsequent transportation of the melt upward with efficient melt suction through the dunite channel. The generation of a large amount of depleted melt possibly occurred around Wadi Rayy, judging from the presence of frequent thick concordant dunite bands and their surrounding highly depleted harzburgites.

The melts generated around the basal section of the northern Oman ophiolite migrated upward through the dunite channel with melt/mantle interactions, which are

recorded in outcrops T-10, Z-1 and F-6. Correspondingly, the boninitic dikes (Ishikawa et al., 2002) and WNW-trending dikes crosscutting pre-existing NS-trending sheeted dike complex were emplaced between Wadi Rajmi and Wadi Zabin in the northern Oman ophiolite (MacLeod & Rothery, 1992; Adachi & Miyashita, 2003). Extensive deformation (flattening) related to the emplacement of the Oman ophiolite made the dunite channels concordant in the basal section, where dunites and peridotites were subjected to low-temperature deformation, and show mylonitic microstructures in outcrop Ry-1 (e.g. Nicolas et al., 2000; Takazawa et al., 2003).

Concordant dunite bands are less frequent in the basal section in Wadi Umm al Hasa (outcrop U-1) and Wadi Khudayrah (outcrop K-1). When present, the concordant dunite bands, together with the ambient harzburgites, also show subduction-related mineral chemistry signatures (Figs. 5 & 9c-d). The difference between Wadi Rayy and the other two localities (Wadis Umm al Hasa and Khudayrah) indicates that the subduction-related hydrous remelting of residual peridotites has occurred in a heterogeneous, possibly finger-like, way (Suetake & Takazawa, 2012; Takazawa, 2012). Such finger-like thermal and chemical structures of the mantle have been reported from the present-day subduction zone of the NE Japan arc (Tamura et al., 2002; Tamura, 2003). Detailed discussion on off-ridge melt generation related migration process is, however, beyond the scope of this thesis.

6.3. Melting process of peridotites

6.3.1. Numerical modeling of the fractional melting process

I utilize trace-element concentrations of clinopyroxenes for modeling the fractional melting process of peridotites in the way of Ozawa (2001), of which the mass conservation equation incorporates modal compositions of rock. I assume that the melting starts from garnet stability field to duplicate abruptly inclining trace-element pattern of clinopyroxene in the peridotites from the northern Oman ophiolite (e.g. Johnson et al., 1990). Depleted MORB mantle (DMM), the oissible source reservoir of MORB, is chosen for a starting chemical composition of the source material (Workman & Hart, 2005), which is garnet peridotite in mode (Johnson et al., 1990). The source mantle (DMM) adiabatically uprises with the potential temperature of 1,473 °C

determined by pMELTS modeling (cf. Ghiorso et al., 2002; Kimura & Sano, 2012), but lower temperature (approximately 1,280-1,400 °C) was suggested by experimental works (e.g. McKenzie & Bickle, 1988; Herzberg et al., 2007). A melting mode of the garnet peridotite at garnet stability field is from Walter (1998). The rapid conversion from the garnet peridotite to spinel peridotite is conducted by sub-solidus breakdown of garnet and olivine into two pyroxenes and spinel with a low melt/rock ratio. Weight fraction of the breakdown equation is from Takazawa et al. (1996). The following fractional melting of the spinel peridotite is separated into two stages in terms of melting mode; melting of two pyroxenes and spinel with crystallizing of olivine converts to melting of only olivine and spinel when clinopyroxenes are completely consumed with decreasing pressure (Falloon et al., 2008). The melting parameters used in the numerical modeling are compiled in Table 9.

To duplicate the ideal fractional melting process, partial melts generated in the solid matrix are quickly separated (dimensionless melt separation rate: $\gamma = 1$). A trace amount of olivine and clinopyroxene is crystallized with the same fraction from final trapped melt in the solid matrix after the end of melting (final trapped melt fraction: $\alpha_{fin} = 0.001$, its separation rate: $\tau = 1.0 \times 10^{-6}$). I adopted HREE contents of clinopyroxene in the ambient harzburgites for estimating its melting degree, because HREE are less mobile during later metasomatism and weathering than MREE and LREE (e.g. Hellebrand et al., 2001). I compiled these HREE contents in Figure 11 with modeling results, showing changes of Yb, Dy and Gd in clinopyroxene during the ideal fractional melting of mantle peridotite with a range of melting degrees in the garnet stability field from 0 % to 10 %. In the garnet stability field, melting degrees of 7-10 % (7-10 $\%_{Grt}$) at the segment center and 5-7 $\%_{Grt}$ at the segment end are statistically consistent with the data; we applied a melting degree of 7 $\%_{Grt}$ in modeling for all samples for simplicity. The estimated range of total melting degree of the ambient harzburgites in the northern Oman ophiolite is from approximately 19 to 23 % (Figs. 11a-b). Clinopyroxenes in the residual peridotites are completely exhausted at approximately 21 % during the ideal fractional melting process. This result is compatible with the microscopic observations of the ambient harzburgites, i.e., they contain interstitial clinopyroxenes (possibly residual clinopyroxene) between olivines (Fig. 4g) in the lower mantle section, but not in the uppermost mantle section (Fig. 4f). The numerical modeling of fractional melting successfully duplicates the natural system in terms of clinopyroxene consumption. The

modal amount of orthopyroxene in the ambient harzburgites is, however, low in comparison with the results of the numerical modeling (Fig. 11c).

6.3.2. A variety of melting processes of peridotite along the ridge segment

The results of the numerical modeling for fractional melting are shown in Figures 11-13. The ambient harzburgites are depleted up to 23 % in melting degree (Figs. 11a and b), but most of them are more enriched, to varying extents, in LREE than fractionally melted peridotites (Figs. 7a-b and 8a-d). This enrichment has two realistic possible causes, later metasomatism by off-ridge magmas or entrapment of interstitial melt fraction when melting ends (cf. Ozawa & Shimizu, 1995). The ambient harzburgites are expected to have no or little overprint by the off-ridge magmas, because we carefully collected them to eliminate metasomatic effect. I suppose that the enrichment was due to insufficient melt separation after melting at the uppermost mantle section. However, the amount of final trapped melt fraction was insufficient to form rocks rich in melt components such as troctolite, gabbro and wehrlite, and was efficiently separated after crystallization of small amount of clinopyroxene in the ambient peridotite.

I observed an upward decrease in Mg#, and increase in Al_2O_3 and Cr_2O_3 contents of clinopyroxene in the ambient harzburgites (Figs. 5h and j), although the reverse trends (increasing Mg# and decreasing Al_2O_3 and Cr_2O_3) are expected in residual mantle peridotite as fractional melting proceeds (e.g. Jaques & Green, 1980). The observed chemical characteristics are possibly related to a contribution from melting of orthopyroxenes; generated partial melts were enriched in Al_2O_3 and Cr_2O_3 at lower pressure, and precipitated clinopyroxene adjacent to the residual orthopyroxene (Fig. 4f). This phenomenon is consistent with the enrichment of Al_2O_3 and Cr_2O_3 in the MORB-like melts that were involved in the MTZ formation (Figs. 5g and i) as well as with the experimental results (e.g. Falloon et al., 2008).

The ambient harzburgite clinopyroxenes are more depleted in LREE to MREE at the segment center than at the segment end, where some ambient harzburgites contain clinopyroxenes with high concentrations of LREE to MREE (Figs. 8e and i-l). These high concentrations are possibly related to either an early breakdown of garnet during fractional melting of the mantle peridotite, where LREE are comparatively preserved than HREE (Fig. 12), or an insufficient melt separation from the residual peridotite,

which effectively makes the clinopyroxene enriched in only LREE there (e.g. Ozawa & Shimizu, 1995). In any case, the evolutional process of the uppermost mantle peridotite is more complicated at segment ends than at the segment center.

6.4. Melt migration process through the replacive dunite channel beneath a mid-ocean ridge

The irregular-shaped orthopyroxene in the concordant dunite bands (Fig. 5e) is interpreted as a product of reaction at low pressures between peridotite and silica-undersaturated melts generated at higher pressures (e.g. Nicolas & Prinzhofer, 1983). The aureole harzburgites of the concordant dunite bands also contain irregular shaped orthopyroxenes, which are smaller than those in the ambient harzburgites. These features indicate a replacive origin of the dunite, rather than a simple residual origin or a cumulate origin (Kelemen et al., 1997).

6.4.1. Numerical modeling of the dunite channel formation process

I also apply the numerical modeling of Ozawa (2001) for duplicating trace-element patterns of clinopyroxene in the concordant dunite bands. The DMM is also chosen for the starting chemical composition of a source material, which is garnet peridotite in mode (Table 9). I assume "influx melting" for forming the replacive dunite channel; the source mantle (DMM) proceeds to melt until changing to dunite with influx and separation of melts in various degrees (= open magmatic system). I consider that the dunite band and its ambient harzburgite passed through the same melting path; the same degree of melting at garnet stability field (0-7 $\%_{Grt}$) and at spinel stability field (7 $\%_{Spl}$ to the end of melting) (Fig. 14a). An influx of melt starts to flow into the DMM from the beginning of melting in the modeling. Melting mode and breakdown equation of the influx melting at garnet stability field are the same as those in the fractional melting for simplicity (Table 9). I assume more efficient melting of pyroxenes coupled with crystallization of olivine at spinel stability field to consume most of the pyroxenes to duplicate the replacive dunites. Such efficient melting of pyroxenes is stopped at 17$\%_{Spl}$ melting, because some concordant dunite bands contain a trace amount of residual orthopyroxenes (Fig. 4e). Trace amounts of olivine and clinopyroxene are crystallized

with the same fraction from the final trapped melt in the solid matrix when the influx melting ends. The influx melting parameters used in the numerical modeling are compiled in Table 9.

A small melt fraction (up to 2 % in volume) is inevitable to be maintained as melt channels in mantle section (Hart, 1993), and chemically isolated from surrounding residual peridotites (e.g. Iwamori, 1993; Kelemen et al., 1995). I assume low melt influx rate ($\beta = 0.01$) and high melt separation rate ($\gamma = 1.01$) for the influx melting process (Fig. 13). Depending on the stratigraphic level and paleoridge segment structure, these values are changeable as mentioned below.

The spoon-shaped trace-element pattern of clinopyroxene in the concordant dunite band is specific to the lower to middle mantle section at the segment center (Figs. 7e and f), and is expected to be one of indicators to constrain the composition of melt influx involved. Such a trace-element pattern is only available by a LREE-enriched melt influx and its crystallization when the influx melting ends (Fig. 13b). The LREE-enriched melt influx (influx A) is acquired by 1% batch melting of the DMM at garnet stability field (Fig. 14b). On the other hand, the moderately declining trace-element pattern of clinopyroxene in the concordant dunite band is dominant at the middle to uppermost mantle section at the segment center (Figs. 7b and d) as well as at the segment end (Figs. 8a, b, f, i and k). Such a trace-element pattern requires comparatively LREE-depleted melt influxes, which are acquired by accumulating melts from the lower influx melting systems; influxes are assumed to be accumulated from 0-7 $\%_{Grt}$ and 7-17 $\%_{Spl}$ influx melting of DMM with flowing influx A with parameters of $\beta = 1$, $\gamma = 2$, $\alpha_{fin} = 0.001$ and $\tau = 1.0\times10^{-6}$ (influx B), and with $\beta = 0.01$, $\gamma = 1.01$, $\alpha_{fin} = 0.001$ and $\tau = 1.0\times10^{-6}$ (influx C). Influx B and E-MORB are alike in trace-element composition, whereas influx C and N-MORB are alike (Fig. 14b). The compositions of influx are shown in Table 9.

6.4.2. A variety of melt migration processes along the ridge segment

Interstitial clinopyroxenes (Fig. 4a) are rarely present in the concordant dunite bands due to efficient melt removal through the influx melting process. Thus, we expect no or little metasomatic effect on the chemistry of the surrounding mantle peridotite (e.g., nil TiO_2 in chromian spinel; Fig. 5d). We suppose that the replacive dunite channel

efficiently transported partial melts (parental MORB melts) generated by adiabatic decompression and melting of the mantle peridotite. Whatever the shape of the dunite channels, they are distributed in a fractal tree mode below a mid-ocean ridge, based on the field observation of the Oman ophiolite, i.e., concordant dunite bands decrease in frequency and increase in thickness upward (e.g. Kelemen et al., 2000; Braun & Kelemen, 2002).

The MTZ dunite mineral chemistry is equilibrated with N-MORB (Figs. 6a and b), but other dunites in the mantle section below the MTZ are not (Figs. 7-9). The dunite bands below the MTZ are too depleted in clinopyroxene trace elements to have mainly drained parental MORB melts as shown in Figure 13a; a large amount of melt influx ($\beta = 1$) increases the trace-element content of clinopyroxene in the dunite channel, even if the melt influx was efficiently separated ($\gamma = 2$) and final trapped melt was completely separated. The parental MORB melts, which were generated beneath the ridge center by diapiric mantle upwelling, were mainly drained through the MTZ dunite (not the dunite band). Thick dunite channels were dominantly distributed beneath the segment center, and a thick MTZ was constructed there (Fig. 15). The MTZ dunite possibly contained a large amount of melt fraction (up to approximately 10 % in volume) just below the crustal section (Dunn et al., 2000).

On the other hand, the numerical modeling suggests that the concordant dunite bands below the MTZ efficiently transported LREE-enriched melts generated at high-pressure conditions (high-P MORB melt) to shallower level of the mantle section (less than 10 km from the base of the crustal section), as mentioned above. The high-P MORB melt influx gave rise to the spoon-shaped trace-element pattern of clinopyroxene in the replacive dunite channel (Figs. 13b and c). Such LREE-enriched melts could migrate to the surface after aggregation, mixing, melt/wall rock interaction and crystallization processes (Fig. 15b), which possibly caused compositional variations of effusive rocks at the scale of a few kilometers to a few tens of kilometers off axis (e.g. Geshi et al., 2007).

Some concordant dunite bands have preserved traces of not only LREE-enriched melt migration, but also of MORB-like melt migration as stated above. The gentle trace-element slope from HREE to LREE of clinopyroxene requires a LREE-depleted melt influx and its stagnation in the dunite channel ($\beta = 0.1$-0.2, $\gamma = 0.1$) after the LREE-enriched melts migration (Figs. 13a and d-f). The coarse clinopyroxene with

orthopyroxene blebs in the thick concordant dunite band (250 cm) in outcrop T-4 in the uppermost mantle section (Fig. 4d) is interpreted as a reaction product between melt and orthopyroxene porphyroclast in the mantle peridotite with high melt/rock ratio (cf. Akizawa et al., 2012). This textural feature is one of the indicators of melt stagnation at the shallower level of the mantle section. A decrease in Cr# of chromian spinel in the concordant dunite bands from the lower mantle section (< 0.7) to the uppermost mantle section (> 0.4) is also a result of melt stagnation in the dunite channels; melt components were largely supplied from the melt influx to the chromian spinels of the dunite channel (Figs. 5c and e). The sufficient melting of orthopyroxenes also affected the composition of melt influx in the dunite channel in the uppermost mantle section, a decrease of Mg#, and an increase of Al_2O_3 and Cr_2O_3 of precipitated clinopyroxene (Figs. 5g and i).

The mantle potential temperature is assumed to have been higher at the segment center than at the segment end because of the diapiric mantle upwelling. The ambient harzburgites are all depleted in modal and chemical compositions at the segment center, whereas the degree of depletion is more variable at the segment end as stated above. At the segment end, uppermost mantle peridotites display highly depleted modal and chemical compositions, regardless of heterogeneous features in the underlying mantle section, where lherzolites (low melting-degree peridotite) were also reported (Takazawa et al., 2003). Highly depleted uppermost mantle harzburgites were possibly transported from the segment center by horizontal mantle flow outward of the diapiric zone (Fig. 15a). Accordingly, some concordant dunite bands were also transported from the segment center.

In outcrop R-2, the trace-element compositions (LREE to MREE) of clinopyroxene in thin concordant dunite bands (< 1cm) and the thick ones (< 20 cm) are different (Fig. 8f). This difference is ascribed to a difference in the flux flowed through the replacive dunite channel; a small flux through the thin dunite channels, and a large one through the thick dunite channels (Fig. 13e). The thin dunite channels could be more fragile than the thick one, and easily transformed into peridotite (i.e., homogenization). However, they were essential to drain generated partial melts upward, and were dominant at the segment end (Fig. 15c). Clinopyroxenes with high concentrations of LREE to MREE in the ambient peridotites at the segment end Figs. 8a-b, f, g-i and k) are possibly derived from such former melt channel. Additionally, the

depletion of modal pyroxenes in ambient harzburgites compared with that calculated in the model is possibly due to a dilution effect by such homogenization of former melt channel with the surrounding residual peridotite (Fig. 11c). On the other hand, the thick dunite channels (> a few tens of centimeters) were more dominant at the segment center than at the segment end (Figs. 15b and c).

6.5. Ultra-depleted melt migration in the uppermost mantle section beneath a mid-ocean ridge

Some concordant dunite bands are associated with orthopyroxene-rich rocks in the middle to uppermost mantle section: the orthopyroxenite lens along the center and boundary of the concordant dunite band in outcrop T-2 (Fig. 2f), and the orthopyroxene-rich harzburgite along the boundary of the concordant dunite band in outcrop T-5. However, no difference has been found in major-element composition between such concordant dunite bands and others (Figs. 5c, e, g and i), whereas clinopyroxenes are extremely depleted in trace elements in the concordant dunite bands that are associated with opx-rich rocks (Figs. 7a and c). The orthopyroxene-rich rocks are supposed to be related to a highly depleted melt, i.e., ultra-depleted melt (e.g. Sobolev & Shimizu, 1993) flowing along the replacive dunite channel beneath the ridge axis. Such ultra-depleted melts were possibly supplied from the restite of the fractional melting of peridotites.

Other dunite bands also contain similar trace-element-depleted clinopyroxenes in outcrops T-3, R-1, H-1, S-2 and S-4 (Figs. 7b, 8d-e, 8j and 8l). They are not associated with orthopyroxene-rich rocks, although the ultra-depleted melts were involved, when the trace-element-depleted clinopyroxene was crystallized in the dunite channel. Such concordant dunite bands are generally thin (up to approximately 30 cm) compared to the other concordant dunite bands (up to approximately 250 cm) at the same stratigraphic level. The thin dunite channels, transporting the ultra-depleted melt upward, were either newly formed or the migrating melt composition has changed from MORB-like melt to the ultra-depleted melt through time. Ultra-depleted melts, however, have less ability to dissolve pyroxenes and cause their chemical variability, e.g., 0.45 ~

0.60 Cr# (Fig. 5c). Therefore, some dunite channels began to drain ultra-depleted melts, instead of the MORB-like melt, at various depths (Figs. 15b and c).

The gabbronoritic dikes precipitating from a highly depleted melt have been reported from the mantle section away from the center of mantle diapirs in the Oman ophiolite (Benoit et al., 1999; Python & Ceuleneer, 2003). Furthermore, highly depleted melt inclusions in olivine have been reported from the MORBs (e.g. Sobolev & Shimizu, 1993). Highly depleted melts are commonly generated in the mantle and contribute to constructing oceanic crust at the ridge axis.

6.6. Melt migration process through fracture-related melt channels

6.6.1. Numerical modeling of fracture-related channel formation process

In the uppermost mantle section at the segment end (outcrop F-5), the aureole harzburgite of the thin (< 1 cm) concordant dunite band (Fig. 2c) contains a relatively high amount of clinopyroxene, and some composite grains of clinopyroxene and orthopyroxene (Fig. 5b). Trace-element patterns of the clinopyroxene are exceptionally heterogeneous in the aureole harzburgite (Fig. 8a). These features indicate chromatographic melt percolation into the wall rock along a fracture (e.g. Navon & Stolper, 1987).

To unravel the behavior of chromatographic melt percolation, I conducted a numerical modeling using a simplified "plate model" of Vernières et al. (1997) (e.g. Tamura et al., 2008), by using trace-element compositions of clinopyroxene. I assume that a melt in equilibrium with clinopyroxene of the MTZ dunite percolates into a highly depleted wall harzburgite with a gradual melt/rock ratio decreasing away from the band. The initial trace-element composition of the percolating melt ($C_{melt\ 0}$) is determined so that it is in equilibrium with the clinopyroxene of the MTZ dunite, and the initial clinopyroxene composition of the wall harzburgite ($C_{cpx\ 0}$) is from the most depleted harzburgite in Wadi Fizh (cf. Akizawa et al., 2012). The percolating melt composition in the cell number j is assumed as $C_{melt\ j} = (C_{melt\ (j-1)} + \alpha_j C_{cpx\ 0}) / (1 + D\ \alpha_j)$. The clinopyroxene/melt mass ratio (α_j) changes from $\alpha_1 = 0.1$ (cell number = 1) to $\alpha_{14} = 50$ (cell number = 14). Partition coefficients (D) for trace elements between

clinopyroxene and melt, and trace-element compositions for the numerical modeling are compiled in Tables 9 and 10.

6.6.2. Melt migration process through the fracture-related melt channel at the segment end

The modeling duplicates the spoon-shaped trace-element patterns of clinopyroxene in the aureole harzburgite of the thin concordant dunite band (Fig. 16a). The melt, similar to N-MORB in trace-element composition, percolates into the highly depleted wall harzburgite (with about 0.3 vol.% clinopyroxene) with a gradual decrease in melt/clinopyroxene ratio outward from 10 to 0.02 (from about 3 vol.% to 0.006 vol.% melt). The melt percolation is restricted to a few centimeters outward, where composite grains o f clinopyroxene and orthopyroxene were formed as a reaction product (Fig. 4b), and the aureole harzburgite changed into dunite or wehrlite through dunitic harzburgite.

The modeling result shows no convex-upward trace-element pattern with negative Eu anomaly of clinopyroxene like that in the harzburgite about 20 cm above the thin concordant dunite band in outcrop F-5 (Fig. 8a), which is exceptionally associated to orthopyroxene, saussurite and chromian spinel with olivine inclusions (Fig. 4c). Such mineral assemblage is considered as a reaction product between a melt and normal orthopyroxene porphyroclast (opx 1), and consequently, residual orthopyroxene (opx 2) was enriched with trace elements (Fig. 16b).

I conducted a mass balance calculation to understand the reaction to form the composite grain (Fig. 4c). I suppose that the reaction is: N-MORB-like melt (equilibrated with clinopyroxene of the MTZ dunite) + trace-element-depleted orthopyroxene (opx 1) = trace-element-enriched residual orthopyroxene (opx 2) + olivine + new melt, which precipitates clinopyroxene and plagioclase. The reaction, N-MORB-like melt (1) + opx 1 (35) = opx 2 (32) + olivine (2) + new melt (1) (the numbers indicate each phase normalized to the melt in volume) is adequate to form the composite grain (Fig. 16b). In the northern Oman ophiolite mantle, small amount of N-MORB-like melt was directly injected and reacted in various degrees with the wall harzburgite. The melt injected evolved to precipitate clinopyroxene and plagioclase, and minerals were metasomatized in mode and chemistry to some degrees as a function of the degree of interaction.

The fracture-related melt migration was dominant, and greatly contributed to draining N-MORB-like melt upward in the uppermost mantle section at the segment end. The lower geotherm at the segment end allowed fracturing in the uppermost mantle. Minor amounts of melt injected directly into the wall harzburgite at least a few tens of centimeters outward from the fracture. These processes made the uppermost mantle complicated in both modal and chemical compositions at the segment end.

7. SUMMARY AND IMPLICATIONS

I conducted sampling of dunites in the mantle section of the northern Oman ophiolite, which are interpreted as ancient melt channels. The melt channel is assumed to be of replacive origin, neither of residual origin nor of cumulus origin. I summarize petrogenesis of such replacive dunite channels at the mantle section in view of MORB genesis beneath a fast-spreading mid-ocean ridge as follows.

1. The MTZ dunites are equilibrated in mineral chemistry with N-MORB (Figs. 7a and b), but other dunites in the mantle section of the northern to central Oman ophiolite are not. The MTZ dunite mainly drained partial melts (parental MORB melt) generated by adiabatic decompression and melting of the mantle peridotite to form MORB. The diapiric mantle upwelling concentrated the partial melts beneath the segment center, where thick dunite channels were dominantly distributed and efficiently drained the partial melts. The thick MTZ of the segment center is derived from such a thick dunite channels (MTZ dunite channels) placed in the center of mantle diapir.

2. Numerical modeling (1-D steady state modeling: Ozawa, 2001) clearly shows that the concordant dunite bands below the MTZ transported the parental MORB melts upward, but the flux into the thin dunite channels (up to several meters in thickness) was smaller than that into the MTZ dunite channels. LREE-enriched melts generated at high-pressure conditions (high-P MORB melt) migrated to a shallower level of the mantle section (less than 10 km from the base of the crustal section = shallower mantle section) through such thin dunite channel. The thin dunite

channels are important for efficiently draining the high-P MORB melts generated several tens of kilometers below the crust/mantle boundary (ca. 60-70 km).

3. Fractional melting of the mantle peridotite ultimately generates highly depleted melts and residual peridotites at the shallower mantle section, where melt channels were insufficient in frequency to drain all the highly depleted melts. Consequently, some melts stagnated in the residual peridotite. However, some dunite channels drained highly depleted melts instead of MORB melts, and occasionally left orthopyroxenes as a reaction product in the channel. High-P MORB melts were mingled with highly depleted melts in the dunite channels in the shallower mantle section to generate N-MORB at the ridge axis (Fig. 2f).

4. Few centimeters-scale dunite channels were dominant at the segment end, but they were fragilely disconnected from the melt migration system, and easily transformed into (homogenized with) the mantle peridotite because of a low melt influx rate during the mantle upwelling. The clinopyroxenes with high concentrations of LREE to MREE in the ambient peridotites at the segment end (Fig. 12) are possibly derived from the former few centimeters-scale melt channels. On the other hand, the meter-scale dunite channels, which transported larger amounts of melts upward and transformed into concordant dunite band/lens, were more dominant at the segment center than at the segment end (Fig. 15).

5. Fracture-related melt migration occurred in the uppermost mantle section at the segment end. Thin dunitic rim (up to a few centimeters) was formed as a reaction product along the fracture. The aureole harzburgite contains a relatively high amount of clinopyroxene and composite grains of clinopyroxene and orthopyroxene (Fig. 4b), which are reaction products between N-MORB-like melt and depleted harzburgite with a low melt/rock ratio (Fig. 16). The N-MORB-like melt chromatographically percolated into the wall harzburgite, and additionally, a small amount of N-MORB-like melt was directly injected into harzburgite and metasomatized it in various degrees, which results in a more complicated (in modal and chemical compositions) suite of uppermost mantle rocks at the segment end than at the segment center.

6. Difference in thermal gradient possibly occurred at a given depth along the paleo-ridge segment due to the oval dome-like mantle diapir; higher at the segment center and lower at the segment end at the same stratigraphic level. Highly depleted peridotites generated at the center of the mantle diapir are transported outward by horizontal mantle flow (Fig. 15). Therefore, at the segment end, the uppermost mantle peridotites are extensively replaced by the highly depleted peridotites, whereas the deeper mantle peridotites are heterogeneous in modal and chemical compositions along the paleo-ridge axis.

8. NOTATION

1-D steady state modeling (Ozawa, 2001)

β: dimensionless melt influx rate
γ: dimensionless melt separation rate
α_{fin}: melt fraction when melting ends.
τ: melt separation rate during trapped melt crystallization.
η: total melt mass influxed at a given melting degree.
ζ: total melt mass separated at a given melting degree.

9. ACKNOWLEDGEMENTS

I especially thank my supervisor, Professor S. Arai (Kanazawa University) for encouragement, discussions and suggestions given throughout this study. This thesis has been greatly improved by his comments. He provided me with a lot of chances for field works abroad (Oman, 9 times; UK, twice; and Turkey, twice) as well as for attending international conferences (SINGAPORE in 2009 and 2012, Asia Oceania Geoscience Society; Budapest, HUNGARY in 2010, International Mineralogical Association; Vienna, AUSTRIA in 2011 and 2013, European Geosciences Union; Prague, CZECH in 2011, Goldschmidt; Muscat, OMAN in 2012, International Conference on the Geology

of the Arabian Plate and the Oman mountain; Brisbane, AUSTRALIA in 2013, Asia Oceania Geoscience Society; and Florence, ITALY in 2013, Goldschmidt).

I thank Dr. A. Tamura (Kanazawa University) for discussions and suggestions. He also greatly assisted me with LA-ICP-MS analysis.

I conducted the numerical modeling under the supervision of Prof. K. Ozawa (Tokyo University). He gave me constructive and insightful comments, which greatly improved this study.

Prof. K. Michibayashi (Shizuoka University) and Mr. Y. Kondo (Shizuoka University) supported me in EBSD analysis at Shizuoka University. Prof. K. Michibayashi kindly discussed with me on the results of petrofabric analysis.

I am grateful to Prof. S. Umino (Kanazawa University), Prof. T. Morishita (Kanazawa University), Dr. T. Mizukami (Kanazawa University), Dr. S. Ishimaru (Kumamoto University), Dr. Y. Soda (Kanazawa University), Prof. S. Miyashita (Niigata University), Prof. E. Takazawa (Niigata University) and Dr. Y. Kusano (Kanazawa University) for discussions and suggestions.

Dr. B. Ildefonse (Université Montpellier 2) and Dr. M. Godard (Université Montpellier 2) assisted me to improve this study during my visits to Université Montpellier 2. They kindly encouraged me to express my scientific results in English.

Mr. H. Negishi (Kanazawa University), Mr. M. Miura (Kanazawa University), Mr. C. Hoshikawa (Kanazawa University), Ms. R. Muroi (Kanazawa University), Dr. Y. Adachi (Niigata University), Dr. M. Python (Hokkaido University), Dr. M. Z. Khedr (Kanazawa University) and Dr. K. Abbou-Kebier (Kanazawa University) assisted me in my field expedition to Oman.

I am also grateful to Mr. Salim Al Busaidi and other people of the Ministry of Commerce and Industry, Sultanate of Oman for their hospitality and assistance. Dr. D. Mainprice (Université Montpellier 2) provided software for analyzing/plotting the CPO data.

This study was supported in part by Grant-in-Aid for Scientific Research (20244085), Grant-in-Aid for Creative Scientific Research (20244085) and Grant-in-aid for JSPS Fellows (11J04217).

10. REFERENCES

Adachi, Y. & Miyashita, S. (2003) Geology and petrology of the plutonic complexes in the Wadi Fizh area: multiple magmatic events and segment structure in the northern Oman ophiolite. *Geochemistry Geophysics Geosystems* **4**, 8619, doi: 10.1029/2001GC000272.

Akizawa, N. & Arai, S. (2009) Petrologic profile of a peridotite layer under a possible Moho in the northern Oman ophiolite: An example from Wadi Fizh. *Journal of Mineralogical and Petrological Sciences* **104**, 389-394.

Akizawa, N., Arai, S. & Tamura, A. (2012) Behavior of MORB magmas at uppermost mantle beneath a fast-spreading axis: An example from Wadi Fizh of the northern Oman ophiolite. *Contributions to Mineralogy and Petrology* **164**, 601-625.

Arai, S. (1994) Characterization of spinel peridotites by olivine-spinel compositional relationships: Review and interpretation. *Chemical Geology* **113**, 191-204.

Arai, S. (2005) Role of dunite in genesis of primitive MORB. *Proceeding of the Japan Academy,* Series B, **81**, 14-19.

Arai, S., Kadoshima, K. & Morishita, T. (2006) Widespread arc-related melting in the mantle section of the northern Oman ophiolite as inferred from detrital chromian spinels. *Journal of the Geological Society* **163**, 869-879.

Barth, G. A. & Mutter, J. C. (1996) Variability in oceanic crustal thickness and structure: Multichannel seismic reflection results from the northern East Pacific Rise. *Journal of Geophysical Research* **101**, 17,951-17,975.

Benoit, M., Ceuleneer, G. & Polvé, M. (1999) The remelting of hydrothermally altered peridotite ay mid-ocean ridges by intruding mantle diapirs. *Nature* **402**, 514-518.

Boudier, F. & Nicolas, A. (1995) Nature of the Moho transition zone in the Oman ophiolite. *Journal of Petrology* **36**, 777-796.

Braun, M. G. & Kelemen, P. B. (2002) Dunite distribution in the Oman ophiolite: Implications for melt flux through porous dunite conduits. *Geochemistry Geophysics Geosystems* **3**, 8603, doi: 10.1029/2001GC000289.

Cassard, D., Nicolas, A., Rabinovitch, M., Moutte, J., Leblanc, M. & Prinzhofer, A. (1981) Structural classification of chromite pods in southern New Caledonia. *Economic Geology* **76**, 805-831.

Ceuleneer, G. (1986) Structure des ophiolites d'Oman: Flux mantellaire sous un centre d'expansion océanique et charriage à la dorsale. Unpublished *thèse de Doctorat*, Université de Nantes, 338 pp (in French).

Ceuleneer, G., Nicolas, A. & Boudier, F. (1988) Mantle floe patterns at an oceanic spreading center: The Oman peridotites record. *Tectonophysics* **151**, 1-26.

Chadam, J., Hoff, D., Merino, E. Ortoleva, P. & Sen, A. (1986) Reactive infiltration instability. *IMA Journal of Applied Mathematics* **36**, 207-221.

Collier, M. L. & Kelemen, P. B. (2010) The case for reactive crystallization at mid-ocean ridges. *Journal of Petrology* **51**, 1,913-1,940.

Dunn, R. A., Toomey, D. R. & Solomon, S. C. (2000) Three-dimensional seismic structure and physical properties of the crust and shallow mantle beneath the East Pacific Rise at 9°30′N. *Journal of Geophysical Research* **105**, 23,537-23,555.

Falloon, T., Green, D., Danyushevsky, L. D. & McNeill, A. W. (2008) The composition of near-solidus partial melts of fertile peridotite at 1 and 1.5 GPa: Implications for the petrogenesis of MORB. *Journal of Petrology* **49**, 591-613.

Forsyth, D. W., Webb, S. C., Dorman, L. M. & Shen, Y. (1998) Phase velocities of Rayleigh waves in the MELT experiment on the East Pacific Rise, *Science* **280**, 1,235-1,238.

Geshi, N., Umino, S., Kumagai, H., Sinton, J. M., White, S. M., Kishimoto, K. & Hilde, T. W. (2007) Discrete plumbing systems and heterogeneous magma sources of a 24 km^3 off-axis lava field on the western flank of East Pacific Rise 14°S. *Earth and Planetary Science Letters* **258**, 61-72.

Ghiorso, M. S., Hirschmann, M. M., Reiners, P. W. & Kress, V. C. (2002). The pMELTS: A revision of MELTS for improved calculation of phase relations and major element partitioning related to partial melting of the mantle to 3 GPa. *Geochemistry Geophysics Geosystems* **3**, doi:10.1029/2001GC000217.

Girardeau, J. Monnier, C., Launeau, P. & Quatrevaux, F. (2002) Kinematics of mantle flow beneath a fossil overlapping spreading center: The Wuqbah massif case, Oman ophiolite. *Geochemistry Geophysics Geosystems* **3**, doi: 10.1029/2001GC000228.

Grove, T. L., Kinzler R. J. & Bryan W. B. (1992) Fractionation of mid-ocean ridge basalt (MORB). In: Morgan, J. P., Blackman, D. K. & Sinton, J. M. (eds.)

Mantle Flow and Melt Generation at Mid-Ocean Ridges, *Geophysical Monograph* **71**, American Geophysical Union, Washington D.C., 281-310.

Hart, S. R. (1993) Equilibration during mantle melting: A fractal tree model. *Geology* **90**, 11,914-11,918.

Hellebrand, E., Snow, J. E., Dick, H. J. B. & Hofmann, A. W. (2001) Coupled major and trace elements as indicators of the extent of melting in mid-ocean-ridge peridotites. *Nature* **410**, 677-681.

Hellebrand, E., Snow, J. E., Hoppe, P. & Hofman, A. W. (2002) Garnet-field melting and late-stage refertilization in 'residual' abyssal peridotites from the Central Indian Ridge. *Journal of Petrology* **43**, 2,305-2,338.

Herzberg, C., Asimow, P. D., Arndt, N., Niu, Y., Lesher, C. M., Fitton, J. G., Cheadle, M. J. & Saunders, A. D. (2007). Temperatures in ambient mantle and plumes: Constraints from basalts, picrites, and komatiites. *Geochemistry Geophysics Geosystems* **2**, doi:10.1029/2006GC001390.

Ishida, Y., Morishita, T., Arai, S. & Shirasaka, M. (2004) Simultaneous in-situ multi-element analysis of minerals on thin section using LA-ICP-MS. *The Science Report of Kanazawa University* **48**, 31-42.

Ishikawa, T., Nagaishi, K. & Umino, S. (2002) Boninitic volcanism in the Oman ophiolite: implications for thermal condition during transition from spreading ridge to arc. *Geology* **30**, 899-902.

Iwamori, H. (1993) A model for disequilibrium mantle melting incorporating melt transport by porous and channel flows. *Nature* **366**, 734-737.

Jaques, A. L. & Green, D. H. (1980) Anhydrous melting of peridotite at 0-15 kb pressure and genesis of Tholeiitic basalts. *Contributions to Mineralogy and Petrology* **73**, 287-310.

Johnson, K. T. M., Dick, H. J. B. & Shimizu, N. (1990) Melting in the oceanic upper mantle: An ion microprobe study of diopsides in abyssal peridotites. *Journal of Geophysical Research* **95**, 2,661-2,678.

Jousselin, D. & Nicolas, A. (2000) The Moho transition zone in the Oman ophiolite-relation with wehrlites in the crust and dunites in the mantle. *Marine Geophysical Researches* **21**, 229-241.

Katz, R. F. (2010) Porosity-driven convection and asymmetry beneath mid-ocean ridges. *Geochemistry Geophysics Geosystems* **11**, Q0AC07, doi: 10.1029/2010GC003282.

Kelemen, P. B., Shimizu, N. & Salters, V. J. M. (1995) Extraction of mid-ocean-ridge basalt from the upwelling mantle by focused flow of melt in dunite channels. *Nature* **375**, 747-753.

Kelemen, P. B., Hirth, G., Shimizu, N., Spiegelman, M. & Dick, H. J. B. (1997) A review of melt migration processes in the adiabatically upwelling mantle beneath oceanic spreading ridges. *Philosophical Transactions of the Royal Society of London*, Series A, **355**, 283-318.

Kelemen, P. B., Braun, M. & Hirth, G. (2000) Spatial distribution of melt conduits in the mantle beneath oceanic spreading ridges: Observations from the Ingalls and Oman ophiolites. *Geochemistry Geophysics Geosystems* **1**, paper number 1999GC000012.

Kelemen, P. B., Yogodzinski G. M. & Scholl D. W. (2003) Along-strike variation in the Aleutian Island Arc: genesis of high Mg# andesite and implications for continental crust. In: Eiler, J. (ed) Inside the Subduction Factory. *Geophysical Monograph* **138**, American Geophysical Union, Washington, 223-276.

Kimura, J.-I. & Sano, S. (2012) Reactive melt flow as the origin of residual mantle lithologies and basalt chemistries in mid-ocean ridges: Implications from the Red Hills peridotite, New Zealand. *Journal of Petrology* **53**, 1,637-1,671.

Klein, E. M. & Langmuir, C. H. (1987) Global correlation of ocean ridge basalt chemistry with axial depth and crustal thickness. *Journal of Geophysical Research* **92**, 8,089-8,115.

Koga, K. T., Kelemen, P. B., Shimizu, N. (2001) Petrogenesis of the crust-mantle transition zone and the origin of lower crustal wehrlite in the Oman ophiolite. *Geochemistry Geophysics Geosystems* **2**, paper number 2000GC000132.

Kushiro, I. (1975) On the nature of silicate melt and its significance in magma genesis: Regularities in the shift of the liquidus boundaries involving olivine, pyroxene, and silica minerals. *American Journal of Science* **275**, 411-431.

Lin, J. & Phipps Morgan, J. (1992) The spreading rate dependence of three-dimensional mid-ocean ridge gravity structure. *Geophysical Research Letter* **19**, 13-16.

Lippard, S. J., Shelton, A. W. & Gass, I. G. (1986) *The ophiolite of northern Oman*. *Memoir* **11**, Geological Society, London, 178 pp.

Loucks, R. R. (1996) A precise olivine-augite Mg-Fe-exchange geothermometer. *Contributions to Mineralogy and Petrology* **164**, 140-150.

Macdonald, K. C., Fox, P. J., Perram, L. J., Eisen, M. F., Haymon, R. M, Miller, S. P., Carbotte, S. M., Cormier, M.-H. & Shor, A. N. (1988) A new view of the mid-ocean ridge from the behavior of ridge-axis discontinuities. *Nature* **335**, 217-225.

Macdonald, K. C., Scheirer, D. S. & Carbotte, S. M. (1991) Mid-ocean ridges: Discontinuities, segments and giant cracks. *Science* **253**, 986-994.

McKenzie, D. & Bickle, M. J. (1988). The volume and composition of melt generation by extension of the lithosphere. *Journal of Petrology* **29**, 625-679.

MacLeod, C. J. & Rothery, D. A. (1992) Ridge axial segmentation in the Oman ophiolite: Evidence from along-strike variations in the sheeted dike complex. In: Parson, L. M., Murton, B. J. & Browning, P. (eds.) *Ophiolites and Their Modern Oceanic Analogues*, *Geological Society Special Publication* **60**, Geological Society, London, 39-63.

Michibayashi, K. & Mainprice, D. (2006) The role of pre-existing mechanical anisotropy on share zone development within oceanic mantle lithosphere: an example from the Oman ophiolite. *Journal of Petrology* **45**, 405-414.

Ministry of Petroleum and Minerals (1992a) *Geological map of Buraymi*, scale 1:250,000, Sultanate of Oman, Muscat.

Ministry of Petroleum and Minerals (1992b) *Geological map of Ibri*, scale 1:250,000, Sultanate of Oman, Muscat.

Miyashita, S., Adachi, Y. & Umino, S. (2003) Along-axis magmatic system in the northern Oman ophiolite: Implications of compositional variation of the sheeted dike complex. *Geochemistry Geophysics Geosystems* **4**, 8617, doi: 10.1029/2001GC000235.

Morishita, T., Ishida, Y. & Arai, S. (2005a) Simultaneous determination of multiple trace element compositions in thin (<30 μm) layers of BCR-2G by 193 nm ArF excimer laser ablation-ICP-MS: implications for matrix effect and elemental fractionation on quantitative analysis. *Geochemical Journal* **39**, 327-340.

Morishita, T., Ishida, Y., Arai, S. & Shirasaka, M. (2005b) Determination of multiple trace element compositions in thin (<30 μm) layers of NIST SRM 614 and 616 using laser ablation-inductively coupled plasma-mass spectrometry (LA-ICP-MS). *Geostandards and Geoanalytical Research* **29**, 107-122.

Navon, O. & Stolper, E. (1987) Geochemical consequences of melt percolation: the upper mantle as a chromatographic column. *Journal of Geology* **95**, 285-307.

Negishi, H., Arai, S., Yurimoto, H., Ito, S., Ishimaru, S., Tamura, A. & Akizawa, N. (2013) Sulfide-rich dunite within a thick Moho transition zone of the northern Oman ophiolite: Implications for the origin of Cyprus-type sulfide deposits. *Lithos* **164-167**, 22-35.

Nicolas, A. & Jackson, M. (1982) High temperature dikes in peridotites: origin by hydraulic fracturing. *Journal of Petrology* **23**, 568-582.

Nicolas, A. & Prinzhofer, A. (1983) Cumulative or residual origin for the transition zone in ophiolites: structural evidence. *Journal of Petrology* **24**, 188-206.

Nicolas, A. (1989) *Structure of Ophiolites and dynamics of Oceanic Lithosphere*. Kluwer Academic, Dordrecht, 367 pp.

Nicolas, A., Boudier, A. & Ildefonse, B. (1996) Variable crustal thickness in the Oman ophiolite: Implication for oceanic crust. *Journal of Geophysical Research* **101**, 17,941-17,950.

Nicolas, A. & Boudier, F. (2000) Large mantle upwellings and related variations in crustal thickness in the Oman ophiolite. In Dilek, Y., Moores, E.M., Elthon, D. & Nicolas, A. (eds.) *Ophiolites and Oceanic Crust: New Insights from Fiels Studies and the Ocean Drilling Program*, *Geological Society of America Special Paper* **349**, Geological Society of America, Colorado, 67-73.

Nicolas, A., Boudier, F., Ildefonse, B. & Ball, B. (2000) Accretion of Oman and United Arab Emirates ophiolite-distribution of a new structural map. *Marine Geophysical Researches* **21**, 147-179.

Obata, M., Banno, S. & Mori, T. (1974) The iron-magnesium partitioning between naturally occurring coexisting olivine and Ca-rich clinopyroxene: an application of the simple mixture modal to olivine solid solution. *Bulletin de la Société Française de Minéralogie et de Cristallographie* **97**, 101-107.

Ozawa, K. & Shimizu, N. (1995) Open-system melting in the upper mantle: Constraints from the Hayachine-Miyamori ophiolite, northeastern Japan. *Journal of Geophysical Research* **100**, 22,315-22,335.

Ozawa, K. (2001) Mass balance equations for open magmatic systems: Trace element behavior and its application to open system melting in the upper mantle. *Journal of Geophysical Research* **106**, 13,407-13,434.

Pearce, N. J. G., Perkins, W. T., Westgate, J. A., Gorton, M. P., Jackson, S. E., Neal, C. R. & Chenery, S. P. (1997) A compilation of new and published major and trace element data for NIST SRM 610 and NIST SRM 612 glass reference materials. *Geostandards Newsletter* **21**, 115-144.

Plank, T. & Langmuir, C. (1992) Effects of the melting regime on the composition of the oceanic crust. *Journal of Geophysical Research* **97**, 19,749-19,770.

Python, M. & Ceuleneer, G. (2003) Nature and distribution of dykes and related melt migration structures in the mantle section of the Oman ophiolite. *Geochemistry Geophysics Geosystems* **4**, 8612, doi:10.1029/2002GC000354.

Quick, J. E. (1981) The origin and significance of large, tabular dunite bodies in the Trinity peridotite, Northern California. *Contributions to Mineralogy and Petrology* **78**, 413-422.

Sleep, N. (1988) Tapping of melt by veins and dikes. *Journal of Geophysical Research* **93**, 10,255-10,272.

Sobolev, A. V. & Shimizu, N. (1993) Ultra-depleted primary melt included in an olivine from the Mid-Atlantic Ridge. *Nature* **363**, 151-154.

Spiegelman, M., Kelemen, P. B. & Aharonov, E. (2001) Causes and consequences of flow organization during melt transport: The reaction infiltration instability in compactible media. *Journal of Geophysical Research* **106**, 2,061-2,078.

Shaw, D. M. (1970) Trace element fractionation during anatexis. *Geochemica et Cosmochimica Acta* **34**, 237-243.

Stolper, E. (1980) A phase diagram for mid-ocean ridge basalts: preliminary results and implications for petrogenesis. *Contributions to Mineralogy and Petrology* **74**, 13-27.

Suetake, A. & Takazawa, E. (2012) Spatial compositional variability and origin of dunites in the Fizh mantle section, the Oman ophiolite. *The Earth Monthly* **134**, 247-251 (in Japanese).

Suhr, G., Seck, H. A., Shimizu, N., Günther, D. & Jenner, G. (1998) Infiltration of refractory melts into the lowermost oceanic crust: Evidence from dunite- and gabbro-hosted clinopyroxenes in the Bay of Island Ophiolite. *Contributions to mineralogy and Petrology* **131**, 136-154.

Suhr, G. (1999) Melt migration under oceanic ridges: Inferences from reactive transport modelling of upper mantle hosted dunites. *Journal of Petrology* **40**, 575-599.

Sun, S. S. & McDonough, W. F. (1989) Chemical and isotopic systematics of oceanic basalts: implications for mantle composition and processes. In: Saunders, A. D. & Norry, M. J. (eds.) *Magmatism in the Ocean Basins*, *Geological Society Special Publication* **42**, Geological Society, London, 313-345.

Takahashi, E. (1986) Origin of basaltic magmas-implications from peridotite melting experiments and an olivine fractional model. *Bulletin of the Volcanological Society of Japan* **30**, S17-S40 (in Japanese with English abstract).

Takazawa, E., Frey, F., Shimizu, N. & Obata, M. (1996) Evolution of the Horoman peridotite (Hokkaido, Japan): Implications from pyroxene compositions. *Chemical Geology* **134**, 3-26.

Takazawa, E., Okayasu, T. & Satoh, K. (2003) Geochemistry and origin of the basal lherzolites from the northern Oman ophiolite (northern Fizh block). *Geochemistry Geophysics Geosystems* **4**, 1021, doi: 10.1029/2001GC000232.

Takazawa, E. (2012) Melting and reaction in an incipient subarc mantle as inferred from the spatial compositional variability in the mantle section of the Oman ophiolite. *Japanese Magazine of Mineralogical and Petrological Sciences* **41**, 257-266 (in Japanese with English abstract).

Tamura, A. & Arai, S. (2006) Harzburgite-dunite-orthopyroxenite suite as a record of supra-subduction zone setting for the Oman ophiolite mantle. *Lithos* **90**, 43-56.

Tamura, A., Arai, S., Ishimaru, S. & Andal, E. S. (2008) Petrology and geochemistry of peridotites from IODP Site U1309 at Atlantis Massif, MAR 30°N: micro- and macro-scale melt penetrations into peridotites. *Contributions to Mineralogy Petrology* **155**, 491-509.

Tamura, Y., Tatsumi, Y., Zhao, D., Kido, Y. & Shukuno, H. (2002) Hot fingers in the mantle wedge: new insights into magma genesis in subduction zones. *Earth and Planetary Science Letters* **197**, 105-116.

Tamura, Y. (2003) Some geochemical constraints on hot fingers in the mantle wedge: evidence from NE Japan. In: Larter, R. D. & Leat, P. T. (eds.) *Intra-oceanic subduction systems: tectonic and magmatic processes*, *Geological Society Special Publication* **219**, Geological Society, London, 221-237.

Toomey, D. R., Jousselin, D., Dunn, R. A., Wilcock, W. S. D. & Detrick, R. S. (2007) Skew of mantle upwelling beneath the East Pacific Rise governs segmentation. *Nature* **446**, 409-414.

Umino, S. Miyashita, S. Hotta, F. & Adachi, Y. (2003) Along-strike variation of the sheeted dike complex in the Oman ophiolite: Insights into subaxial ridge segment structure and the magma plumbing system. *Geochemistry Geophysics Geosystem* **4**, 8618, doi: 100.1029/2001GC000233.

Vernières, J., Godard, M. & Bodinier, J.-L. (1997) A plate model for the simulation of trace element fractionation during partial melting and magma transport in the Earth's upper mantle. *Journal of Geophysical Research* **102**, 24,771-24,784.

Walter, M. J. (1998) Melting of garnet peridotite and the origin of komatiite and depleted lithosphere. *Journal of Petrology* **39**, 29-60.

Workman, R. K. & Hart, S. R. (2005) Major and trace element composition of the depleted MORB mantle (DMM). *Earth and Planetary Science Letters* **231**, 53-72.

11. FIGURES

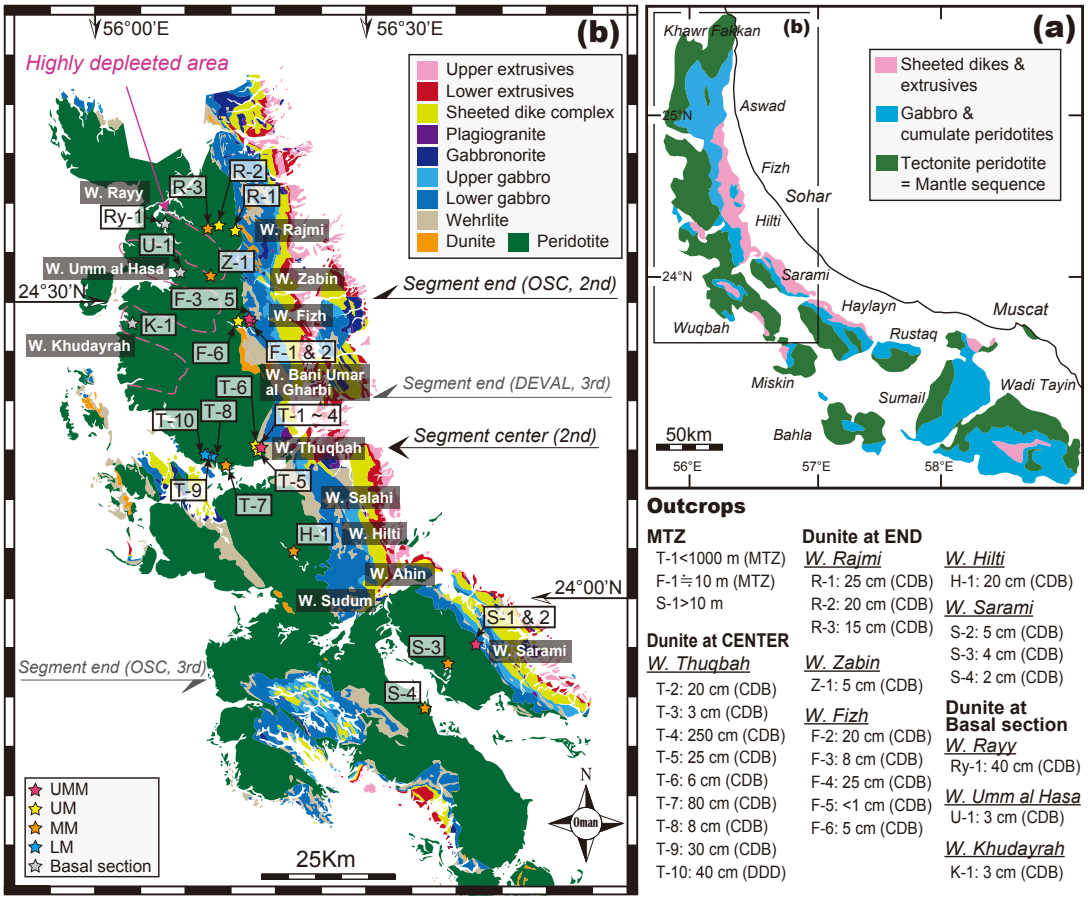

Figure 1

Geological maps. (a) Simplified geological map of the Oman ophiolite modified from Lippard et al. (1986). (b) Distribution of rocks in the northern Oman ophiolite with distribution of the outcrops that were examined in this study; map modified from the 1:250,000 geological maps of Buraymi and Ibri (Ministry of Petroleum and Minerals, 1992a, b). Paleoridge segment structures are from Girardeau et al. (2002), Adachi & Miyashita (2003), Miyashita et al. (2003) and Umino et al. (2003). Area of highly depleted peridotites is enclosed by dashed line (Suetake & Takazawa, 2012). Abbreviations: Center = segment center, End = segment end, MTZ = Moho transition zone, UMM = uppermost mantle section, UM = upper mantle section, MM = middle mantle section, LM = lower mantle section, CDB = concordant dunite band, and DDD = discordant dunite dike.

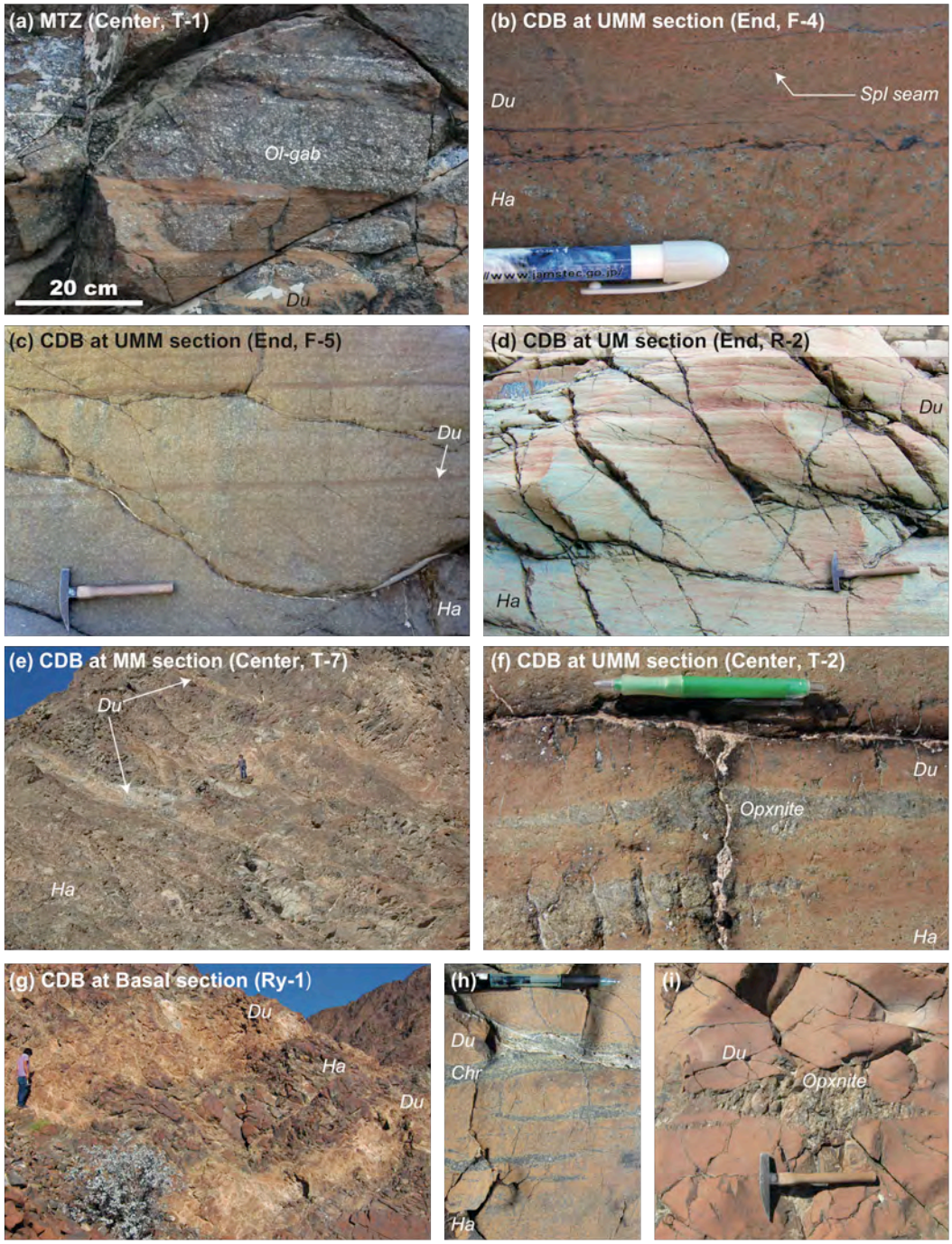

Figure 2

Photographs of outcrops.

(a) Typical appearance of the MTZ in outcrop T-1 along Wadi Thuqbah (segment center). Olivine gabbro (ol-gab) layers in the MTZ are concordant with the base of the layered gabbro section. Brownish parts are composed of dunite (Du) to wehrlite. (b) Sharp and flat boundary between dunite (Du) and harzburgite (Hz) in outcrop F-4 along Wadi Fizh (uppermost mantle section). A spinel seam in the dunite band is concordant with the dunite/harzburgite boundary. (c and d) Concentration of concordant dunite bands in outcrop F-5 in Wadi Fizh (uppermost mantle section) and in outcrop R-2 in Wadi Rajmi (upper mantle section), respectively. (e) Thick concordant dunite bands in outcrop T-7 in Wadi Thuqbah (middle mantle section) (f) The concordant dunite band in outcrop T-2 in Wadi Thuqbah (uppermost mantle section) with association of orthopyroxenites (opxnite) at its center and the boundary with the harzburgite. Note that the lens-shaped orthopyroxenite is elongated and parallel with the boundary. (g) The concordant dunite bands in outcrop Ry-1 in Wadi Rayy (basal section). (h and i) The elongated chromitite (chr) and the pocket of orthopyroxenite (opxnite) in the concordant dunite bands in outcrop Ry-1, respectively. The pen shown in (b) is about 6cm long, and that shown in (f) is about 14 cm long. The hammer in (c), (d) and (i), which is aligned with the harzburgite foliations on the outcrop surface, is approximately 35 cm in length. The man in (e) and (g) is about 180 cm in height.

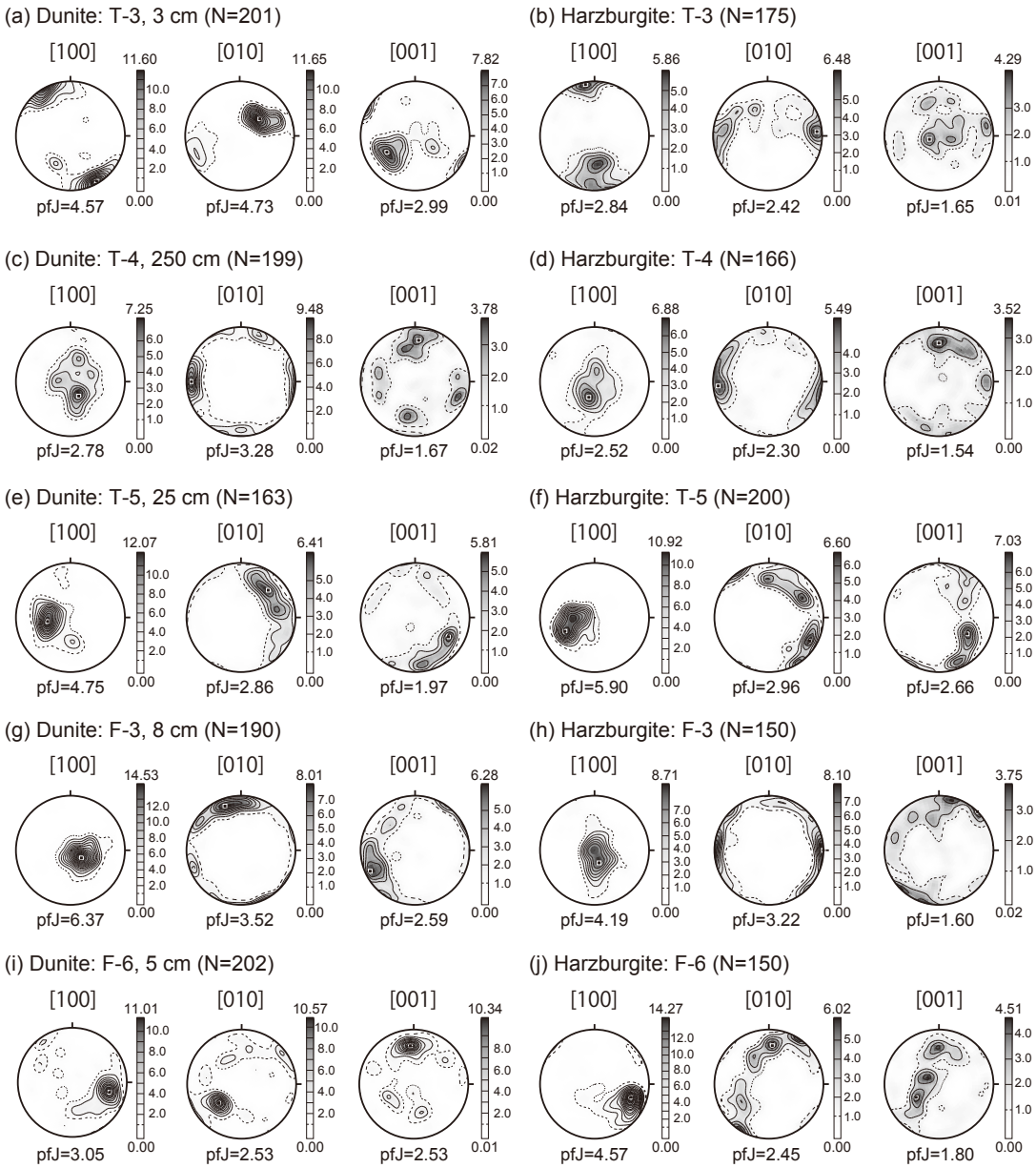

Figure 3

Petrofabric characteristics. Pole figures of the crystal preferred orientation (CPO) of olivines from the solitary dunite bands (a, c, e, g and i) and their ambient harzburgites (b, d, f, h and i), of which pairs are placed side by side.

To obtain representative CPO patterns, total analytical points (N) were more than 150 in number for each lithology. The position of maximum density of CPO is shown with black squares in each pole figures. Unity of random distribution for CPO is defined by pfJ index (maximum value is 60 for a single crystal of olivine, cf. Michibayashi & Mainprice, 2006). Equal area projection, lower hemisphere stereoplots, and contours at 1 multiples of uniform distribution.

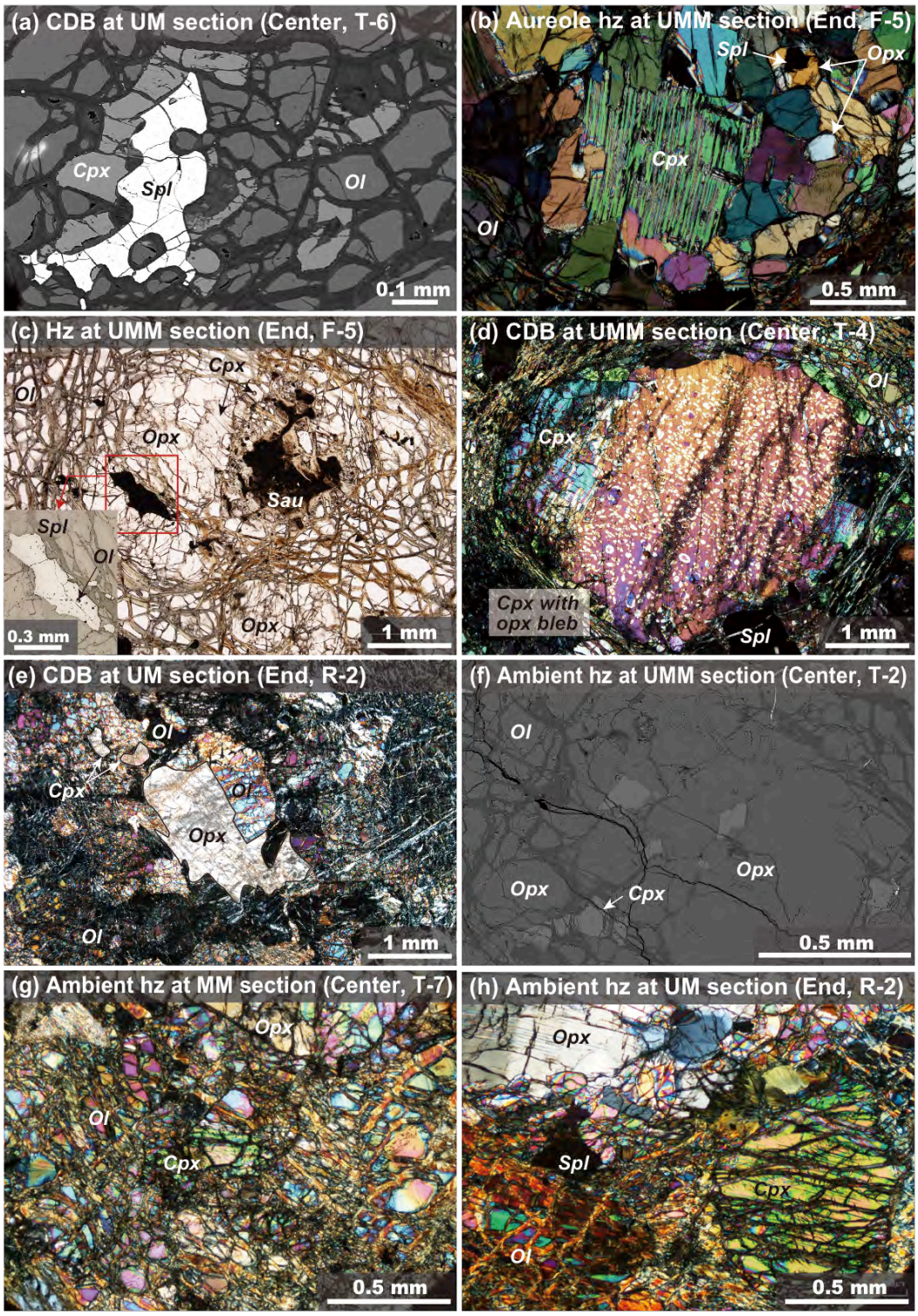

Figure 4

Petrographic characteristics of dunites and harzburgites.

(a) Interstitial clinopyroxene associated to anhedral spinel in the concordant dunite band of outcrop T-6 (Wadi Thuqbah). (b) Orthopyroxene porphyroclast irregularly replaced by clinopyroxene in the aureole harzburgite at outcrop F-5 (Wadi Fizh). (c) Composite grain of orthopyroxene, clinopyroxene, spinel and saussurite in a harzburgite, which is about 20 cm above the concordant dunite band at outcrop F-5 (Wadi Fizh). The spinel contains olivine inclusions (inset). (d) Large clinopyroxene grain (about 3 mm in diameter) with orthopyroxene blebs in the thick (250 cm) concordant dunite band at outcrop T-4 (Wadi Thuqbah). (e) Irregular-shaped orthopyroxene grain in the concordant dunite band at outcrop R-2 (Wadi Rajmi). (f) Typical ambient harzburgite from the uppermost mantle section (outcrop T-2). The clinopyroxenes are almost rare, tiny and related to the orthopyroxene porphyroclast in the harzburgite. (g) Typical ambient harzburgite from the lower to middle mantle section at the segment center (outcrop T-7). Note that the clinopyroxene is tiny (less than 0.5 mm in diameter) and interstitial to olivine. (h) ambient harzburgite from the upper mantle section at the segment end (outcrop R-2). Clinopyroxene is large (more than 0.5 mm in diameter); no such harzburgites are observed at the segment center through all stratigraphic level observed. Abbreviations: ol = olivine, spl = spinel, opx = orthopyroxene, cpx = clinopyroxene, sau = saussurite, and hz = harzburgite. Composite images (a and f) and photomicrographs (b-e and g-h). Panel (c) is by plane-polarized light, and the others by crossed-polarized light.

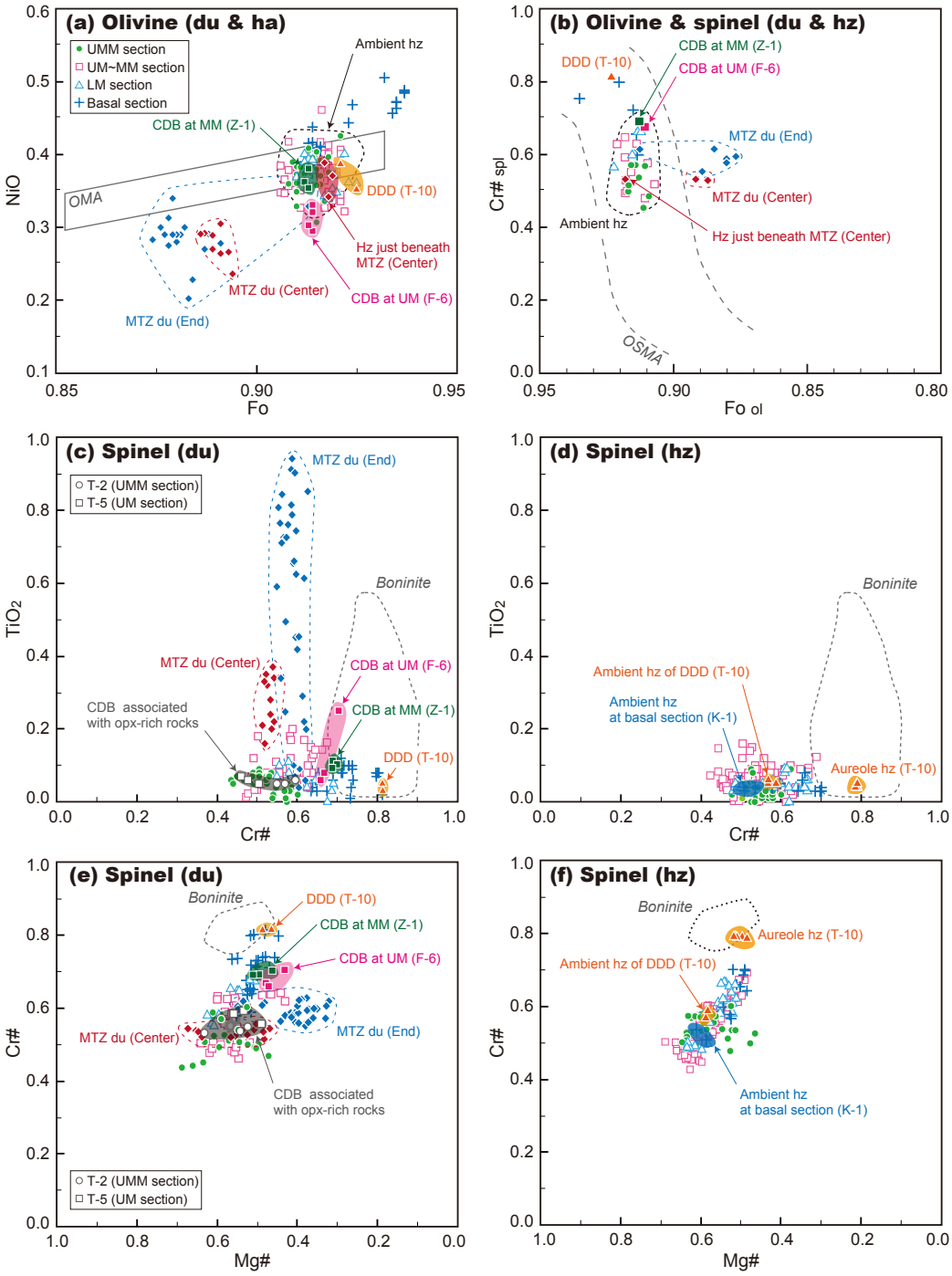

Figure 5

Mineral chemical characteristics of dunites (du) and their ambient harzburgites (hz).

(a) Variations of Fo and NiO in olivine. Olivine mantle array (OMA) is the field of residual mantle peridotite (Takahashi, 1986). (b) Relationships between Fo of olivine and Cr# of spinel. Olivine-spinel mantle array (OSMA) is the trend of residual spinel peridotite defined by Arai (1994). Plots of (a) and (b) are mean values; standard deviations are smaller than individual symbols. (c-f) Variations of Cr#,TiO_2 and Mg# in spinel. Note that (d) and (f) contain data of both "ambient harzburgites" and "aureole harzburgites" of the dunite bands. The boninite fields are modified from Tamura and Arai (2006) (c and d), and from Ishikawa et al. (2002) (e and f). (g-j) Variations of Mg#, Al_2O_3 and Cr_2O_3 in clinopyroxene and orthopyroxene. The ranges of chemical composition of orthopyroxene are shown in red for the lower to uppermost mantle section, and in blue for the basal section. The arrowed thick lines show a systematic change in chemistry from the lower mantle section to the uppermost mantle section in this study. Abbreviations are the same as in Figure 1.

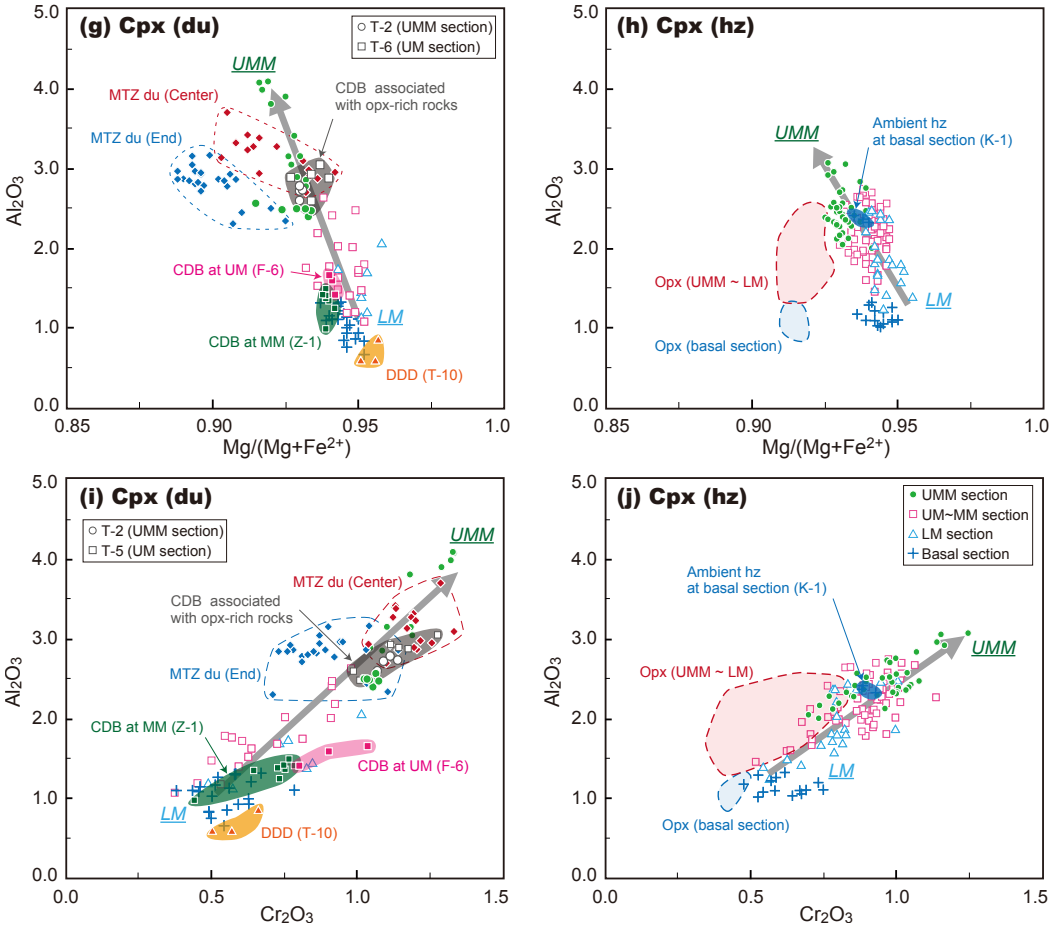

Figure 5 (Continued)

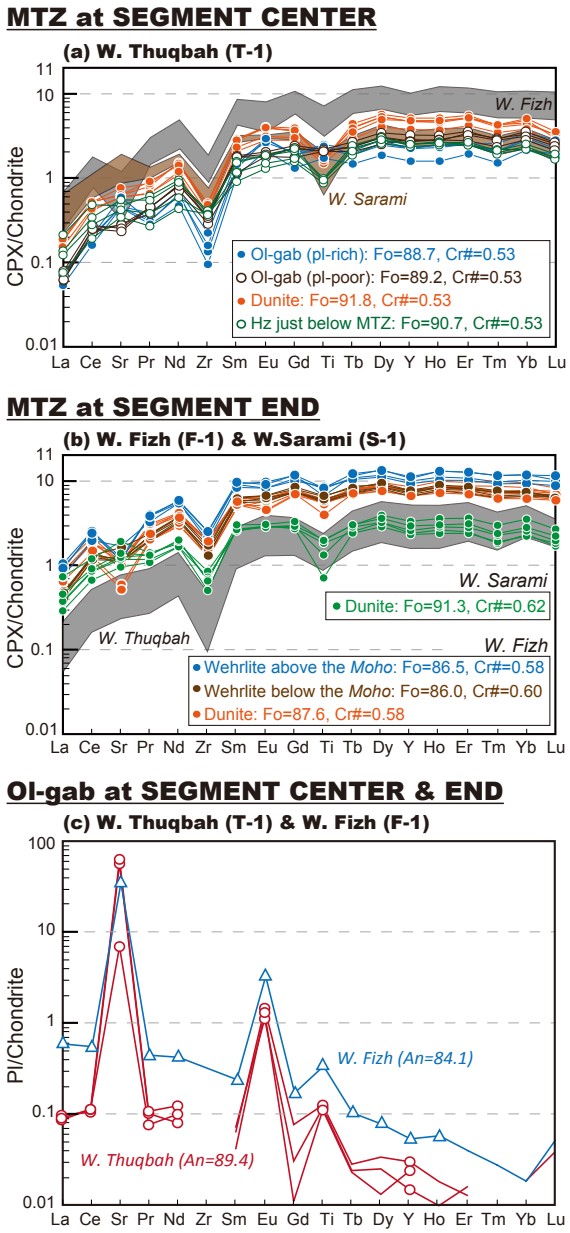

Figure 6

Trace-element compositions. (a and b) Chondrite-normalized trace-element patterns of clinopyroxene in olivine gabbro (ol-gab), wehrlite, dunite and harzburgite (hz) from Wadi Thuqbah, Wadi Fizh and Wadi Sarami. (c) Chondrite-normalized trace-element patterns of plagioclase in the olivine gabbro (ol-gab) from Wadi Thuqbah and Wadi Fizh. Mean values of Fo, Cr# and An (when plagioclase is present) are shown in each lithology. Lithology and mineral chemistry are shown in rectangle boxes. Chondrite values are from Sun and McDonough (1989). Data below the detection limits are not shown.

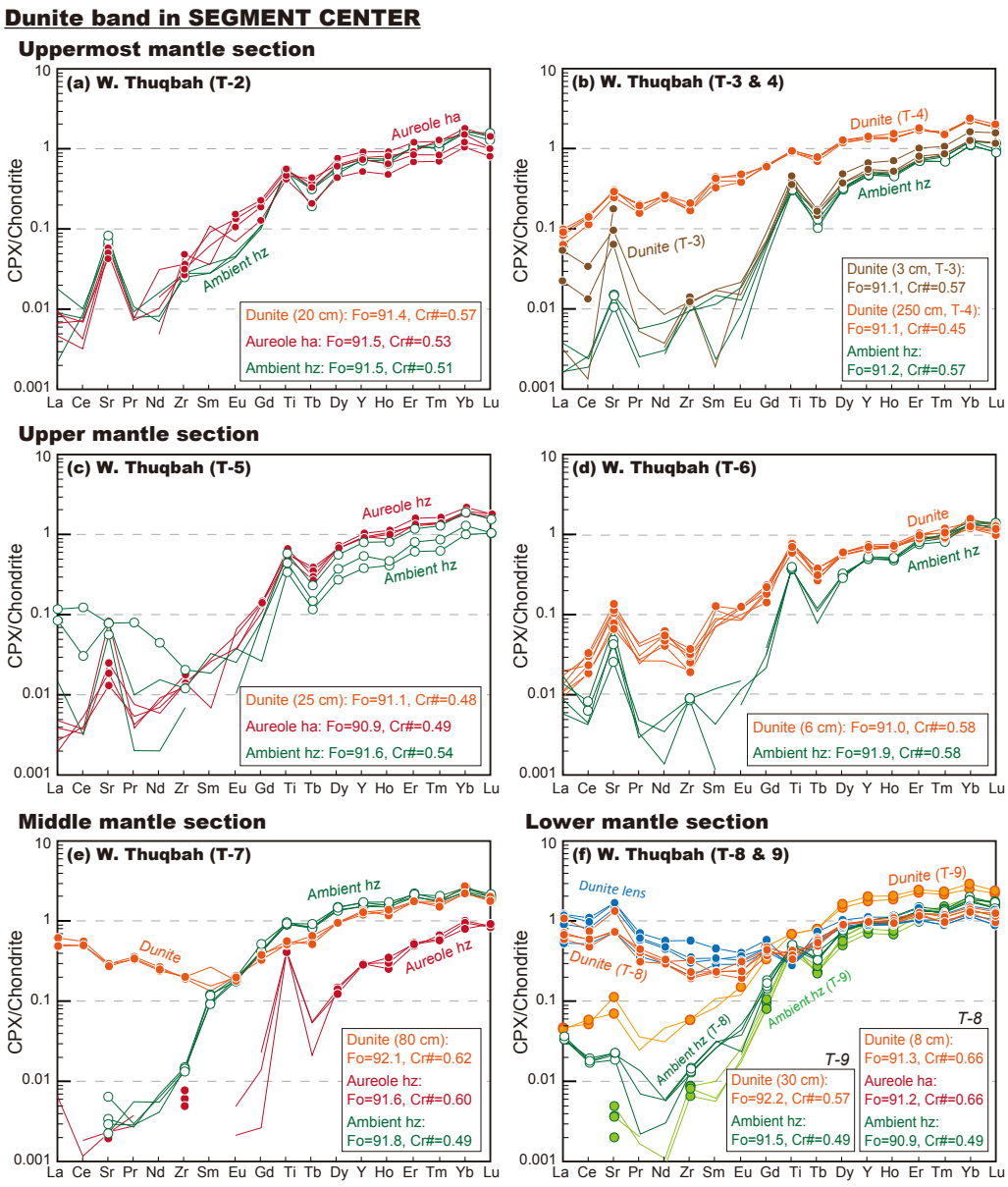

Figure 7

Chondrite-normalized trace-element patterns of clinopyroxene in the dunite and harzburgite (hz) at the segment center. For dunites that contain no clinopyroxene, data are acquired from the aureole harzburgite within a few centimeters from the dunite band. The aureole harzburgite from outcrop T-7 is, however, about 50 cm away from the boundary with dunite (e). Lithology and mineral chemistry are shown in rectangle boxes. Fo and Cr# are mean values. Chondrite values are from Sun and McDonough (1989). Data below the detection limits are not shown.

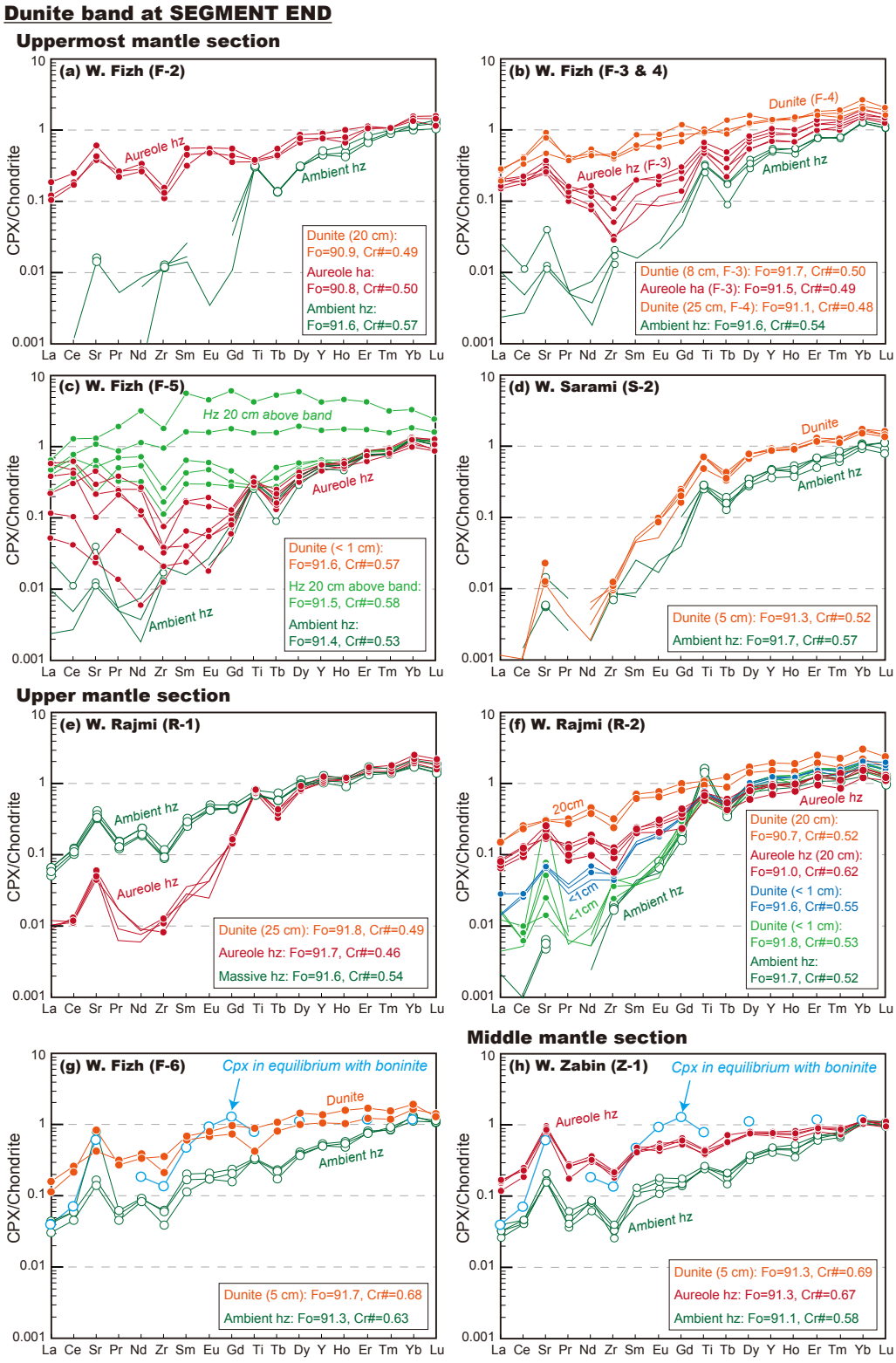

Figure 8

Chondrite-normalized trace-element patterns of clinopyroxene in the dunite and harzburgite (hz) at the segment end.

The clinopyroxene from the harzburgite about 20 cm away from the dunite/harzburgite boundary (Hz 20 cm above band) at outcrop F-5 (c) is exceptionally enriched in trace elements . The trace-element pattern of clinopyroxene in equilibrium with boninite from the Oman ophiolite is shown in (g) and (h) (cf. Ishikawa et al., 2002). Lithology and mineral chemistry are shown in rectangle boxes. Fo and Cr# are mean values. Chondrite values are from Sun and McDonough (1989). Data below the detection limits are not shown.

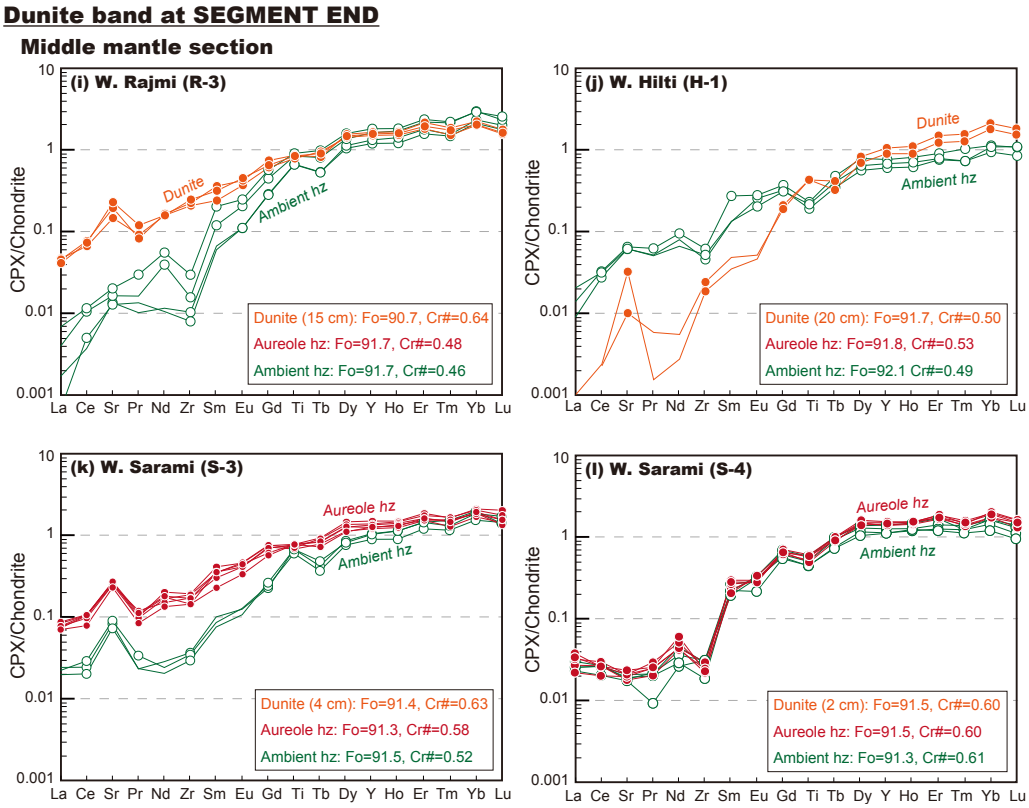

Figure 8 (Continued)

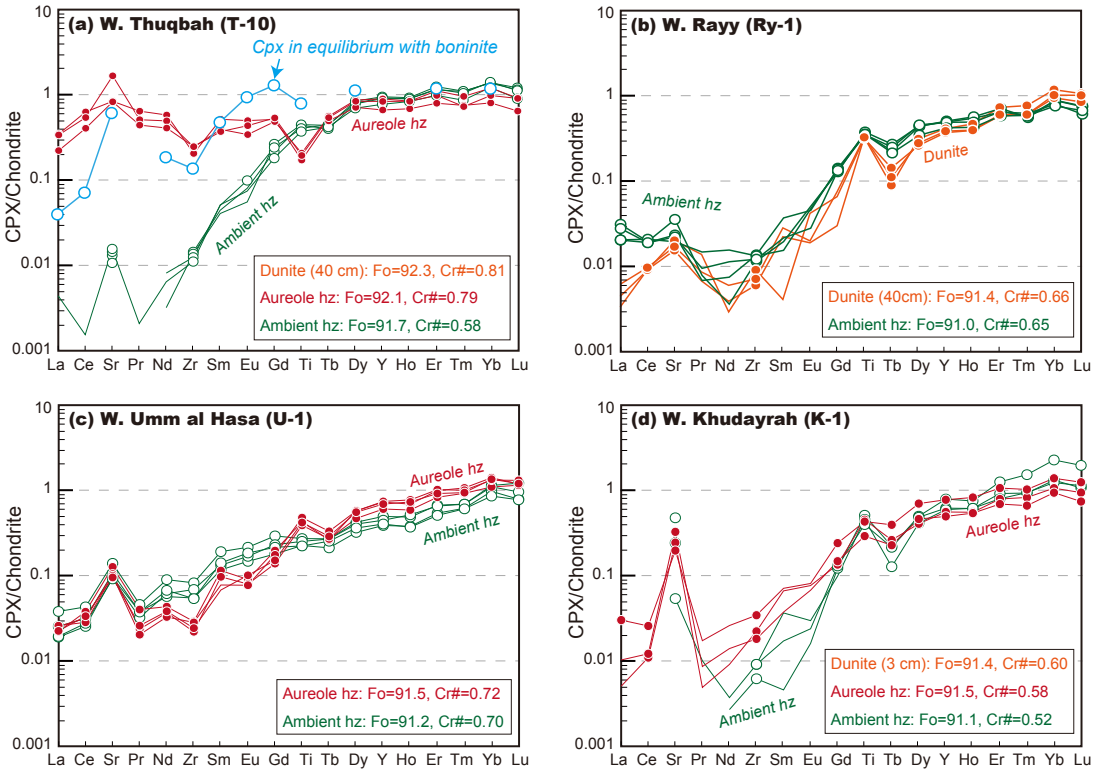

Figure 9

Trace-element compositions of clinopyroxene. (a) Chondrite-normalized trace-element patterns of clinopyroxene in the aureole harzburgite and ambient harzburgite of the discordant dunite dike. The trace-element pattern of clinopyroxene in equilibrium with the boninite from the Oman ophiolite is from Ishikawa et al. (2002). (b-d) Chondrite-normalized trace-element patterns of clinopyroxene in the concordant dunite bands and their ambient harzburgites from the basal section of the Oman ophiolite. Lithology and mineral chemistry are shown in rectangle boxes. Fo and Cr# are mean values. Chondrite values are from Sun and McDonough (1989). Data below the detection limits are not shown.

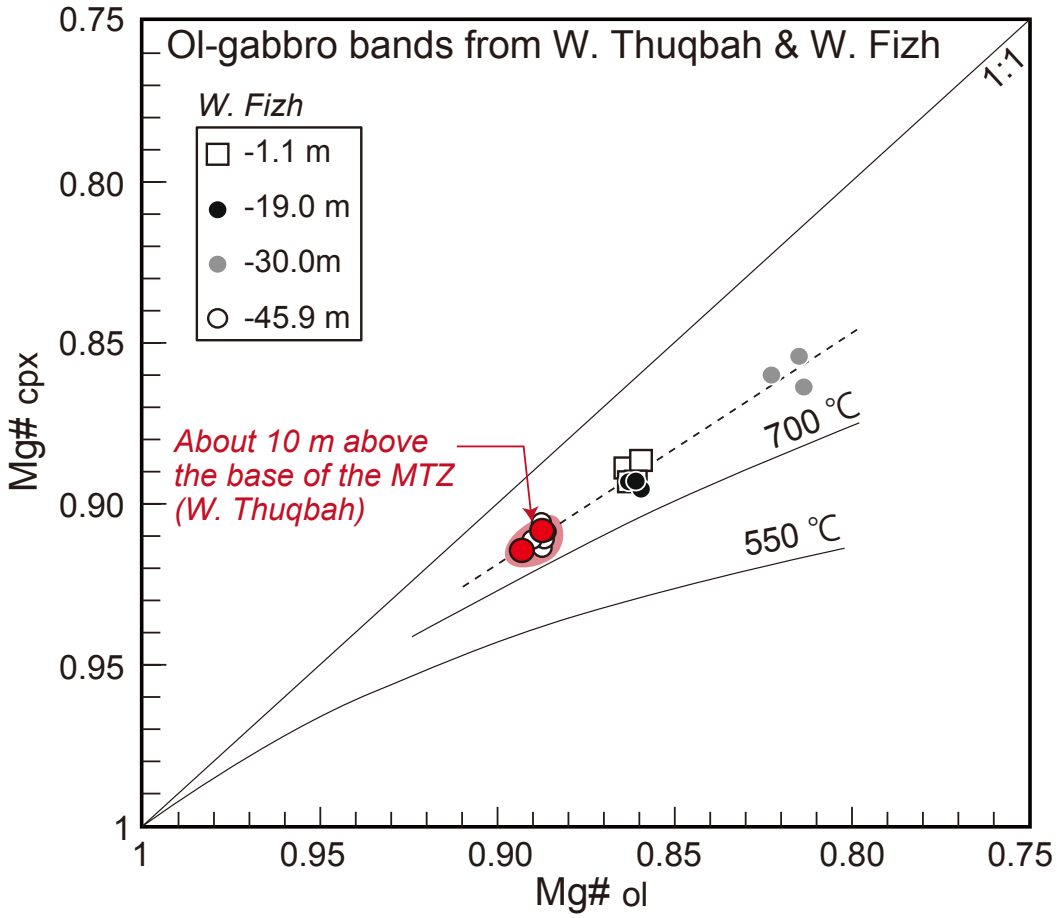

Figure 10

Mg-Fe partitioning between olivine (ol) and clinopyroxene (cpx) in olivine gabbro (ol-gabbro) bands around the MTZ; two bands are located about 10 m above the base of the MTZ in Wadi Thuqbah, and four bands are located about 1 m, 19 m, 30 m and 46 m below the base of the layered gabbro section in Wadi Fizh (cf. Akizawa et al., 2012). Isotherms are from Obata et al. (1974). Olivine and clinopyroxene have attained equilibrium in terms of Mg-Fe partition at high temperature [1,160-1,200 °C, Loucks (1996)].

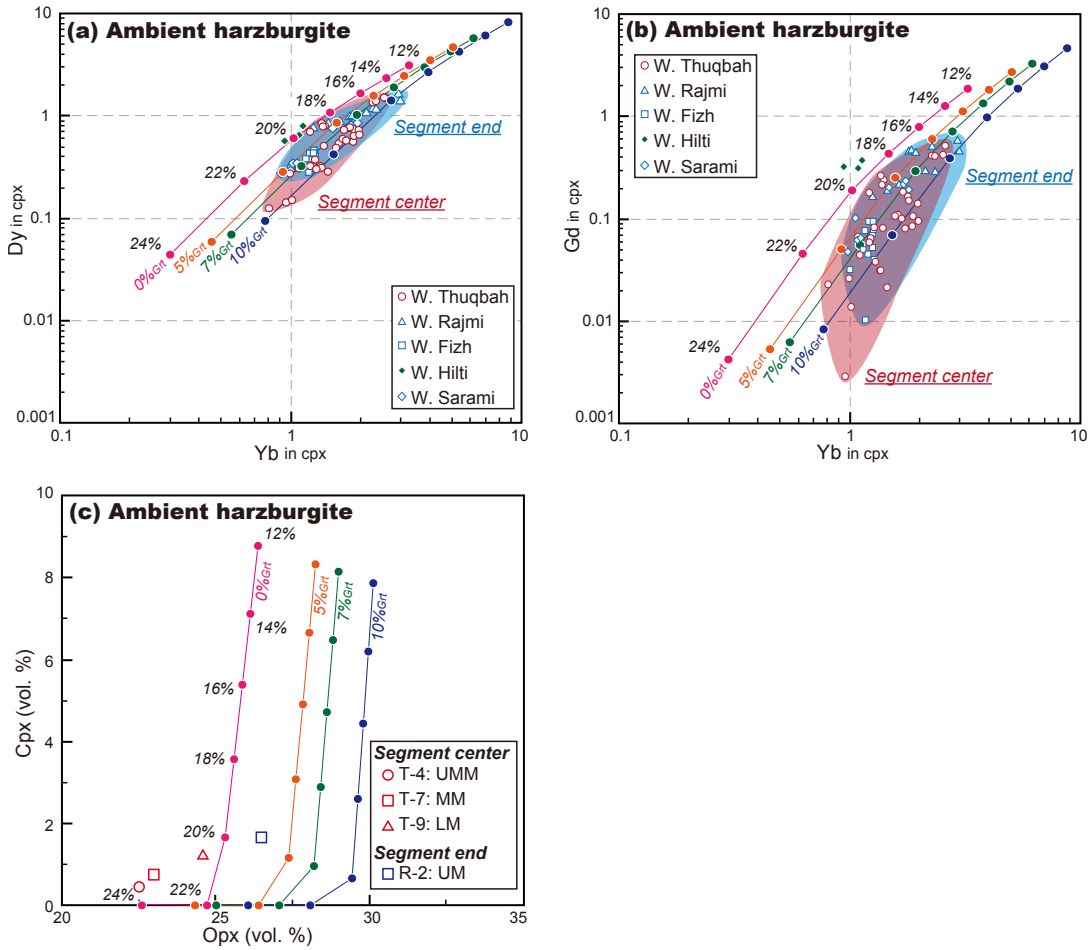

Figure 11

Chemical and petrographic relationships between the ambient harzburgite of the dunite band, and the residual harzburgite calculated by the numerical modeling. (a and b) Relationships between chondrite-normalized Yb, Dy and Gd of clinopyroxene in the ambient harzburgites from the segment center and segment end. Calculated compositions of residual clinopyroxene in the numerical modeling, fractional melting of DMM, are also shown; (1) melting only in the spinel stability field (0 $\%_{Grt}$), (2) 5 % melting in the garnet stability field followed by melting in the spinel stability field (5 $\%_{Grt}$), (3) 7 % melting in the garnet stability field followed by melting in the spinel stability field (7 $\%_{Grt}$), and (4) 10 % melting in the garnet stability field followed by melting in the spinel stability field (10 $\%_{Grt}$). (c) Modal variations of orthopyroxene and clinopyroxene (vol. %) in the ambient harzburgite and the residual harzburgite calculated by the numerical modeling. Chondrite values are from Sun and McDonough (1989).

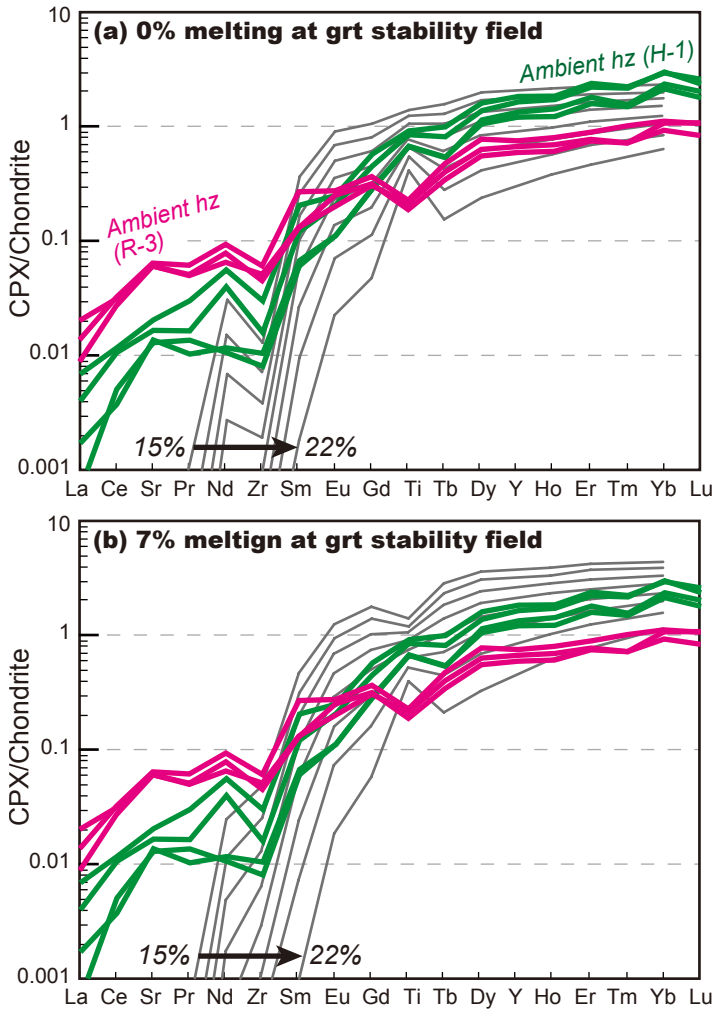

Figure 12

Chondrite-normalized trace-element patterns of clinopyroxene obtained by numerical modeling. (a) Fractional melting of DMM only in the spinel stability field. (b) 7 % fractional melting of DMM in the garnet stability field followed by melting in the spinel stability field. Trace-element patterns of clinopyroxene in ambient harzburgites are from outcrops R-3 and H-1 (segment end). Chondrite values are from Sun and McDonough (1989).

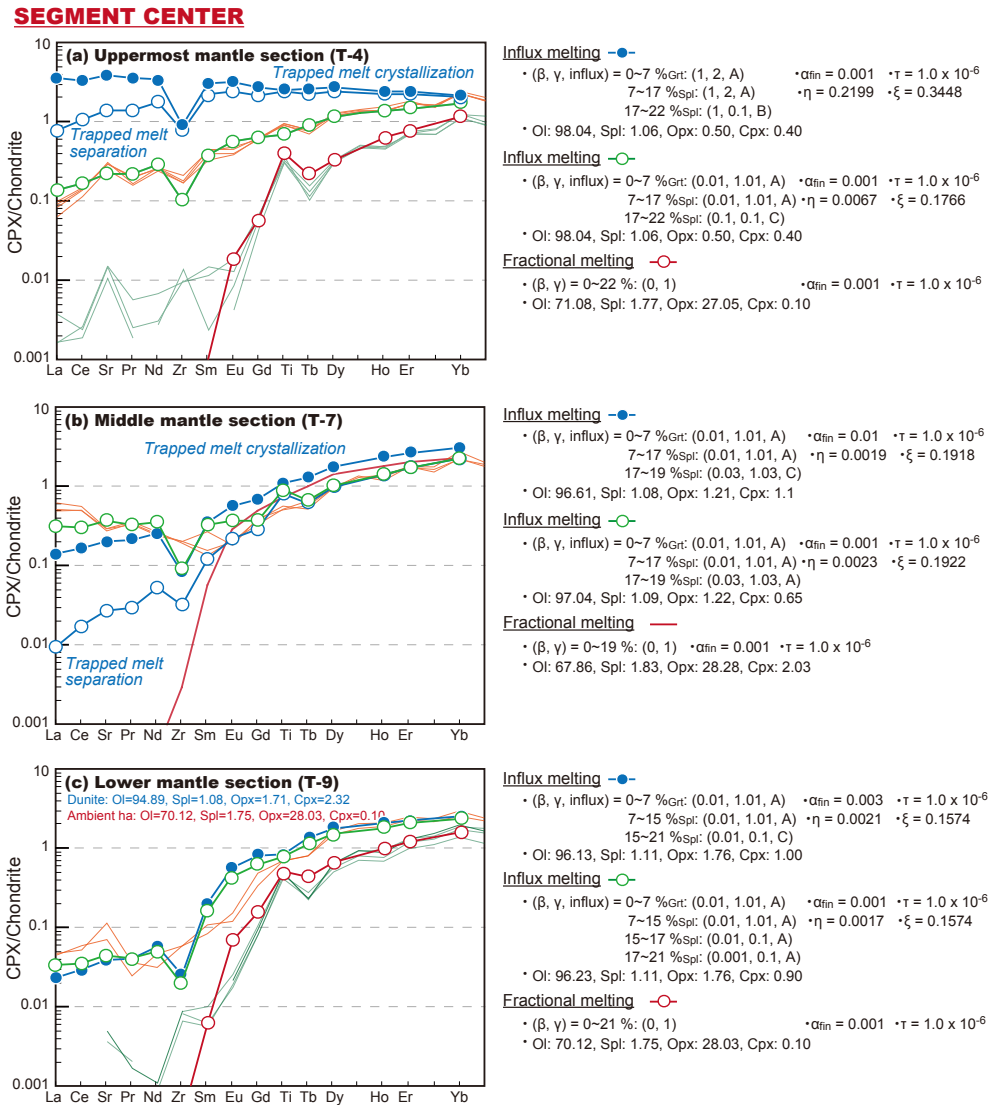

Figure 13

Trace-element patterns of clinopyroxene obtained by the numerical modeling in dunite channel and residual harzburgite. Parameters used are shown on the right-hand side. (a-c) Segment center. (d-f) Segment end. See text for details.

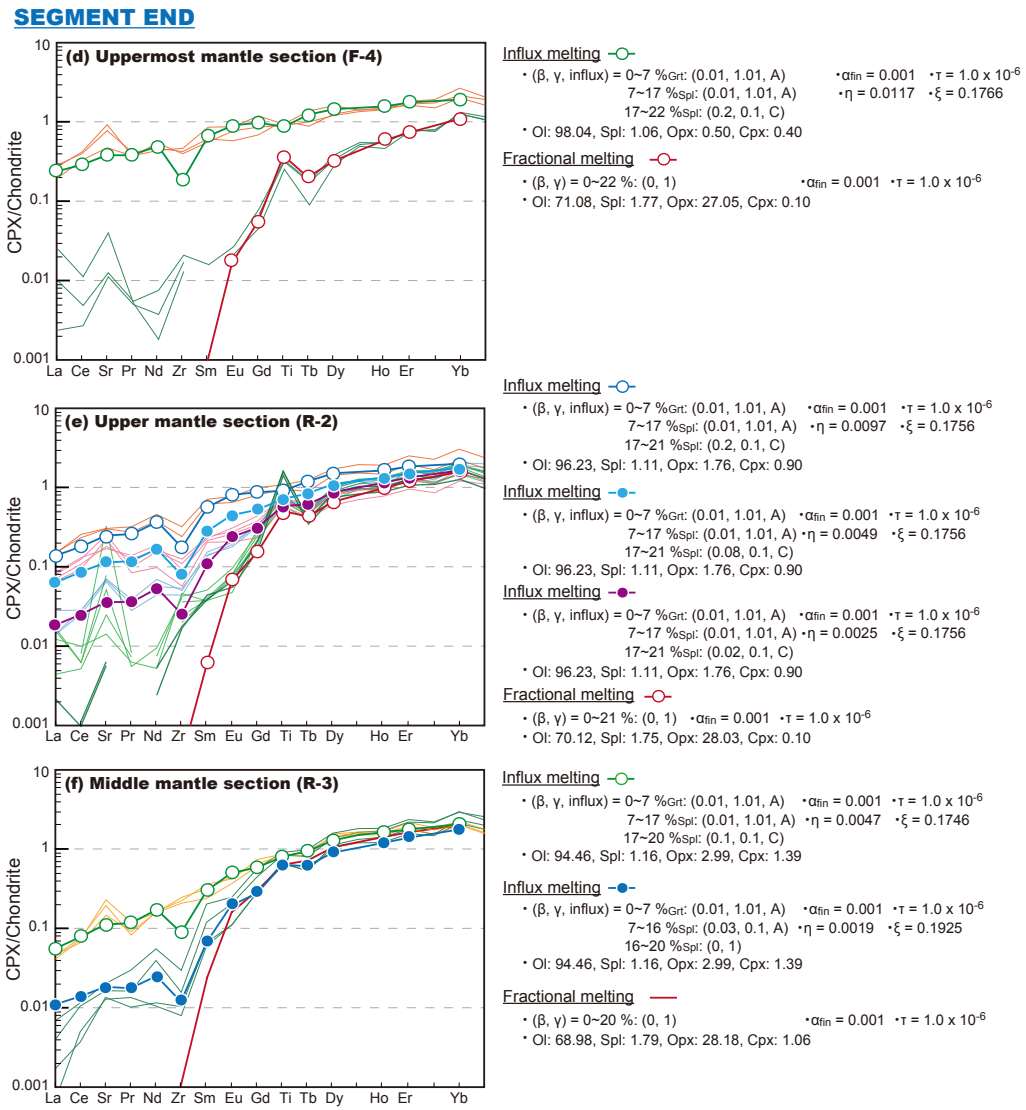

Figure 13 (Continued)

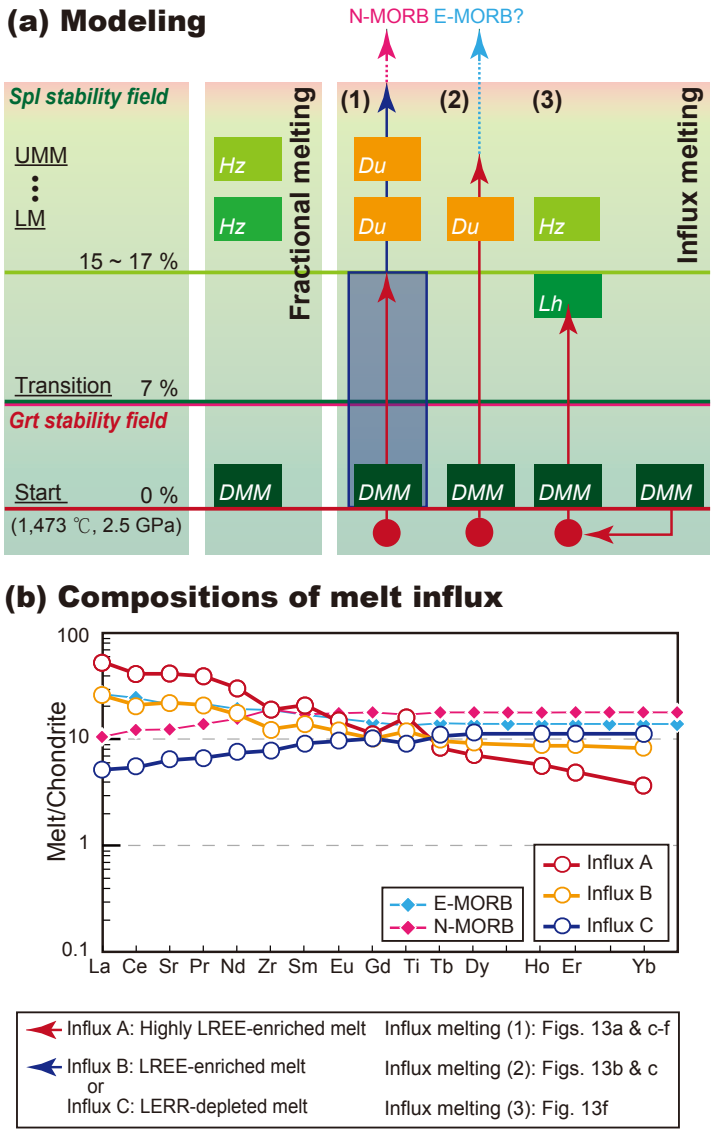

Figure 14

Summary of the numerical modeling. (a) Modes of melting to duplicate the "ambient harzburgite" by fractional melting of DMM and the "dunite channel" by influx melting of DMM. Influx melting (1) shows the mode of Figure 13a and c-f, influx melting (2) shows the mode of Figure 13b and c, and influx melting (3) shows the mode of Figure 13f. (b) Chondrite-normalized trace element compositions of melt used in the influx melting of the numerical modeling. Note that influx C is similar to N-MORB in trace-element composition. N-MORB and E-MORB compositions and chondrite values are from Sun & McDonough (1989). Abbreviation: Lh = lherzolite, Hz = harzburgite, Du = dunite, Grt = garnet, Spl = spinel, UMM = uppermost mantle section, and LM = lower mantle section.

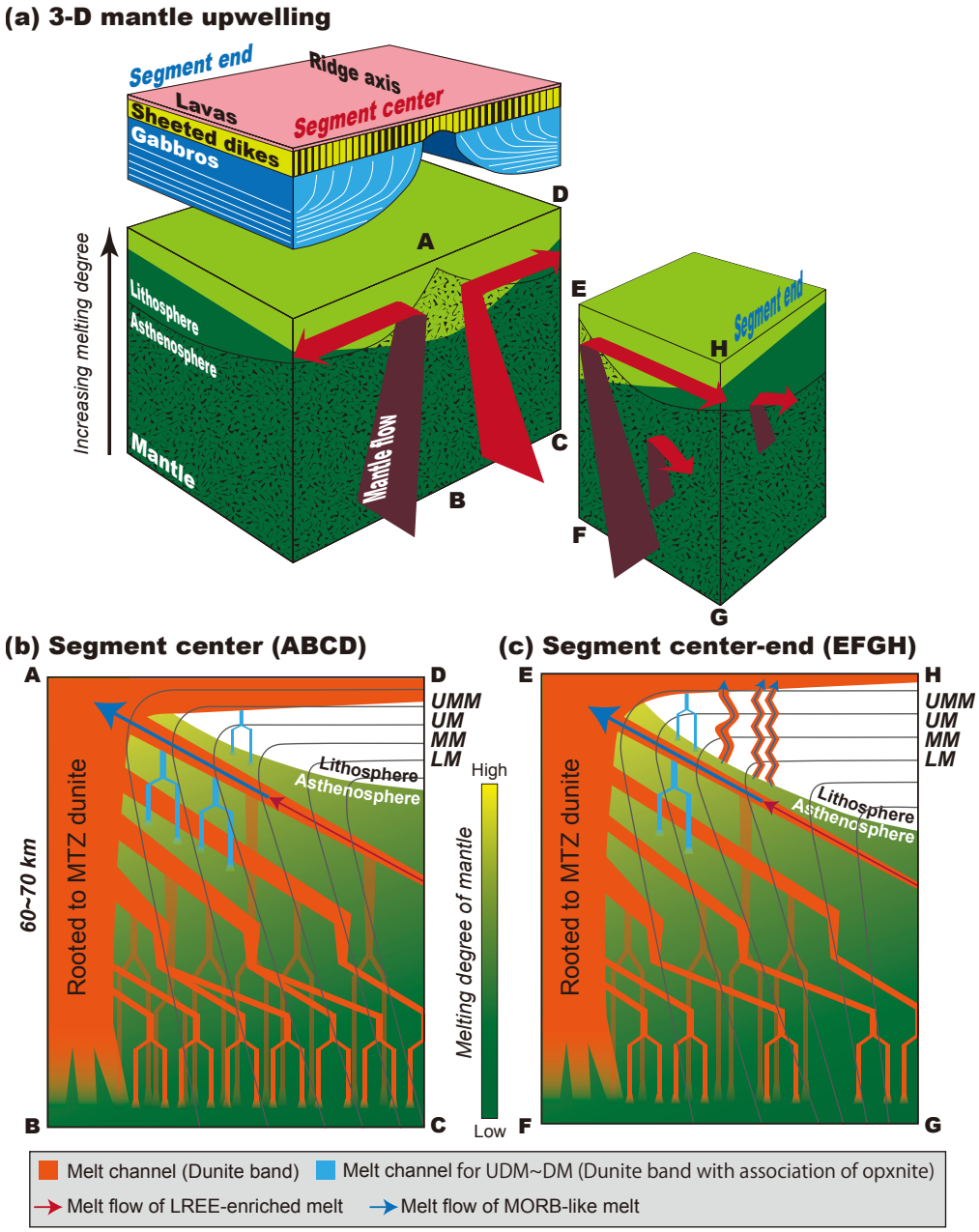

Figure 15

Schematic illustration of suboceanic lithosphere and asthenosphere. (a) A sketch of three-dimensional mantle upwelling beneath a fast-spreading center (modified from Nicolas et al., 2000). (b) Melt-channel distribution in the mantle section across axis at the segment center. (c) Melt-channel distribution in the mantle section along axis from the segment center to the segment end. The gray lines show mantle flow. Abbreviations: UMM = uppermost mantle section, UM = upper mantle section, MM = middle mantle section, LM = lower mantle section, UDM = ultra depleted melt, and DM = depleted melt.

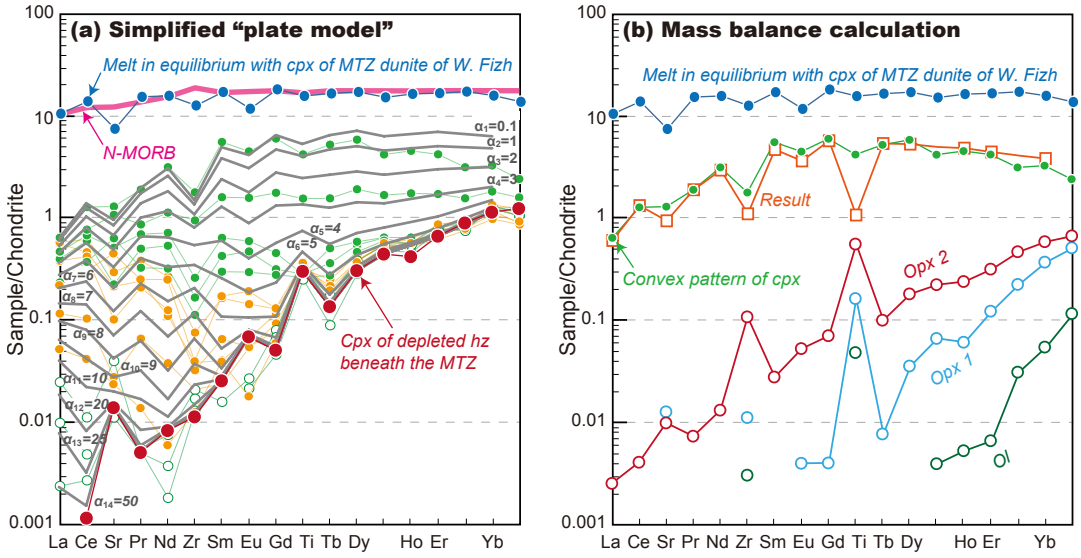

Figure 16

Duplication of trace-element patterns of clinopyroxene by modeling and calculation that explain fracture-related melt migration. (a) Results of a simplified numerical modeling, modified from the "plate model" of Vernières et al. (1997) (cf. Tamura et al., 2008). The modeling duplicates spoon-shaped patterns and moderately depleted patterns declining from HREE to LREE, but not the convex-upward pattern such as that obtained in the harzburgite 20 cm above the concordant dunite band of outcrop F-5 (Fig. 8c). (b) Result of a mass balance calculation for a convex-upward pattern, which is explained by an interaction between N-MORB-like melt and harzburgite with a low melt/rock ratio. Trace-element compositions of intruding melt, clinopyroxene, orthopyroxenes (opx 1 and opx 2) and olivine for calculations are shown in Table 10. See text for details. N-MORB composition and chondrite values are from Sun & McDonough (1989).

12. Table

Wadi	Outcrop	Description	Ol	Opx	Cpx	Spl	Total
Thuqbah	T-4: UMM	Ambient	76.3	22.5	0.4	0.8	100
Thuqbah	T-7: MM	Aureole	90.7	8.4	0.4	0.5	100
Thuqbah	T-7: MM	Ambient	75.2	23.0	0.8	1.0	100
Thuqbah	T-9: LM	Ambient	72.5	24.6	1.2	1.7	100
Rajmi	R-2: UM	Ambient	70.8	26.5	1.7	1.0	100
Rajmi	R-3: MM	Ambient	84.4	12.1	1.0	2.5	100
Fizh	F-4: UMM	Ambient	83.1	16.0	0.3	0.6	100

Table 1. Modal amounts of minerals in harzburgites. Abbreviations: UMM = uppermost mantle section, UM = upper mantle section, MM = middle mantle section, LM = lower mantle section, ol = olivine, opx = orthopyroxene, cpx = clinopyroxene and spl = spinel. The aureole harzburgite at outcrop T-7 is about 50 cm away from the boundary with dunite, and is called ‘harzburgite’ for our convenience even though dunitic in modal composition.

Wadi	Outcrop	Rock type	SiO_2	TiO_2	Al_2O_3	Cr_2O_3	FeO*	MnO	MgO	CaO	Na_2O	K_2O	NiO	Total	Fo
Thuqbah	T-1: MTZ	Ol-gab (Pl-rich)	40.47	0.00	-	-	10.41	0.14	48.94	0.06	0.02	-	0.27	100.31	89.3
Thuqbah	T-1: MTZ	Ol-gab (Pl-poor)	40.67	-	-	-	10.86	0.14	48.79	0.03	0.01	0.01	0.29	100.79	88.9
Thuqbah	T-1: MTZ	Dunite	41.07	-	-	-	8.06	0.13	50.49	0.09	-	-	0.34	100.18	91.8
Thuqbah	T-1: MTZ	Hz beneath MTZ	40.76	-	-	-	8.61	0.12	50.06	0.03	0.02	0.00	0.35	99.94	91.2
Thuqbah	T-2: UMM	CDB (20 cm)	40.96	-	-	-	8.49	0.14	51.21	0.11	0.00	-	0.39	101.30	91.5
Thuqbah	T-2: UMM	Aureole hz	41.14	-	0.01	-	8.58	0.14	51.41	0.02	0.00	0.01	0.40	101.70	91.4
Thuqbah	T-2: UMM	Ambient hz	41.39	-	-	-	8.52	0.09	51.19	0.04	0.01	0.00	0.40	101.64	91.5
Thuqbah	T-3: UMM	CDB (3 cm)	41.30	-	-	0.02	8.81	0.12	49.71	0.08	-	-	0.38	100.41	91.0
Thuqbah	T-3: UMM	Aureole hz	41.33	-	-	-	8.80	0.12	50.18	0.01	-	-	0.42	100.86	91.0
Thuqbah	T-3: UMM	Ambient hz	41.30	-	-	0.02	8.81	0.12	49.71	0.08	-	-	0.38	100.41	91.0
Thuqbah	T-4: UMM	CDB (250 cm)	41.36	-	-	-	8.75	0.09	50.95	0.02	0.01	0.01	0.37	101.56	91.2
Thuqbah	T-5: UM	CDB (25 cm)	41.64	-	-	-	8.80	0.16	50.69	0.20	-	0.00	0.36	101.85	91.1
Thuqbah	T-5: UM	Aureole hz	41.66	-	-	-	8.97	0.17	50.58	0.03	-	0.00	0.37	101.77	91.0
Thuqbah	T-5: UM	Ambient hz	41.41	-	-	0.02	8.31	0.13	50.65	0.01	-	0.00	0.39	100.93	91.6
Thuqbah	T-6: UM	CDB (6 cm)	41.23	-	-	-	8.93	0.12	50.50	0.07	0.00	-	0.38	101.23	91.0
Thuqbah	T-6: UM	Aureole hz	41.23	0.00	-	-	8.70	0.10	50.96	0.03	-	0.01	0.39	101.42	91.3
Thuqbah	T-6: UM	Ambient hz	41.53	0.02	-	-	8.19	0.12	51.91	0.01	-	-	0.40	102.17	91.9
Thuqbah	T-7: MM	CDB (80 cm)	41.37	-	-	0.00	7.83	0.15	51.43	0.03	-	-	0.34	101.15	92.1
Thuqbah	T-7: MM	Aureole hz	41.35	-	-	-	8.29	0.12	51.28	0.02	-	0.02	0.39	101.46	91.7
Thuqbah	T-7: MM	Ambient hz	41.36	-	-	0.01	8.16	0.10	51.17	0.02	0.00	-	0.39	101.21	91.8
Thuqbah	T-8: LM	CDB (8 cm)	41.47	-	-	-	8.55	0.13	49.98	0.09	-	-	0.40	100.63	91.2
Thuqbah	T-8: LM	Dunite lens	41.77	0.02	0.00	-	8.62	0.14	50.36	0.03	-	-	0.39	101.34	91.2
Thuqbah	T-8: LM	Aureole hz	41.81	0.01	-	-	8.62	0.14	50.20	0.01	0.02	0.01	0.38	101.19	91.2
Thuqbah	T-8: LM	Ambient hz	41.58	0.00	-	-	8.83	0.14	50.24	0.03	-	0.00	0.40	101.22	91.0
Thuqbah	T-9: LM	CDB (30 cm)	41.45	-	0.01	-	7.70	0.13	52.07	0.03	0.00	-	0.36	101.74	92.3
Thuqbah	T-9: LM	Aureole hz	41.88	-	-	-	7.96	0.11	51.77	0.02	-	0.00	0.39	102.12	92.1
Thuqbah	T-9: LM	Ambient hz	41.53	-	-	-	8.27	0.10	51.69	-	-	-	0.38	101.97	91.8
Rajmi	R-1: UM	CDB (25 cm)	41.52	-	-	-	7.99	0.10	50.59	0.04	0.01	-	0.34	100.59	91.9
Rajmi	R-1: UM	Aureole hz	41.64	-	0.01	-	8.14	0.07	50.64	0.01	-	0.00	0.37	100.89	91.7
Rajmi	R-1: UM	Ambient hz	41.59	-	-	-	8.29	0.09	50.61	0.01	-	0.00	0.38	100.96	91.6
Rajmi	R-2: UM	CDB (20 cm)	41.35	0.02	-	-	9.01	0.10	50.09	0.01	0.02	-	0.38	100.98	90.8
Rajmi	R-2: UM	Aureole hz	41.60	-	-	-	8.89	0.09	50.59	0.01	0.01	-	0.38	101.58	91.0
Rajmi	R-2: UM	CDB (<1 cm)	41.23	-	-	-	8.70	0.10	51.30	0.02	-	0.00	0.39	101.74	91.3
Rajmi	R-2: UM	CDB (<1 cm)	41.52	0.01	-	-	8.00	0.14	50.84	0.01	0.00	0.00	0.38	100.91	91.9
Rajmi	R-2: UM	Ambient hz	41.19	-	-	-	8.20	0.15	51.74	0.02	0.01	0.00	0.40	101.70	91.8
Rajmi	R-3: MM	CDB (15 cm)	41.59	-	-	-	8.25	0.08	51.69	0.03	0.02	-	0.34	102.00	91.8
Rajmi	R-3: MM	Aureole hz	41.19	-	-	-	8.35	0.14	51.36	0.01	0.01	0.00	0.34	101.39	91.6
Rajmi	R-3: MM	Ambient hz	41.33	0.01	-	-	8.32	0.09	51.51	0.02	-	0.00	0.39	101.66	91.7
Zabin	Z-1: MM	CDB (5 cm)	40.89	-	-	0.00	8.61	0.12	50.84	0.02	-	0.00	0.38	100.87	91.3
Zabin	Z-1: MM	Aureole hz	41.35	-	0.00	-	8.74	0.17	50.61	0.03	0.01	-	0.37	101.28	91.2
Zabib	Z-1: MM	Ambient hz	41.05	-	-	-	8.86	0.13	50.09	0.02	-	0.00	0.40	100.55	91.0
Fizh	F-1: MTZ	Wehrlite (above)	40.16	-	-	-	13.30	0.24	47.65	0.02	-	-	0.23	101.59	86.5
Fizh	F-1: MTZ	Wehrlite (below)	40.14	0.01	-	-	13.46	0.29	46.54	0.04	-	0.01	0.26	100.74	86.0
Fizh	F-1: MTZ	Dunite	39.61	-	-	0.02	11.93	0.18	48.09	0.01	-	-	0.31	100.15	87.8
Fizh	F-2: UMM	CDB (20 cm)	41.16	0.01	-	-	9.00	0.13	50.72	0.02	-	-	0.39	101.43	90.9
Fizh	F-2: UMM	Aureole hz	41.35	-	-	-	8.99	0.09	50.27	0.00	0.01	-	0.41	101.12	90.9
Fizh	F-2: UMM	Ambient hz	41.49	-	-	-	8.97	0.14	51.09	0.03	-	-	0.39	102.11	91.0
Fizh	F-3: UMM	CDB (8 cm)	41.07	0.00	-	-	8.27	0.11	50.93	0.03	-	-	0.39	100.80	91.7
Fizh	F-3: UMM	Aureole hz	40.40	0.01	-	-	8.37	0.13	50.81	0.02	-	-	0.40	100.14	91.5
Fizh	F-3: UMM	Ambient hz	40.83	-	-	0.00	8.54	0.13	50.74	0.02	0.00	-	0.40	100.66	91.4
Fizh	F-4: UMM	CDB (25 cm)	41.05	-	-	-	8.33	0.13	51.51	0.02	-	0.01	0.34	101.39	91.7
Fizh	F-5: UMM	CDB (<1 cm)	41.67	-	-	-	8.54	0.12	51.83	0.03	-	-	0.40	102.58	91.5
Fizh	F-5: UMM	Aureole hz	41.24	-	-	-	8.39	0.16	51.48	0.03	-	0.01	0.39	101.70	91.6
Fizh	F-5: UMM	Hz above band	41.21	0.01	-	-	8.37	0.16	50.85	0.01	0.01	-	0.38	100.99	91.5
Fizh	F-5: UMM	Ambient hz	41.46	-	-	-	8.56	0.12	51.09	0.04	-	-	0.37	101.64	91.4
Fizh	F-6: UM	CDB (5 cm)	41.28	-	-	-	8.78	0.14	50.57	0.02	0.00	0.01	0.37	101.17	91.1
Fizh	F-6: UM	Ambient hz	41.71	0.00	-	-	8.56	0.04	49.33	0.02	-	0.00	0.38	100.05	91.1

Table 2. Representative major-element compositions (in wt%) of olivine.

Abbreviations: MTZ = Moho transition zone, UMM = uppermost mantle section, UM = upper mantle section, MM = middle mantle section, LM = lower mantle section, BA = basal section, ol-gab = olivine gabbro, CDB = concordant dunite band, DB = dunite band, DDD = discordant dunite dike, Wehrlite (above) = wehrlite above the base of the layered gabbro section (outcrop F-1), Wehrlite (below) = wehrlite below the base of the layered gabbro section (outcrop F-1), Hz above band = harzburgite about 20 cm above the concordant dunite band (outcrop F-5), hz = harzburgite, and pl = plagioclase. FeO* is total iron as FeO. -: not detected.

Wadi	Outcrop	Rock type	SiO_2	TiO_2	Al_2O_3	Cr_2O_3	FeO*	MnO	MgO	CaO	Na_2O	K_2O	NiO	Total	Fo
Hilti	H-1: MM	CDB (20 cm)	40.82	-	-	0.01	8.18	0.11	50.55	0.00	0.00	-	0.37	100.04	91.7
Hilti	H-1: MM	Aureole hz	40.93	-	0.00	-	8.06	0.09	50.80	0.01	0.00	-	0.38	100.29	91.8
Hilti	H-1: MM	Ambient hz	40.94	-	-	0.01	7.70	0.10	51.10	0.01	0.01	0.00	0.40	100.26	92.2
Sarami	S-1: MTZ	Dunite	41.44	-	-	-	8.79	0.12	51.13	0.03	-	-	0.37	101.89	91.2
Sarami	S-2: UMM	CDB (5 cm)	41.73	-	-	0.00	8.39	0.08	51.07	0.15	-	-	0.36	101.79	91.6
Sarami	S-2: UMM	Aureole hz	41.39	-	-	-	8.36	0.16	51.04	0.04	-	0.01	0.37	101.36	91.6
Sarami	S-2: UMM	Ambient hz	41.42	-	-	-	8.35	0.13	51.03	0.03	-	-	0.38	101.34	91.6
Sarami	S-3: MM	CDB (4 cm)	41.40	-	-	-	8.54	0.12	50.88	0.01	-	-	0.33	101.27	91.4
Sarami	S-3: MM	Aureole hz	41.28	0.01	-	-	8.63	0.14	50.98	0.02	-	-	0.36	101.40	91.3
Sarami	S-3: MM	Ambient hz	41.02	0.01	-	-	8.28	0.14	50.91	0.01	-	0.00	0.40	100.77	91.6
Sarami	S-4: LM	CDB (2 cm)	41.48	-	-	-	8.41	0.12	51.20	0.01	0.00	0.01	0.37	101.59	91.6
Sarami	S-4: LM	Aureole hz	41.51	-	0.01	-	8.43	0.12	51.74	0.01	-	-	0.39	102.21	91.6
Sarami	S-4: LM	Ambient hz	41.44	-	-	-	8.71	0.14	50.69	0.01	-	-	0.39	101.38	91.2
Thuqbah	T-10: LM	DDD (40 cm)	41.80	-	0.00	0.01	7.87	0.13	51.60	0.03	-	-	0.39	101.82	92.1
Thuqbah	T-10: LM	Aureole hz	41.83	-	-	0.01	7.93	0.11	51.46	0.03	0.00	0.00	0.39	101.76	92.0
Thuqbah	T-10: LM	Ambient hz	41.71	-	-	-	8.36	0.15	51.54	0.01	-	-	0.36	102.12	91.7
Rayy	Ry-1: BA	CDB (40 cm)	41.39	-	-	-	8.48	0.11	50.67	0.01	-	0.01	0.42	101.09	91.4
Rayy	Ry-1: BA	CDB (150 cm)	41.66	0.00	-	-	7.73	0.10	51.96	-	-	0.00	0.44	101.90	92.3
Rayy	Ry-1: BA	Ambient hz	41.18	0.01	-	-	8.91	0.13	49.53	0.02	0.01	0.01	0.38	100.18	90.8
Umm al Hasa	U-1: BA	Aureole hz	40.73	0.02	0.02	0.07	8.41	0.16	50.72	-	0.01	0.02	0.39	100.52	91.5
Umm al Hasa	U-1: BA	Ambient hz	41.71	-	-	-	8.68	0.15	50.47	0.02	-	-	0.39	101.41	91.2
Khudayrah	K-1: BA	CDB (3 cm)	41.28	-	-	0.01	8.43	0.08	51.12	0.00	0.00	0.01	0.38	101.32	91.5
Khudayrah	K-1: BA	Aureole hz	41.66	-	-	-	8.32	0.17	51.41	0.02	-	-	0.39	101.97	91.7
Khudayrah	K-1: BA	Ambient hz	41.51	0.01	-	-	8.82	0.09	50.70	0.01	0.01	0.00	0.39	101.54	91.1

Table 2. Continued.

Wadi	Outcrop	Rock type	SiO_2	TiO_2	Al_2O_3	Cr_2O_3	Fe_2O_3	FeO	MnO	MgO	CaO	Na_2O	K_2O	NiO	Total	Mg#	Cr#
Thuqbah	T-1: MTZ	Ol-gab (Pl-rich)	0.06	0.34	22.77	40.11	5.67	20.19	0.30	9.99	0.01	0.01	-	0.10	99.55	0.469	0.542
Thuqbah	T-1: MTZ	Ol-gab (Pl-poor)	-	0.35	24.64	40.10	5.28	17.40	0.27	12.19	-	-	-	0.09	100.32	0.555	0.522
Thuqbah	T-1: MTZ	Dunite	-	0.20	25.32	43.55	2.02	13.74	0.20	14.53	-	0.02	0.01	0.10	99.69	0.653	0.536
Thuqbah	T-1: MTZ	Harzburgite	0.01	0.11	25.12	42.13	3.19	15.36	0.26	13.37	-	0.07	-	0.11	99.73	0.608	0.529
Thuqbah	T-2: UMM	CDB (20 cm)	0.18	0.06	21.05	46.18	3.24	17.80	0.27	11.45	0.03	-	-	0.04	100.30	0.534	0.595
Thuqbah	T-2: UMM	Aureole hz	0.05	0.05	26.12	43.57	2.48	14.57	0.24	14.38	0.03	-	-	0.13	101.62	0.637	0.528
Thuqbah	T-2: UMM	Ambient hz	-	0.05	27.88	42.81	1.03	14.63	0.25	14.48	0.02	0.02	-	0.09	101.26	0.638	0.507
Thuqbah	T-3: UMM	CDB (3 cm)	-	0.03	22.56	44.13	4.16	15.84	0.25	12.81	0.01	-	-	0.12	99.91	0.590	0.568
Thuqbah	T-3: UMM	Aureole hz	-	0.02	23.27	45.32	2.28	16.00	0.29	12.84	0.01	0.01	-	0.12	100.16	0.588	0.566
Thuqbah	T-3: UMM	Ambient hz	0.01	0.05	23.68	44.19	2.84	16.78	0.30	12.42	-	-	-	0.06	100.33	0.569	0.556
Thuqbah	T-4: UMM	CDB (250 cm)	-	0.06	32.60	37.48	2.19	13.02	0.19	16.13	-	0.02	-	0.14	101.83	0.688	0.435
Thuqbah	T-5: UM	CDB (25 cm)	0.01	0.07	27.77	35.32	7.28	17.96	0.30	12.15	0.07	0.03	-	0.15	101.11	0.547	0.460
Thuqbah	T-5: UM	Aureole hz	-	0.03	28.94	40.66	1.30	15.77	0.23	13.74	0.01	0.03	0.01	0.07	100.79	0.608	0.485
Thuqbah	T-5: UM	Ambient hz	-	-	24.88	43.74	2.66	16.14	0.30	13.05	-	-	-	0.07	100.84	0.590	0.541
Thuqbah	T-6: UM	CDB (6 cm)	-	0.12	21.88	45.57	2.99	16.97	0.32	12.06	0.02	0.02	-	0.06	100.01	0.559	0.583
Thuqbah	T-6: UM	Aureole hz	-	0.06	23.67	44.25	2.47	16.69	0.28	12.41	0.01	-	-	0.05	99.89	0.570	0.556
Thuqbah	T-6: UM	Ambient hz	0.01	0.05	22.14	46.62	2.58	16.16	0.27	12.74	-	0.02	-	0.10	100.69	0.584	0.586
Thuqbah	T-7: MM	CDB (80 cm)	-	0.08	19.68	50.07	1.61	15.37	0.30	12.91	0.01	-	-	0.06	100.09	0.599	0.631
Thuqbah	T-7: MM	Aureole hz	-	0.06	21.68	47.62	2.39	16.11	0.29	12.82	-	0.01	0.01	0.07	101.06	0.586	0.596
Thuqbah	T-7: MM	Ambient hz	-	0.07	28.20	41.00	2.26	13.64	0.22	14.99	-	0.03	-	0.14	100.55	0.662	0.494
Thuqbah	T-8: LM	CDB (8 cm)	-	0.07	17.86	49.72	4.17	16.47	0.31	12.11	-	0.01	-	0.07	100.79	0.567	0.651
Thuqbah	T-8: LM	Dunite lens	-	-	16.47	51.11	3.42	17.96	0.31	10.86	0.01	0.01	-	0.06	100.21	0.519	0.675
Thuqbah	T-8: LM	Aureole hz	-	0.06	17.38	52.00	1.55	17.18	0.33	11.47	-	-	-	0.03	100.00	0.543	0.667
Thuqbah	T-8: LM	Ambient hz	-	0.03	28.36	40.82	1.81	15.41	0.27	13.88	0.01	0.01	-	0.10	100.70	0.616	0.491
Thuqbah	T-9: LM	CDB (30 cm)	-	0.08	22.72	46.63	1.69	15.72	0.28	13.02	0.01	0.03	-	0.07	100.25	0.596	0.579
Thuqbah	T-9: LM	Aureole hz	-	0.05	24.47	45.48	0.99	16.53	0.32	12.76	-	-	-	0.03	100.63	0.579	0.555
Thuqbah	T-9: LM	Ambient hz	-	0.04	28.60	40.35	1.49	14.83	0.28	14.09	0.01	-	-	0.07	99.76	0.629	0.486
Rajmi	R-1: UM	CDB (25 cm)	0.07	0.18	25.41	38.15	6.49	14.03	0.27	14.04	0.05	0.03	0.02	0.15	98.89	0.641	0.502
Rajmi	R-1: UM	Aureole hz	-	0.06	29.56	39.14	2.38	14.28	0.22	14.71	-	0.03	-	0.08	100.46	0.647	0.470
Rajmi	R-1: UM	Ambient hz	-	0.05	26.27	41.22	2.84	16.07	0.27	13.06	0.01	0.02	-	0.09	99.90	0.592	0.513
Rajmi	R-2: UM	CDB (20 cm)	0.61	0.12	26.34	37.82	6.23	17.61	0.34	12.22	0.01	0.03	0.01	0.10	101.44	0.553	0.491
Rajmi	R-2: UM	Aureole hz	-	0.09	20.51	48.02	2.59	17.76	0.31	11.61	-	-	-	0.08	100.97	0.538	0.611
Rajmi	R-2: UM	CDB (<1 cm)	0.02	0.09	24.53	43.14	2.85	17.37	0.31	12.19	-	-	-	0.10	100.60	0.556	0.541
Rajmi	R-2: UM	CDB (<1 cm)	-	0.08	25.82	42.06	2.48	16.70	0.33	12.69	-	-	-	0.09	100.25	0.575	0.522
Rajmi	R-2: UM	Ambient hz	-	0.16	27.17	41.40	2.93	14.99	0.24	14.18	-	-	-	0.10	101.17	0.628	0.505
Rajmi	R-3: MM	CDB (15 cm)	-	0.14	18.23	49.39	3.32	17.04	0.32	11.70	-	0.02	-	0.08	100.24	0.550	0.645
Rajmi	R-3: MM	Aureole hz	-	0.05	27.91	40.66	2.28	15.71	0.25	13.62	-	-	-	0.10	100.58	0.607	0.494
Rajmi	R-3: MM	Ambient hz	-	0.04	29.99	38.54	2.57	14.56	0.23	14.60	0.01	0.02	-	0.09	100.65	0.641	0.463
Zabin	Z-1: MM	CDB (5 cm)	-	0.11	15.60	51.36	4.33	18.83	0.36	10.40	-	0.02	-	0.07	101.08	0.496	0.688
Zabin	Z-1: MM	Aureole hz	0.02	0.09	16.74	50.42	3.72	18.54	0.33	10.60	-	-	-	0.06	100.52	0.505	0.669
Zabib	Z-1: MM	Ambient hz	-	0.02	22.08	44.76	4.05	17.96	0.31	11.56	-	-	-	0.07	100.81	0.534	0.576
Fizh	F-1: MTZ	Wehrlite (above)	-	1.44	17.88	36.25	12.66	25.89	0.50	6.14	-	0.02	-	0.11	100.88	0.297	0.576
Fizh	F-1: MTZ	Wehrlite (below)	0.01	0.66	16.22	36.35	14.45	25.71	0.50	5.61	-	0.03	-	0.15	99.69	0.280	0.601
Fizh	F-1: MTZ	Dunite	0.01	1.00	19.36	39.46	9.86	21.48	0.41	9.13	0.01	-	-	0.14	100.86	0.431	0.578
Fizh	F-2: UMM	CDB (20 cm)	0.02	0.06	26.32	34.44	8.32	20.40	0.33	10.24	0.01	0.02	-	0.17	100.33	0.472	0.467
Fizh	F-2: UMM	Aureole hz	-	0.04	25.77	38.24	5.63	20.28	0.30	10.41	0.05	-	-	0.10	100.82	0.478	0.499
Fizh	F-2: UMM	Ambient hz	0.01	0.04	22.60	44.38	4.40	16.33	0.30	12.68	-	-	-	0.11	100.85	0.581	0.568
Fizh	F-3: UMM	CDB (8 cm)	0.02	0.07	25.32	37.42	6.98	18.45	0.28	11.39	0.02	0.02	-	0.15	100.12	0.524	0.498
Fizh	F-3: UMM	Aureole hz	-	0.04	27.44	39.75	3.83	15.38	0.24	13.76	0.01	-	-	0.07	100.52	0.614	0.493
Fizh	F-3: UMM	Ambient hz	0.04	0.04	26.24	41.60	3.43	15.61	0.26	13.54	0.02	-	-	0.12	100.90	0.607	0.515
Fizh	F-4: UMM	CDB (25 cm)	0.07	0.08	26.73	40.64	3.90	14.72	0.29	14.13	-	-	-	0.11	100.67	0.631	0.505
Fizh	F-5: UMM	CDB (<1 cm)	0.01	0.01	22.70	44.99	3.39	15.85	0.29	12.88	-	-	-	0.10	100.21	0.592	0.571
Fizh	F-5: UMM	Aureole hz	-	0.01	22.77	44.45	3.79	16.80	0.32	12.33	0.01	0.06	-	0.06	100.58	0.567	0.567
Fizh	F-5: UMM	Hz above band	-	0.13	22.28	44.91	3.42	16.26	0.31	12.56	0.02	0.02	-	0.09	100.00	0.579	0.575
Fizh	F-5: UMM	Ambient hz	0.00	-	24.92	43.01	3.16	16.73	0.27	12.67	0.00	0.02	-	0.08	100.87	0.574	0.536
Fizh	F-6: UM	CDB (5 cm)	-	0.06	16.88	48.42	5.22	19.65	0.34	9.85	0.01	-	-	0.09	100.52	0.472	0.658
Fizh	F-6: UM	Ambient hz	-	0.03	19.14	47.65	4.84	18.38	0.33	11.13	-	0.02	-	0.07	101.59	0.519	0.625

Table 3. Representative major-element compositions (in wt%) of chromian spinel. Abbreviations are the same in Table 2. -: not detected.

Wadi	Outcrop	Rock type	SiO_2	TiO_2	Al_2O_3	Cr_2O_3	Fe_2O_3	FeO	MnO	MgO	CaO	Na_2O	K_2O	NiO	Total	Mg#	Cr#
Hilti	H-1: MM	CDB (20 cm)	0.02	0.03	27.47	40.96	2.06	15.50	0.27	13.58	-	0.02	-	0.08	99.99	0.610	0.500
Hilti	H-1: MM	Aureole hz	-	0.03	26.06	43.09	2.05	15.29	0.26	13.70	-	-	-	0.09	100.57	0.615	0.526
Hilti	H-1: MM	Ambient hz	-	0.01	28.52	39.76	2.42	15.04	0.20	14.00	-	0.02	-	0.09	100.06	0.624	0.483
Sarami	S-1: MTZ	Dunite	-	0.22	19.51	46.78	4.47	17.76	0.31	11.44	0.01	0.01	-	0.10	100.61	0.535	0.617
Sarami	S-2: UMM	CDB (5 cm)	0.03	0.08	24.37	41.85	4.27	17.81	0.28	11.88	-	-	-	0.12	100.69	0.543	0.535
Sarami	S-2: UMM	Aureole hz	-	0.02	25.20	42.81	2.24	15.60	0.28	13.15	0.02	-	-	0.09	99.41	0.600	0.533
Sarami	S-2: UMM	Ambient hz	-	0.03	22.65	45.29	3.81	15.02	0.26	13.53	-	-	0.01	0.12	100.72	0.616	0.573
Sarami	S-3: MM	CDB (4 cm)	-	0.15	18.60	48.03	3.74	19.29	0.36	10.33	0.01	-	-	0.07	100.58	0.488	0.634
Sarami	S-3: MM	Aureole hz	0.01	0.10	22.55	45.76	2.88	16.94	0.26	12.35	-	0.03	-	0.06	100.94	0.565	0.576
Sarami	S-3: MM	Ambient hz	0.01	0.07	25.77	42.71	2.47	15.92	0.27	13.26	-	0.01	-	0.08	100.57	0.597	0.526
Sarami	S-4: LM	CDB (2 cm)	-	0.07	21.74	47.33	1.89	17.46	0.31	11.89	-	-	0.02	0.06	100.77	0.548	0.594
Sarami	S-4: LM	Aureole hz	-	0.08	20.72	48.35	2.14	17.05	0.31	12.06	-	-	0.01	0.03	100.75	0.558	0.610
Sarami	S-4: LM	Ambient hz	-	0.09	20.48	48.80	1.77	17.71	0.35	11.64	0.01	-	-	0.05	100.90	0.540	0.615
Thuqbah	T-10: LM	DDD (40 cm)	0.02	0.03	9.37	60.85	1.44	19.31	0.37	9.40	-	0.03	-	0.02	100.84	0.465	0.813
Thuqbah	T-10: LM	Aureole hz	-	0.04	10.72	60.27	1.25	18.41	0.38	10.24	-	-	-	0.02	101.33	0.498	0.790
Thuqbah	T-10: LM	Ambient hz	-	0.05	23.78	46.58	1.07	16.15	0.32	13.01	0.01	0.01	-	0.06	101.04	0.589	0.568
Rayy	Ry-1: BA	CDB (40 cm)	-	0.06	18.00	49.60	2.69	18.33	0.34	10.71	0.01	-	-	0.04	99.78	0.510	0.649
Rayy	Ry-1: BA	CDB (150 cm)	-	0.08	9.77	59.18	3.30	18.89	0.37	9.85	-	0.02	-	0.04	101.50	0.482	0.803
Rayy	Ry-1: BA	Ambient hz	-	0.06	17.69	49.85	2.78	18.57	0.33	10.54	-	-	0.01	0.07	99.90	0.503	0.654
Umm al Hasa	U-1: BA	Aureole hz	-	0.10	13.70	54.70	2.82	18.34	0.37	10.43	-	0.01	0.01	0.05	100.53	0.503	0.728
Umm al Hasa	U-1: BA	Ambient hz	0.01	0.04	15.20	53.09	2.99	18.89	0.33	10.28	-	-	-	0.06	100.89	0.492	0.701
Khudayrah	K-1: BA	CDB (3 cm)	-	0.06	21.44	45.39	2.93	18.36	0.32	11.01	0.01	0.01	-	0.08	99.61	0.516	0.587
Khudayrah	K-1: BA	Aureole hz	-	0.05	23.25	45.36	1.77	18.38	0.32	11.41	0.01	-	-	0.01	100.56	0.525	0.567
Khudayrah	K-1: BA	Ambient hz	-	0.04	27.35	42.09	1.52	16.51	0.28	13.13	0.01	-	-	0.06	100.99	0.586	0.508

Table 3. Continued.

Wadi	Outcrop	Rock type	SiO_2	TiO_2	Al_2O_3	Cr_2O_3	FeO*	MnO	MgO	CaO	Na_2O	K_2O	NiO	Total	Mg#
Thuqbah	T-1: MTZ	Ol-gab (Pl-rich)	51.95	0.18	3.24	1.20	2.85	0.09	16.58	23.49	0.51	0.01	0.01	100.11	0.912
Thuqbah	T-1: MTZ	Ol-gab (Pl-poor)	51.67	0.21	3.43	1.13	2.85	0.09	16.49	23.90	0.32	-	0.04	100.11	0.912
Thuqbah	T-1: MTZ	Dunite	52.78	0.14	2.99	1.22	2.27	0.07	17.77	22.31	0.47	-	0.03	100.02	0.933
Thuqbah	T-1: MTZ	Harzburgite	53.29	0.09	2.64	1.05	2.14	0.07	17.30	23.74	0.32	-	0.05	100.68	0.935
Thuqbah	T-2: UMM	Aureole hz	53.59	0.05	2.73	1.14	2.37	0.10	18.06	23.38	0.08	0.00	0.03	101.53	0.931
Thuqbah	T-2: UMM	Ambient hz	53.41	0.04	3.05	1.15	2.44	0.06	18.90	21.81	0.02	0.00	0.08	100.96	0.932
Thuqbah	T-3: UMM	Aureole hz	54.18	0.01	2.50	1.02	2.32	0.08	17.17	22.95	0.26	-	0.03	100.52	0.929
Thuqbah	T-3: UMM	Ambient hz	53.94	0.01	2.33	0.99	2.11	0.08	17.53	23.68	-	-	0.05	100.71	0.937
Thuqbah	T-4: UMM	CDB (250 cm)	52.67	0.07	3.99	1.32	3.11	0.09	19.22	20.73	0.02	-	0.06	101.27	0.917
Thuqbah	T-5: UM	Aureole hz	53.67	0.01	2.89	1.14	2.48	0.09	17.80	22.35	0.02	-	0.04	100.48	0.927
Thuqbah	T-5: UM	Ambient hz	54.00	0.02	2.38	1.00	2.09	0.08	17.00	23.95	0.08	0.00	0.06	100.66	0.936
Thuqbah	T-6: UM	CDB (6 cm)	54.37	0.02	1.53	0.63	2.18	0.06	17.90	23.70	0.17	-	0.06	100.61	0.936
Thuqbah	T-6: UM	Aureole hz	54.10	0.06	1.91	0.82	1.99	0.07	17.59	24.22	0.13	-	0.04	100.93	0.940
Thuqbah	T-6: UM	Ambient hz	54.43	0.05	2.10	0.92	2.14	0.07	18.40	23.47	0.11	-	0.05	101.74	0.939
Thuqbah	T-7: MM	CDB (80 cm)	55.50	0.02	1.41	0.59	1.83	0.07	18.45	23.71	0.16	0.00	0.05	101.81	0.947
Thuqbah	T-7: MM	Aureole hz	54.69	-	1.81	0.70	2.17	0.07	18.76	23.22	0.01	0.01	0.05	101.48	0.939
Thuqbah	T-7: MM	Ambient hz	53.72	0.03	2.38	0.95	1.78	0.05	17.61	24.12	0.12	-	0.06	100.81	0.946
Thuqbah	T-8: LM	CDB (8 cm)	55.23	-	1.44	0.85	1.54	0.01	16.94	25.22	0.19	-	0.06	101.49	0.951
Thuqbah	T-8: LM	Dunite lens	55.10	0.01	1.38	0.83	1.59	0.06	17.41	24.21	0.17	0.01	0.03	100.79	0.951
Thuqbah	T-8: LM	Aureole hz	55.54	0.01	1.20	0.67	1.61	0.05	17.77	23.81	0.18	-	0.04	100.88	0.952
Thuqbah	T-8: LM	Ambient hz	54.73	0.02	2.47	1.00	1.98	0.04	17.81	23.55	0.04	-	0.05	101.67	0.941
Thuqbah	T-9: LM	CDB (30 cm)	54.50	0.04	1.69	0.73	1.53	0.04	17.52	25.02	0.09	0.01	0.04	101.21	0.953
Thuqbah	T-9: LM	Aureole hz	53.10	0.00	1.90	0.81	2.27	0.08	19.33	22.39	0.06	-	0.06	100.00	0.938
Thuqbah	T-9: LM	Ambient hz	53.63	0.01	2.47	0.98	1.92	0.08	17.33	24.29	0.02	-	0.05	100.77	0.941
Rajmi	R-1: UM	Aureole hz	53.74	0.07	2.61	0.85	2.07	0.06	17.27	23.59	0.05	-	0.04	100.34	0.937
Rajmi	R-1: UM	Ambient hz	53.73	0.05	2.37	0.99	1.84	0.07	16.97	24.23	0.13	0.01	0.04	100.40	0.943
Rajmi	R-2: UM	CDB (20 cm)	54.10	0.04	2.02	0.91	1.72	0.07	17.51	23.87	0.10	-	0.04	100.37	0.948
Rajmi	R-2: UM	Aureole hz	54.88	0.06	1.54	0.80	1.90	0.07	17.64	23.96	0.17	0.00	0.05	101.07	0.943
Rajmi	R-2: UM	CDB (<1 cm)	54.39	0.04	2.11	0.88	1.92	0.08	17.37	23.98	0.13	-	0.03	100.93	0.942
Rajmi	R-2: UM	CDB (<1 cm)	54.19	0.06	1.73	0.71	1.86	0.09	17.80	24.42	0.09	-	0.05	101.00	0.945
Rajmi	R-2: UM	Ambient hz	53.07	0.12	2.14	0.80	1.82	0.08	17.78	24.13	0.07	0.01	0.05	100.07	0.946
Rajmi	R-3: MM	CDB (15 cm)	54.15	0.05	1.18	0.53	1.77	0.04	17.53	24.34	0.09	0.01	0.04	99.72	0.946
Rajmi	R-3: MM	Aureole hz	53.42	0.05	2.00	0.83	1.94	0.08	17.66	24.04	0.12	-	0.04	100.18	0.942
Rajmi	R-3: MM	Ambient hz	53.77	0.03	2.63	0.84	2.17	0.04	17.96	23.53	-	0.00	0.04	101.03	0.936
Zabin	Z-1: MM	Aureole hz	54.49	0.01	1.49	0.77	2.03	0.08	17.50	24.21	0.20	0.01	0.03	100.81	0.939
Zabib	Z-1: MM	Ambient hz	54.25	-	1.97	0.88	2.16	0.08	17.43	24.04	0.12	-	0.03	100.96	0.935
Fizh	F-1: MTZ	Wehrlite (above)	53.79	0.58	2.56	0.49	5.35	0.13	20.15	18.13	0.26	0.00	0.02	101.45	0.870
Fizh	F-1: MTZ	Wehrlite (below)	53.88	0.33	1.83	0.46	3.26	0.10	17.32	23.14	0.22	-	0.06	100.60	0.904
Fizh	F-1: MTZ	Dunite	51.42	0.46	2.87	1.03	3.80	0.11	17.21	22.65	0.27	-	0.03	99.85	0.890
Fizh	F-2: UMM	Aureole hz	54.28	-	2.53	1.00	2.52	0.07	17.52	22.78	0.23	0.01	0.04	100.97	0.925
Fizh	F-2: UMM	Ambient hz	54.49	0.01	2.12	0.78	2.50	0.10	18.43	22.83	-	-	0.04	101.30	0.929
Fizh	F-3: UMM	Aureole hz	52.86	0.04	2.70	0.96	2.39	0.09	18.80	22.18	0.19	-	0.06	100.27	0.933
Fizh	F-3: UMM	Ambient hz	52.92	0.04	2.83	1.07	2.17	0.10	18.24	23.40	0.00	-	0.06	100.82	0.937
Fizh	F-4: UMM	CDB (25 cm)	53.14	0.07	2.86	1.09	2.30	0.10	17.78	24.06	0.14	0.01	0.05	101.59	0.932
Fizh	F-5: UMM	Aureole hz	53.82	0.02	2.11	0.88	2.49	0.09	18.65	22.95	0.08	0.00	0.05	101.14	0.930
Fizh	F-5: UMM	Hz above band	54.14	0.19	2.44	1.04	2.51	0.10	18.97	22.20	0.11	0.01	0.06	101.77	0.931
Fizh	F-5: UMM	Ambient hz	54.18	0.03	2.23	0.77	2.52	0.06	18.44	23.10	0.01	0.00	0.06	101.39	0.929
Fizh	F-6: UM	CDB (5 cm)	54.92	0.05	1.60	0.90	2.00	0.06	17.82	24.07	0.25	-	0.03	101.67	0.941
Fizh	F-6: UM	Ambient hz	54.44	0.02	1.89	0.92	1.99	0.03	17.38	24.19	0.15	0.00	0.03	101.05	0.939

Table 4. Representative major-element compositions (in wt%) of clinopyroxene. Abbreviations are the same in Table 2. FeO* is total iron as FeO. -: not detected.

Wadi	Outcrop	Rock type	SiO_2	TiO_2	Al_2O_3	Cr_2O_3	FeO*	MnO	MgO	CaO	Na_2O	K_2O	NiO	Total	Mg#
Hilti	H-1: MM	CDB (20 cm)	53.34	0.01	2.40	0.91	1.93	0.06	17.40	24.63	0.04	0.01	0.06	100.79	0.941
Hilti	H-1: MM	Aureole hz	53.17	0.01	2.42	0.90	2.01	0.06	17.44	24.61	0.01	-	0.06	100.68	0.939
Hilti	H-1: MM	Ambient hz	53.50	-	2.51	0.97	1.84	0.08	17.42	24.76	0.11	-	0.04	101.21	0.944
Sarami	S-1: MTZ	Dunite	54.39	0.12	2.35	1.10	2.57	0.09	17.73	22.36	0.37	0.01	0.05	101.13	0.925
Sarami	S-2: UMM	CDB (5 cm)	53.47	0.07	3.05	1.19	2.53	0.05	17.99	22.49	0.04	0.00	0.03	100.92	0.927
Sarami	S-2: UMM	Aureole hz	53.67	-	2.61	1.07	2.85	0.10	20.38	19.31	0.01	-	0.05	100.04	0.927
Sarami	S-2: UMM	Ambient hz	54.10	0.02	2.46	0.98	2.56	0.11	18.87	22.26	-	-	0.06	101.41	0.929
Sarami	S-3: MM	Aureole hz	53.83	0.07	1.88	0.88	1.88	0.06	17.61	24.41	0.13	-	0.04	100.77	0.944
Sarami	S-3: MM	Ambient hz	53.40	0.03	2.28	0.91	1.79	0.10	17.42	24.85	0.08	-	0.07	100.92	0.945
Sarami	S-4: LM	CDB (2 cm)	54.85	0.03	1.73	0.76	1.98	0.07	18.32	24.08	0.03	0.01	0.03	101.89	0.943
Sarami	S-4: LM	Aureole hz	54.67	0.04	1.67	0.71	1.88	0.06	18.14	24.15	0.04	0.00	0.02	101.37	0.945
Sarami	S-4: LM	Ambient hz	54.78	0.01	1.66	0.74	1.96	0.07	18.30	24.01	0.05	0.00	0.03	101.61	0.943
Thuqbah	T-10: LM	Aureole hz	55.72	0.00	0.59	0.57	1.51	0.01	18.24	24.31	0.28	-	0.03	101.25	0.956
Thuqbah	T-10: LM	Ambient hz	54.98	0.02	1.57	0.79	1.65	0.04	17.89	23.60	0.06	0.00	0.03	100.63	0.951
Rayy	Ry-1: BA	CDB (40 cm)	55.21	-	1.16	0.46	2.06	0.08	18.18	23.71	0.02	0.01	0.05	100.93	0.940
Rayy	Ry-1: BA	Ambient hz	54.74	0.02	1.27	0.59	1.70	0.06	17.41	24.19	-	0.01	0.03	100.01	0.948
Umm al Hasa	U-1: BA	Aureole hz	54.93	0.03	0.84	0.49	1.62	0.07	18.02	24.49	0.15	0.01	0.00	100.64	0.952
Umm al Hasa	U-1: BA	Ambient hz	55.14	0.02	1.06	0.67	1.86	0.08	17.77	24.11	0.13	-	0.04	100.87	0.945
Khudayrah	K-1: BA	Aureole hz	54.28	-	1.54	0.70	1.81	0.08	17.43	24.11	0.05	-	0.03	100.04	0.945
Khudayrah	K-1: BA	Ambient hz	53.98	0.03	2.33	0.93	2.03	0.09	17.79	24.38	0.03	0.00	0.05	101.62	0.940

Table 4. Continued.

Wadi	Outcrop	Rock type	SiO_2	TiO_2	Al_2O_3	Cr_2O_3	FeO*	MnO	MgO	CaO	Na_2O	K_2O	NiO	Total	Mg#
Thuqbah	T-1: MTZ	Harzburgite	56.44	0.00	2.12	0.60	5.56	0.12	33.60	1.67	0.03	-	0.10	100.26	0.915
Thuqbah	T-2: UMM	Ambient hz	56.80	0.04	2.22	0.77	5.56	0.14	33.44	1.98	0.01	-	0.08	101.03	0.915
Thuqbah	T-3: UMM	Ambient hz	57.49	0.02	1.76	0.63	5.57	0.13	34.18	0.95	0.01	0.01	0.10	100.84	0.916
Thuqbah	T-4: UMM	CDB (250 cm)	55.71	0.03	3.57	0.85	6.50	0.12	33.55	0.88	-	0.00	0.07	101.28	0.902
Thuqbah	T-5: UM	Ambient hz	56.84	0.01	2.05	0.69	5.73	0.14	35.03	0.53	-	-	0.07	101.08	0.916
Thuqbah	T-6: UM	Ambient hz	57.44	-	1.66	0.51	5.36	0.11	35.07	0.98	0.02	-	0.07	101.22	0.921
Thuqbah	T-7: MM	CDB (80 cm)	57.88	0.01	1.28	0.46	5.08	0.14	35.41	0.82	0.00	-	0.08	101.17	0.925
Thuqbah	T-7: MM	Ambient hz	56.74	0.02	2.48	0.76	5.29	0.13	34.49	0.94	0.00	-	0.11	100.96	0.921
Thuqbah	T-8: LM	Ambient hz	57.04	0.00	1.96	0.62	5.60	0.16	33.41	1.64	0.01	-	0.06	100.49	0.914
Thuqbah	T-9: LM	Ambient hz	56.54	-	2.42	0.80	5.28	0.11	33.42	2.23	0.01	0.00	0.07	100.88	0.919
Rajmi	R-1: UM	Ambient hz	57.33	0.03	2.06	0.62	5.49	0.14	34.04	0.96	-	-	0.08	100.74	0.917
Rajmi	R-2: UM	CDB (20 cm)	57.25	0.03	1.85	0.65	5.86	0.12	34.15	1.13	-	-	0.09	101.13	0.912
Rajmi	R-2: UM	Ambient hz	55.44	0.05	2.04	0.45	5.53	0.11	34.85	0.46	-	0.00	0.06	99.01	0.918
Rajmi	R-3: MM	Ambient hz	57.11	0.03	2.27	0.43	5.70	0.14	35.09	0.61	-	-	0.06	101.45	0.916
Zabin	Z-1: MM	Ambient hz	57.22	-	1.56	0.45	5.86	0.15	34.26	0.99	-	-	0.07	100.56	0.912
Fizh	F-2: UMM	Ambient hz	57.93	0.00	1.58	0.48	5.82	0.13	35.62	0.95	0.00	-	0.09	102.61	0.916
Fizh	F-3: UMM	Ambient hz	56.36	-	2.22	0.62	5.71	0.11	34.05	1.33	0.01	-	0.08	100.47	0.914
Fizh	F-4: UMM	CDB (25 cm)	56.48	0.01	2.25	0.68	5.44	0.16	34.13	1.88	0.00	-	0.09	101.13	0.918
Fizh	F-5: UMM	Hz above band	57.29	0.02	1.76	0.60	5.44	0.13	34.02	1.65	0.02	-	0.10	101.01	0.918
Fizh	F-5: UMM	Aureole hz	56.92	0.02	1.97	0.75	5.52	0.13	34.33	1.84	0.01	-	0.10	101.57	0.917
Fizh	F-5: UMM	Ambient hz	57.34	-	1.99	0.63	5.41	0.14	34.39	1.15	-	-	0.10	101.15	0.919
Fizh	F-6: UM	CDB (5 cm)	57.13	0.01	1.35	0.54	5.97	0.16	34.22	1.04	0.00	-	0.10	100.51	0.911
Fizh	F-6: UM	Ambient hz	57.81	-	1.44	0.44	5.53	0.10	34.50	1.32	0.01	0.01	0.09	101.25	0.917
Hilti	H-1: MM	Ambient hz	56.67	-	2.07	0.54	5.50	0.12	34.48	0.96	-	-	0.08	100.42	0.918
Sarami	S-2 UMM	Ambient hz	57.43	0.01	1.82	0.64	5.39	0.12	34.77	1.64	-	0.00	0.12	101.93	0.920
Sarami	S-3: MM	Ambient hz	56.96	0.01	1.98	0.60	5.32	0.15	34.39	1.39	-	0.01	0.11	100.92	0.920
Sarami	S-4: LM	Ambient hz	57.72	0.02	1.41	0.42	5.99	0.13	34.94	0.79	-	0.01	0.03	101.48	0.912
Thuqbah	T-10: LM	Ambient hz	57.92	-	1.64	0.54	5.47	0.13	34.84	1.28	0.01	0.00	0.07	101.89	0.919
Rayy	Ry-1: BA	CDB (40 cm)	57.61	0.04	1.15	0.43	5.35	0.14	34.73	0.79	0.01	-	0.08	100.32	0.920
Rayy	Ry-1: BA	Ambient hz	57.78	0.01	1.19	0.44	5.89	0.16	34.44	0.58	-	0.01	0.08	100.58	0.912
Umm al Hasa	U-1: BA	Ambient hz	57.96	0.00	0.95	0.42	5.60	0.16	34.51	1.13	-	0.01	0.08	100.81	0.917
Khudayrah	K-1: BA	Ambient hz	56.80	0.01	1.99	0.54	5.53	0.12	33.84	1.61	0.00	-	0.08	100.52	0.916

Table 5. Representative major-element compositions (in wt%) of orthopyroxene. Abbreviations are the same in Table 2. FeO* is total iron as FeO. -: not detected.

Wadi	Outcrop	Rock type	SiO_2	TiO_2	Al_2O_3	Cr_2O_3	FeO*	MnO	MgO	CaO	Na_2O	K_2O	NiO	Total	An
Thuqbah	T-1: MTZ	Ol-gab (Pl-poor)	45.65	-	34.87	-	0.13	-	0.01	18.55	1.21	-	-	100.42	0.894

Table 6. Representative major-element compositions (in wt%) of plagioclase. Abbreviations are the same in Table 2. FeO* is total iron as FeO. -: not detected.

Wadi	Outcrop	Rock type	La	Ce	Sr	Pr	Nd	Zr	Sm	Eu	Gd	Ti	Tb	Dy	Y	Ho	Er	Tm	Yb	Lu
Thuqbah	T-1: MTZ	Ol-gab (Pl-rich)	0.032	0.220	6.595	0.052	0.444	1.105	0.301	0.224	0.532	1378.16	0.105	0.832	4.637	0.191	0.554	0.083	0.641	0.088
Thuqbah	T-1: MTZ	Ol-gab (Pl-poor)	0.033	0.256	3.388	0.071	0.584	2.395	0.368	0.162	0.660	1272.87	0.138	1.069	6.366	0.241	0.752	0.110	0.750	0.102
Thuqbah	T-1: MTZ	Dunite	0.066	0.419	6.569	0.099	0.793	2.377	0.454	0.236	0.798	976.97	0.175	1.469	9.009	0.345	1.042	0.156	1.026	0.132
Thuqbah	T-1: MTZ	Harzburgite	0.033	0.210	4.051	0.055	0.423	1.612	0.232	0.113	0.475	445.63	0.099	0.772	4.001	0.162	0.430	0.058	0.384	0.054
Thuqbah	T-2: UMM	Aureole hz	-	-	0.378	-	-	0.126	-	0.007	0.041	214.75	0.018	0.164	1.268	0.051	0.164	0.040	0.267	0.032
Thuqbah	T-2: UMM	Ambient hz	-	-	0.503	-	-	0.108	-	-	-	236.51	0.008	0.121	1.156	0.039	0.184	0.031	0.268	0.039
Thuqbah	T-3: UMM	DB (3 cm)	0.013	0.021	0.712	-	-	0.049	-	-	-	161.37	0.007	0.095	0.878	0.032	0.139	0.026	0.217	0.035
Thuqbah	T-3: UMM	Ambient hz	-	-	0.075	-	-	0.036	-	-	-	142.92	0.006	0.082	0.784	0.029	0.120	0.024	0.210	0.029
Thuqbah	T-4: UMM	CDB (250 cm)	0.022	0.086	2.122	0.020	0.123	0.814	0.064	0.029	0.126	419.11	0.032	0.321	2.240	0.093	0.310	0.045	0.410	0.061
Thuqbah	T-5: UM	Aureole hz	-	-	0.136	-	-	0.069	-	-	0.029	294.10	0.012	0.182	1.621	0.067	0.270	0.049	0.368	0.054
Thuqbah	T-5: UM	Ambient hz	0.020	0.019	0.569	-	-	0.047	-	-	-	256.84	0.009	0.139	1.242	0.048	0.198	0.038	0.317	0.046
Thuqbah	T-6: UM	CDB (6 cm)	-	0.020	0.981	-	0.026	0.144	-	-	0.046	310.17	0.012	0.149	1.091	0.043	0.165	0.032	0.214	0.035
Thuqbah	T-6: UM	Ambient hz	-	0.003	0.346	-	-	0.034	-	-	-	163.88	-	0.075	0.777	0.029	0.141	0.029	0.220	0.037
Thuqbah	T-7: MM	CDB (80 cm)	0.117	0.303	1.974	0.034	0.116	0.775	-	0.012	0.079	248.92	0.021	0.237	2.016	0.083	0.300	0.045	0.376	0.053
Thuqbah	T-7: MM	Aureole hz	-	-	0.014	-	-	0.019	-	-	-	183.54	-	0.031	0.452	0.021	0.088	0.017	0.137	0.028
Thuqbah	T-7: MM	Ambient hz	-	-	0.021	-	-	0.056	0.014	0.011	0.089	429.81	0.033	0.374	2.652	0.095	0.375	0.056	0.432	0.061
Thuqbah	T-8: LM	CDB (8 cm)	0.160	0.356	5.245	0.044	0.154	0.887	0.035	0.019	0.091	147.07	0.021	0.222	1.506	0.056	0.194	0.029	0.216	0.037
Thuqbah	T-8: LM	Dunite lens	0.273	0.578	11.834	0.060	0.218	1.290	0.051	0.019	0.094	121.86	0.020	0.209	1.420	0.055	0.171	0.030	0.195	0.030
Thuqbah	T-8: LM	Ambient hz	0.009	0.011	0.163	-	-	0.055	-	-	0.035	221.52	0.013	0.188	1.456	0.061	0.221	0.039	0.304	0.043
Thuqbah	T-9: LM	CDB (30 cm)	0.011	0.032	0.822	-	-	0.226	-	0.007	0.071	309.16	0.032	0.373	2.823	0.114	0.392	0.066	0.435	0.067
Thuqbah	T-9: LM	Aureole hz	-	0.022	0.779	-	-	0.113	-	0.005	0.063	196.37	0.025	0.303	2.004	0.077	0.257	0.037	0.283	0.041
Thuqbah	T-9: LM	Ambient hz	-	-	0.026	-	-	0.031	-	-	0.017	200.75	0.011	0.142	1.265	0.046	0.204	0.040	0.296	0.047
Rajmi	R-1: UM	Aureole hz	-	0.008	0.421	-	-	0.031	-	-	0.030	361.60	0.016	0.214	1.917	0.070	0.285	0.053	0.401	0.065
Rajmi	R-1: UM	Ambient hz	0.015	0.073	2.913	0.015	0.109	0.448	0.048	0.030	0.105	362.17	0.030	0.290	2.103	0.074	0.306	0.051	0.387	0.060
Rajmi	R-2: UM	CDB (20 cm)	0.035	0.155	2.188	0.032	0.212	1.225	0.105	0.046	0.207	472.13	0.049	0.419	2.995	0.112	0.417	0.067	0.506	0.070
Rajmi	R-2: UM	Aureole hz	0.017	0.065	1.293	0.012	0.075	0.479	0.035	0.016	0.079	325.84	0.024	0.220	1.489	0.060	0.206	0.041	0.272	0.038
Rajmi	R-2: UM	CDB (<1 cm)	-	0.017	0.490	-	0.026	0.205	-	0.011	0.070	349.11	0.019	0.253	1.924	0.072	0.257	0.047	0.343	0.059
Rajmi	R-2: UM	CDB (<1 cm)	-	0.004	0.374	-	-	0.156	-	0.005	0.051	302.10	0.018	0.221	1.742	0.070	0.239	0.041	0.306	0.041
Rajmi	R-2: UM	Ambient hz	-	-	0.047	-	-	1.614	-	0.004	0.045	708.70	0.016	0.215	0.069	0.062	0.216	0.040	0.278	0.038
Rajmi	R-3: MM	CDB (15 cm)	0.011	0.041	1.072	0.009	0.075	0.812	0.036	0.022	0.130	352.38	0.039	0.359	2.382	0.092	0.311	0.046	0.344	0.047
Rajmi	R-3: MM	Ambient hz	-	-	0.099	-	-	0.040	-	0.007	0.061	299.40	0.022	0.264	1.897	0.073	0.269	0.045	0.362	0.054

Table 7. Representative trace-element compositions (in ppm) of clinopyroxene. Abbreviations are the same in Table 2. -: below detection limits. -: not detected.

Wadi	Outcrop	Rock type	La	Ce	Sr	Pr	Nd	Zr	Sm	Eu	Gd	Ti	Tb	Dy	Y	Ho	Er	Tm	Yb	Lu
Zabin	Z-1: MM	Aureole hz	0.039	0.155	6.676	0.029	0.174	0.876	0.073	0.031	0.139	203.13	0.029	0.204	1.275	0.050	0.163	0.028	0.194	0.034
Zabin	Z-1: MM	Ambient hz	0.010	0.029	1.562	0.006	0.042	0.103	0.018	0.010	0.032	109.28	0.006	0.082	0.654	0.022	0.105	0.020	0.183	0.030
Fizh	F-1: MTZ	Wehrlite (above)	0.213	1.560	8.276	0.379	2.687	9.729	1.397	0.479	2.211	3610.76	0.408	2.998	15.705	0.632	1.797	0.250	1.742	0.252
Fizh	F-1: MTZ	Wehrlite (below)	0.110	0.832	8.481	0.221	1.750	6.179	0.990	0.390	1.650	2917.20	0.325	2.306	11.961	0.481	1.363	0.185	1.245	0.172
Fizh	F-1: MTZ	Dunite	0.237	1.328	8.029	0.299	1.998	7.720	0.997	0.370	1.629	2620.47	0.313	2.247	11.898	0.483	1.318	0.195	1.207	0.180
Fizh	F-2: UMM	CDB (20 cm)	0.044	0.151	4.383	0.026	0.132	0.426	0.047	0.033	0.074	158.43	0.017	0.166	1.193	0.040	0.176	0.032	0.246	0.043
Fizh	F-2: UMM	Ambient hz	-	-	0.114	-	-	0.048	-	-	-	135.86	0.005	0.077	0.706	0.027	0.118	0.024	0.170	0.026
Fizh	F-3: UMM	Aureole hz	0.044	0.132	2.081	0.015	0.055	0.195	0.018	0.010	0.043	235.04	0.012	0.169	1.328	0.053	0.204	0.036	0.271	0.045
Fizh	F-3: UMM	Ambient hz	-	-	0.123	-	-	0.059	-	-	-	186.56	0.007	0.107	0.926	0.034	0.138	0.028	0.206	0.034
Fizh	F-4: UMM	CDB (25 cm)	0.068	0.241	5.595	0.041	0.217	1.626	0.091	0.035	0.143	457.39	0.035	0.312	2.220	0.085	0.308	0.057	0.450	0.062
Fizh	F-5: UMM	Aureole hz	0.090	0.251	0.727	0.021	0.058	0.124	0.010	0.003	0.017	124.60	0.006	0.078	0.702	0.031	0.103	0.022	0.163	0.025
Fizh	F-5: UMM	Hz above band	0.111	0.463	7.689	0.085	0.523	3.614	0.236	0.093	0.366	680.32	0.062	0.471	2.596	0.103	0.288	0.046	0.305	0.047
Fizh	F-5: UMM	Ambient hz	-	-	0.090	-	-	0.080	-	-	0.017	141.99	0.007	0.093	0.832	0.032	0.130	0.022	0.216	0.033
Fizh	F-6: UM	CDB (5 cm)	0.027	0.130	6.037	0.027	0.157	1.369	0.103	0.048	0.202	393.36	0.043	0.360	2.146	0.095	0.287	0.047	0.326	0.039
Fizh	F-6: UM	Ambient hz	0.007	0.027	1.004	0.005	0.039	0.148	0.017	0.010	0.033	148.81	0.007	0.091	0.778	0.032	0.127	0.027	0.213	0.034
Hilti	H-1: MM	CDB (20 cm)	-	-	0.119	-	-	0.053	-	-	0.027	254.83	0.010	0.175	1.653	0.062	0.293	0.053	0.447	0.066
Hilti	H-1: MM	Ambient hz	-	0.020	0.451	0.005	-	0.203	-	0.012	0.066	96.77	0.016	0.161	1.068	0.042	0.134	0.022	0.185	0.033
Sarami	S-1: MTZ	Dunite	0.107	0.545	9.889	0.129	0.917	2.482	0.443	0.179	0.679	859.93	0.118	0.880	4.503	0.177	0.516	0.070	0.467	0.065
Sarami	S-2: UMM	CDB (5 cm)	-	-	0.093	-	-	0.049	-	0.005	0.042	312.86	0.014	0.193	1.354	0.054	0.197	0.033	0.256	0.040
Sarami	S-2: UMM	Ambient hz	-	-	0.043	-	-	0.031	-	-	-	123.82	0.005	0.086	0.735	0.032	0.113	0.025	0.174	0.033
Sarami	S-3: MM	Aureole hz	0.018	0.064	1.937	0.011	0.083	0.646	0.052	0.026	0.126	341.03	0.033	0.315	1.930	0.080	0.256	0.046	0.306	0.046
Sarami	S-3: MM	Ambient hz	0.005	0.012	0.522	0.002	-	0.112	-	-	0.055	296.76	0.019	0.202	1.597	0.067	0.242	0.039	0.311	0.051
Sarami	S-4: LM	Aureole hz	0.008	0.016	0.174	0.003	0.029	0.090	0.031	0.021	0.138	264.00	0.037	0.352	2.320	0.094	0.297	0.046	0.325	0.046
Sarami	S-4: LM	Ambient hz	0.006	0.016	0.138	0.002	0.014	0.072	0.033	0.013	0.113	197.85	0.029	0.259	1.734	0.074	0.202	0.033	0.202	0.028
Thuqbah	T-10: LM	Aureole hz	0.053	0.244	5.923	0.044	0.189	0.941	0.055	0.026	0.111	85.25	0.021	0.207	1.295	0.050	0.165	0.022	0.164	0.027
Thuqbah	T-10: LM	Ambient hz	-	-	0.113	-	-	0.043	-	-	0.038	164.41	0.017	0.173	1.210	0.050	0.167	0.026	0.207	0.027
Rayy	Ry-1: BA	CDB (40 cm)	-	0.006	0.125	-	-	0.028	-	-	-	144.63	0.005	0.070	0.602	0.024	0.102	0.018	0.172	0.030
Rayy	Ry-1: BA	Ambient hz	0.007	0.012	0.159	-	-	0.047	-	-	0.028	155.64	0.009	0.086	0.653	0.025	0.098	0.018	0.128	0.020
Umm al Hasa	U-1: BA	Aureole hz	0.005	0.020	0.689	0.003	0.018	0.093	0.010	0.006	0.032	186.41	0.012	0.139	1.083	0.044	0.156	0.028	0.230	0.036
Umm al Hasa	U-1: BA	Ambient hz	0.005	0.017	0.663	0.003	0.029	0.265	0.020	0.010	0.048	112.05	0.011	0.101	0.700	0.031	0.111	0.021	0.187	0.029
Khudayrah	K-1: BA	Aureole hz	-	0.007	2.335	-	-	0.069	-	0.004	0.031	127.56	0.009	0.114	0.766	0.032	0.116	0.020	0.158	0.022
Khudayrah	K-1: BA	Ambient hz	-	-	1.731	-	-	0.035	-	-	0.020	200.62	0.005	0.102	0.920	0.037	0.134	0.028	0.207	0.034

Table 7. Continued.

Wadi	Outcrop	Rock type	La	Ce	Sr	Pr	Nd	Zr	Sm	Eu	Gd	Ti	Tb	Dy	Y	Ho	Er	Tm	Yb	Lu
Thuqbah	T-1: MTZ	Ol-gab (Pl-poor)	0.021	0.070	432.73	0.011	0.059	-	-	0.086	-	56.85	-	-	0.049	-	-	-	-	-

Table 8. Representative trace-element compositions (in ppm) of plagioclase. Abbreviations are the same in Table 2. -: below detection limits. -: not detected.

	Partition coefficient					Initial bulk composition	Chondrite composition
	ol/melt	opx/melt	cpx/melt	grt/melt	spl/melt		
La*	0.000007	0.0025	0.06	0.0035	0.0006	0.192	0.237
Ce*	0.00001	0.005	0.1	0.008	0.0006	0.55	0.612
Sr**	0.00001	0.003	0.1283	0.007	0	7.664	7.26
Pr**	0.00004	0.006	0.13	0.033	0.0006	0.107	0.095
Nd*	0.00007	0.01	0.2	0.05	0.0006	0.581	0.467
Zr*	0.004	0.024	0.12	0.4	0.07	5.082	3.87
Sm*	0.001	0.02	0.3	0.22	0.001	0.239	0.153
Eu*	0.001	0.03	0.37	0.45	0.001	0.096	0.058
Gd**	0.0012	0.04	0.37	0.9	0.0006	0.358	0.2055
Ti*	0.015	0.1	0.35	0.16	0.15	716.3	445
Tb**	0.0026	0.05	0.41	1.5	0.006	0.07	0.0374
Dy*	0.004	0.05	0.44	2	0.002	0.505	0.254
Y	-	-	-	-	-	-	1.57
Ho**	0.007	0.065	0.43	2.8	0.0023	0.115	0.0566
Er*	0.009	0.07	0.43	3.5	0.003	0.348	0.1655
Tm	-	-	-	-	-	-	0.0255
Yb*	0.014	0.09	0.41	5	0.005	0.365	0.17
Lu	-	-	-	-	-	-	0.0254

	Initial mode grt-peri	Conversion mode	Melting mode (fractional melting)			Melting mode (influx melting)	
			Grt-peri	Spl-peri (H)	Spl-peri (L)	Spl-peri (H)	Spl-peri (L)
Ol	0.55	207	0.08	-0.22	0.98	-2.19	-0.45
Opx	0.2	-607	-0.19	0.37	0	2.2	1
Cpx	0.15	-184	0.81	0.8	0	0.89	0.4
Grt	0.1	794	0.3	0	0	0	0
Spl	0	-209	0	0.05	0.02	0.1	0.05

	Compositions of influx (ppm)		
	Influx A	Influx B	Influx C
La	12.42	6.11	1.23
Ce	25.12	12.89	3.43
Sr	301.30	158.02	47.34
Pr	3.71	1.99	0.66
Nd	14.04	8.08	3.51
Zr	73.58	48.81	30.27
Sm	3.18	2.17	1.42
Eu	0.87	0.69	0.56
Gd	2.29	2.14	2.08
Ti	7144.16	5225.11	4011.38
Tb	0.31	0.36	0.40
Dy	1.81	2.37	2.84
Ho	0.32	0.50	0.63
Er	0.81	1.42	1.89
Yb	0.63	1.38	1.92

Table 9. Parameters for the modeling (1-D steady state modeling). Partition coefficients between minerals and melt are quoted from *Suhr et al. (1998) and from **Kelemen et al. (2003). See the text for further details on these parameters. Abbreviations: ol = olivine, opx = orthopyroxene, cpx = clinopyroxene, grt = garnet, spl = spinel, grt-peri = garnet peridotite, spl-peri (H) = spinel peridotite at higher pressures, and spl-peri (L) = spinel peridotite at lower pressures.

	Melt	Cpx	Convex cpx	Opx 1	Opx 2	Ol	New melt
La	2.493	-	0.149	-	0.001	-	2.474
Ce	8.500	0.001	0.804	-	0.003	-	8.420
Sr	54.281	0.101	7.166	0.093	0.072	-	55.220
Pr	1.460	0.000	0.184	-	0.001	-	1.438
Nd	7.350	0.004	1.519	-	0.006	-	7.152
Zr	48.939	0.044	5.366	0.043	0.424	0.012	36.870
Sm	2.624	0.004	0.793	-	0.004	-	2.486
Eu	0.682	0.004	0.299	0.000	0.003	-	0.591
Gd	3.739	0.010	1.309	0.001	0.015	-	3.297
Ti	6978.060	134.105	1346.754	73.800	253.221	21.742	1414.518
Tb	0.620	0.005	0.248	0.000	0.004	-	0.509
Dy	4.355	0.078	1.661	0.009	0.047	-	3.178
Y	23.857	0.698	8.304	0.106	0.357	0.006	-
Ho	0.929	0.024	0.346	0.003	0.014	0.000	0.609
Er	2.763	0.110	0.917	0.021	0.053	0.001	1.774
Tm	0.441	0.023	0.126	0.006	0.012	0.001	-
Yb	2.685	0.194	0.751	0.064	0.102	0.009	1.649
Lu	0.349	0.032	0.094	0.013	0.017	0.003	-

Table 10. Trace-element compositions (in ppm) for the modeling (plate model) and the mass balance calculation. Abbreviations: Melt = the melt in equilibrium with the clinopyroxene in the MTZ dunite of Wadi Fizh, Cpx = the clinopyroxene in the most depleted wall harzburgite, Convex cpx and Opx 2 = the clinopyroxene and the orthopyroxene of the composite grain (Fig. 4c) in the harzburgite about 20 cm above the concordant dunite band at outcrop F-5, Opx 1 and Ol = the orthopyroxene and the olivine in the ambient harzburgite at outcrop F-5, and New melt = a melt generated by the mass balance calculation. Trace-element compositions of 'Melt' and 'Cpx' are from Akizawa et al. (2012). -: below detection limit. See the text for details on the mass balance calculation.